SPHERICAL NANOINDENTATION PROTOCOLS FOR EXTRACTING MICROSCALE MECHANICAL PROPERTIES IN VISCOELASTIC MATERIALS

A Dissertation
Presented to
The Academic Faculty

By

Mohammed T. Abba

In Partial Fulfillment
Of the Requirements for the Degree
Doctor of Philosophy in Mechanical Engineering

Georgia Institute of Technology

December 2015

SPHERICAL NANOINDENTATION PROTOCOLS FOR EXTRACTING MICROSCALE MECHANICAL PROPERTIES IN VISCOELASTIC MATERIALS

Approved by:

Dr. Surya R. Kalidindi, Advisor
School of Mechanical Engineering
Georgia Institute of Technology

Dr. Ulrike G.K. Wegst
Thayer School of Engineering
Dartmouth College

Dr. Min Zhou
School of Mechanical Engineering
Georgia Institute of Technology

Dr. Karl I. Jacob
School of Materials Science and Engineering
Georgia Institute of Technology

Dr. Kenneth Gall
School of Materials Science and Engineering
Georgia Institute of Technology

Date Approved: 08/21/2015

ACKNOWLEDGEMENTS

TABLE OF CONTENTS

LIST OF TABLES

LIST OF FIGURES

SUMMARY

Nanoindentation has a high load resolution, depth sensing capabilities, and can be used to characterize the local mechanical behavior in material systems with heterogeneous microstructures. Recently nanoindentation has been used to extract useful stress-strain curves, primarily in hard materials such as metals and ceramics. To apply these indentation stress-strain methods to polymer composites, we have to first develop analysis techniques for materials that exhibit viscoelasticity. In a lot of current research the viscoelastic material properties are extracted after the material has been deformed enough to initiate plasticity and in some cases the time dependence of the deformation is ignored. This doesn't give an accurate representation of the material properties of the undeformed sample or the local deformation behavior of the material. This dissertation develops analysis protocols to extract stress-strain curves and viscoelastic properties from the load-displacement data generated from spherical nanoindentation on materials exhibiting time-dependent response at room temperature. Once these protocols are developed they can then be applied, in the future, to study viscoelastic and viscoplastic properties of various mesoscale constituents of composite material systems. These new protocols were developed and tested on polymethyl methacrylate, polycarbonate, low-density polyethylene, and the bio-polymer chitosan. The properties extracted were consistent under different conditions and we were able to produce stress-strain curves for different loading rates and different indenter tip sizes. This dissertation demonstrates that a set of protocols can be used to reliably investigate the mechanical properties and deformation behavior of time-dependent materials using nanoindentation.

CHAPTER 1: INTRODUCTION

Extensive advances in imaging and property measurement techniques, at the micro-scale, over the past few decades have allowed researchers to gain new insights into the mechanics of engineering materials, biological materials, and advanced composites. In the design of many advanced composite materials, the goal is to fabricate lightweight, strong, and tough materials, generally by reinforcing soft materials such as polymers. Composites are also very popular in biomedical applications where they are used for bone replacement, cartilage replacement, bone cement, screws and many other applications [1]. There has been recent interest in the application of biological principles in the design of stronger, tougher, and "greener" materials [2-5]. Several studies mimic materials that match the properties of the natural material or are even stronger and tougher [4-11].

There is considerable ongoing research into how such composites achieve better properties than their individual constituents display on their own. To investigate this property amplification we have to understand the mechanical properties at the scale in which the separate constituents interact, and not just the macroscale where the effective property of the composite is defined. Also successful application of devices at small length scales can only be guaranteed if their mechanical properties at the low length scales are known. An understanding of the deformation behavior of materials requires knowledge of the local stress-strain behavior of individual microstructural phases and constituents. While there are tools to characterize mechanical response of materials at

such scales [12-15], multiple data analysis procedures and assumptions lead to disparate results even on the same materials.

One method that has been successfully applied to characterize mechanical properties of hard materials is nanoindentation. Nanoindentation has a high load resolution, depth sensing capabilities, and can be used to characterize the local mechanical behavior in material systems with heterogeneous microstructures [16]. Indentation data analysis methods recently developed by our research group have demonstrated a great potential to transform the raw load-displacement data obtained using spherical indenters into indentation stress-strain curves [17]. These protocols have been able to capture the local loading and unloading elastic moduli, the local indentation yield strengths, and some post-yield behavior in several samples [18, 19]. The validity of the definitions of indentation strain and contact radius used by these protocols have been critically evaluated using finite element models [20]. By recovering indentation stress-strain curves from the measured indentation load-displacement data we can get a reliable comparison of material behavior between different samples without the need for expensive and time consuming uniaxial mechanical tests. These protocols have thus far been explored mostly on materials that do not experience significant time-dependent deformation.

To be able to apply the indentation stress-strain methods to polymer composites, we have to first develop analysis techniques that will work for materials that exhibit viscoelasticity. In much of current research, the viscoelastic material properties are extracted after the material has been deformed enough to initiate plasticity and in some cases the time dependence of the deformation is ignored. These methods do not give an

accurate representation of the material properties of the undeformed sample or the local deformation behavior of the material. This dissertation develops analysis protocols to extract stress-strain curves and viscoelastic properties from the load-displacement data generated from spherical nanoindentation on materials exhibiting time-dependent response at room temperature. Once these protocols are developed they can then be applied, in the future, to study viscoelastic and viscoplastic properties of various mesoscale constituents of composite material systems, including both interior regions as well as those near interfaces. The central goals of this PhD thesis are to develop and demonstrate these new protocols through selected case studies on a range of materials that include commercial polymers and the bio-polymer chitosan.

This dissertation is divided into six chapters. In Chapter 2, background information is given for general viscoelasticity, nanoindentation, and the data analyses procedures used in current literature. In Chapter 3, a new set of protocols for extracting stress-strain curves and viscoelastic properties from nanoindentation testing of viscoelastic materials is presented. In Chapter 4, this protocol is tested on three commercially available polymers; polymethyl methacrylate (PMMA), polycarbonate (PC), and low-density polyethylene (LDPE) using three different indenter sizes. The properties and stress-strain curves obtained from nanoindentation are compared against results obtained from conventional uniaxial compression tests performed on the same polymers at a similar strain rate. Finite element (FE) simulations of spherical nanoindentation and uniaxial compression are also performed to understand this deformation behavior under idealized conditions. The results from the FE simulations help us get a better grasp of the results of the experimental work and determine the

relationship between uniaxial compression stress-strain curves and indentation stress-strain curves for viscoelastic materials. In Chapter 5, the protocol is tested on a biopolymer, chitosan. The properties obtained from nanoindentation are once again compared against properties obtained from conventional tensile testing of thin films of the biopolymer. Chapter 6 summarizes and concludes the dissertation.

CHAPTER 2: BACKGROUND

2.1. Viscoelastic Materials

The mechanical response of viscoelastic materials can be characterized in a number of deformation modes including shearing, bending, torsion, compression, and/or tension. In all of these deformation modes, materials generally undergo a certain amount of reversible deformation. Any further deformation beyond this reversible limit results in the material not being able to return to its original shape. Viscoelastic materials exhibit both elastic (Hookean) solid and viscous (Newtonian) fluid properties while undergoing deformation. In elastic deformation, a material deforms instantaneously upon loading and returns to its original state when the load is removed. In one dimension and for small strains they follow Hooke's law [21]:

$$\sigma(t) = K\varepsilon(t) \tag{1}$$

with K as the Elastic modulus, σ as the stress response, and ε as the applied strain. Viscous fluids, however, do not have a tendency for deformational recovery and resist only shear flow. In viscous flow, the rate of deformation increases with increasing applied stress; there is often a time delay between the applied maximum stress and the resultant maximum strain and vice versa. Under shear stress, a viscous fluid obeys:

$$\sigma(t) = \eta \frac{d\varepsilon(t)}{dt} \tag{2}$$

with η as the viscosity.

In viscoelastic materials, the relationship between stress and strain depends both on time and temperature. Only the time dependence will be considered in this dissertation. In elastic materials, stress and strain have a linear relationship (Figure 1a),

whereas for viscoelastic materials there is a strain rate dependence on the stress-strain relationship (Figure 1b). Some characteristics observed in viscoelastic materials, a couple of which will be discussed in the next sections, are:

1. constant stress leads to strain increase with time (creep);

2. constant strain leads to stress decrease with time (relaxation);

3. effective stiffness depends on rate of load application;

4. hysteresis (phase lag) occurs if cyclic loading is applied;

5. rebound of an object after impact is less than 100%.
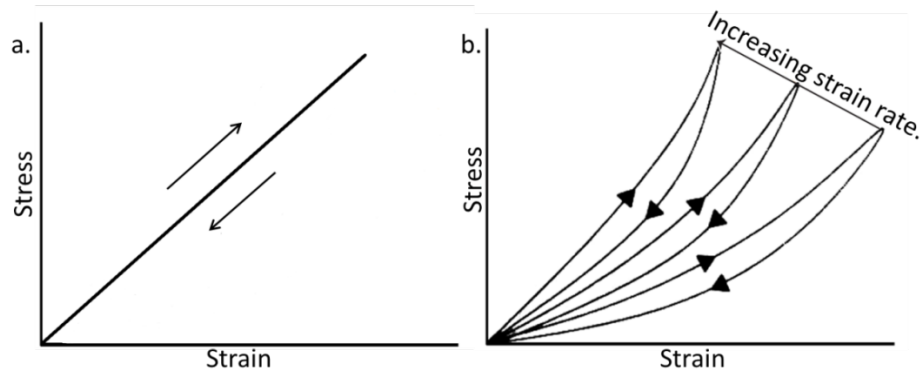
Figure 1 - Stress-strain plots for loading and unloading at different strain rates. (a) Ideal elastic material. (b) Linearly viscoelastic material.

2.1.1. Stress Relaxation

Stress relaxation in viscoelastic materials occurs when they relieve stress under constant strain. This is best exemplified when a single step function is applied as the strain history with a magnitude ε_0: $\varepsilon(t) = \varepsilon_0 H(t)$ (Figure 2a). $H(t)$ is the Heaviside unit step function which is zero for negative t and one when t is greater than zero. If the material is a perfectly elastic solid, the corresponding stress history would be of the form $\sigma(t) = \sigma_0 H(t)$ which is constant for all positive t (Figure 2b). If the material is a perfectly

viscous fluid, the stress would be instantaneously infinite at the application of the strain and then zero for all positive t (Figure 2b). In a viscoelastic material the stress, $\sigma(t)$, will decrease with time as shown in Figure 2b and the ratio [22],

$$E(t) = \frac{\sigma(t)}{\varepsilon_0} \tag{3}$$

is called the relaxation modulus which is independent of the strain level in linearly viscoelastic materials. Relaxation can also occur in shear or volumetric deformation. For shear stress the shear relaxation modulus is $E_s(t)$ and for volumetric deformation the bulk relaxation modulus can be defined as $E_B(t)$ with the stress as hydrostatic stress. If the strain is released at a later time, the stress will recover depending on the material in the following manner. For perfectly elastic materials, the stress will recover to zero immediately whereas for perfectly viscous materials, there will be an instant infinite amount of residual stress at the release of the strain and then zero after that. For a viscoelastic material, it will induce a certain amount of residual stress which will progressively increase to zero.
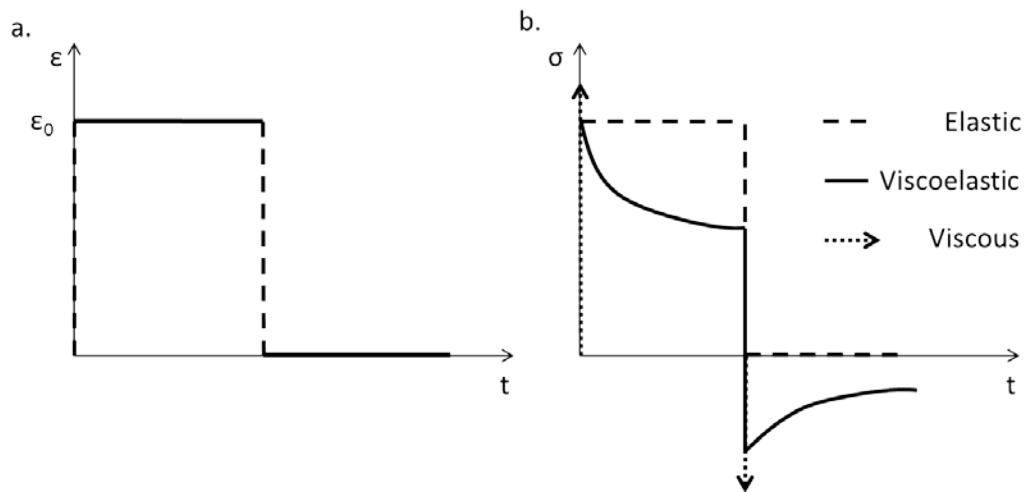
Figure 2 – (a) A step increase and decrease in strain and the (b) resulting stress response.

7

2.1.2. Creep

Creep in viscoelastic materials occurs when they deform under constant stress. This is best exemplified when a single step function is applied as the stress history with a magnitude σ_0: $\sigma(t) = \sigma_0 H(t)$ (Figure 3a). For a perfectly elastic solid, the strain response would be of the form $\varepsilon(t) = \varepsilon_0 H(t)$ for all positive t. For a perfectly viscous fluid, the strain history would increase at a constant rate and be of the form $\varepsilon(t) = \sigma_0 t/\eta$. For a viscoelastic material, the strain $\varepsilon(t)$ will increase with time as shown in Figure 3b and the ratio [22],

$$J(t) = \frac{\varepsilon(t)}{\sigma_0}$$

(4)

is called the creep compliance which is independent of the stress level in linearly viscoelastic materials. Creep can also occur in shear, $J_s(t)$, extension, $J_E(t)$, and volumetric deformation, $J_B(t)$. If the load is released at a later time, the strain will recover in different ways in the different classes of materials. For perfectly elastic materials, the strain will recover to zero immediately, whereas for perfectly viscous materials, the strain remains constant. For a viscoelastic material, there is an initial drop in strain equal to the step strain applied after which the strain progressively decreases to zero.
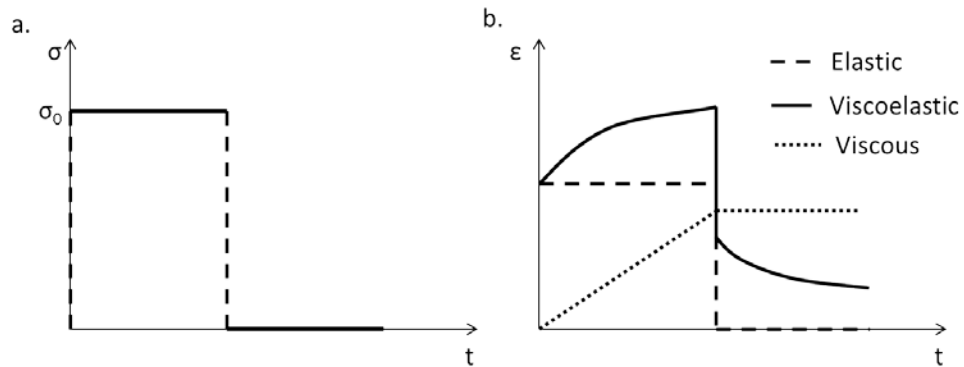
Figure 3 - (a) A step increase and decrease in stress and the (b) resulting strain response.

2.1.3. Constitutive Relationships

Practical applications of viscoelastic materials rarely involve keeping them under constant load or extension, so it is important to understand the material's response to an arbitrary load or displacement history. To understand this, it is important to develop constitutive equations that describe the fundamental material behavior. Boltzmann generalized the behavior observed in the previous two section and formed the superposition principle which states that the net response caused by two or more stimuli is the sum of the responses of the individual stimuli. Consider an increment in strain over a small time interval:

$$d\varepsilon(\tau) = \frac{d\varepsilon(\tau)}{d\tau} d\tau \tag{5}$$

Assuming the stress is continuous and differentiable in time and strain is related to stress via the relaxation modulus (equation (3)), Boltzmann suggested that an increment in stress is related to the increment in strain at time increments from τ to t through the relaxation modulus as:

$$d\sigma(t) = E(t - \tau) \frac{d\varepsilon(\tau)}{d\tau} d\tau \tag{6}$$

The complete stress at any time t can then be obtained by integrating over all the increments:

$$\sigma(t) = \int_0^t E(t - \tau) \frac{d\varepsilon(t)}{d\tau} d\tau \tag{7}$$

Performing the same process for an arbitrary stress history, a complimentary relation may be obtained:

$$\varepsilon(t) = \int_0^t J(t - \tau) \frac{d\sigma(t)}{d\tau} d\tau \tag{8}$$

If the material response to a step stress or strain can be determined experimentally, the response of a linear viscoelastic material to any load history can be found. Experimentally applying a step stress or strain is not feasible, so the usual procedure is to apply the stress or strain at the fastest rate that the machine allows and hold it at a preset value. This ramp loading can be taken into consideration when extracting the creep compliance or relaxation modulus from such tests as will be shown in the next chapter.

Since this is the one dimensional form of the constitutive relationships, a three dimensional form needs to be developed to be applicable to all cases. This relationship for an arbitrary strain history can be written as [23]:

$$\sigma_{ij}(t) = \int_{-\infty}^{t} E_{ijkl}(t-\tau)\frac{d\varepsilon_{kl}(\tau)}{d\tau}d\tau \tag{9}$$

where the fourth-order tensor $E_{ijkl}(t)$ is the relaxation modulus of the material and for an isotropic material is represented as:

$$E_{ijkl}(t) = G(t)\big(\delta_{ik}\delta_{jl} + \delta_{il}\delta_{jk}\big) + (K(t) - 2/3K(t))\delta_{ij}\delta_{kl} \tag{10}$$

The scalar $G(t)$ is the relaxation modulus in shear and $K(t)$ is the bulk relaxation modulus. This relationship can also be extended to an arbitrary stress history as [23]:

$$\varepsilon_{ij}(t) = \int_{-\infty}^{t} J_{ijkl}(t-\tau)\frac{d\sigma_{kl}(\tau)}{d\tau}d\tau \tag{11}$$

where the fourth-order tensor $J_{ijkl}(t)$ is the creep compliance of the material and for an isotropic material is represented as:

$$J_{ijkl}(t) = J_s(t)\big(\delta_{ik}\delta_{jl} + \delta_{il}\delta_{jk}\big) + (J_B(t) - 2/3J_s(t))\delta_{ij}\delta_{kl} \tag{12}$$

The scalar $J_s(t)$ is the creep compliance in shear and $J_B(t)$ is the bulk creep compliance. These three-dimensional representations of the viscoelastic constitutive equations can be used to describe the full range of material behavior under any deformation condition.

In some case, the time dependent shear modulus or bulk modulus may need to be derived from the relaxation modulus. To get this relationship for an isotropic viscoelastic material, the correspondence principle can be used to get the Laplace transformed moduli [24] and the convolution theorem can be used to get the viscoelasticity relationships [25, 26] as:

$$E(t) = 2\left[G(t) + \int_{-\infty}^{t} v(\tau)G(t-\tau)\,d\tau\right] \tag{13}$$

$$E(t) = 3\left[K(t) - 2\int_{-\infty}^{t} v(\tau)K(t-\tau)\,d\tau\right] \tag{14}$$

If the Poisson's ratio has very little variance or is assumed to be constant, the relationships reduce to:

$$G(t) = \frac{E(t)}{2(1+v)} \tag{15}$$

$$K(t) = \frac{E(t)}{3(1-2v)} \tag{16}$$

which is similar to the elasticity relationships. The most significant change of Poisson's ratio for most polymers is during the glass-to-rubber transition. As the operating temperature gets further from that region, the ratio is relatively constant. Since all experiments will be performed at temperatures much lower or higher than the glass transition temperature, the assumption of constant Poisson's ratio is a reasonable one.

2.1.4. Relation between Creep and Relaxation

In cases where only the creep compliance or the relaxation modulus can be calculated, it is important to obtain a relationship between both functions. The viscoelastic stress-strain relationships can be manipulated using integral transforms, such as the Laplace transform, to convert a linear integral equation or a linear differential equation to an algebraic equation that is easier to solve. Using the derivative and convolution properties of the Laplace transform, equations (9) and (11) can be converted to $\sigma_{ij}(s) = sE_{ijkl}(s)\varepsilon_{kl}(s)$ and $\varepsilon_{ij}(s) = sJ_{ijkl}(s)\sigma_{kl}(s)$ respectively where s is the transform variable. This leads to the relationship,

$$\frac{\sigma_{ij}(s)}{\varepsilon_{kl}(s)} = sE_{ijkl}(s) = \frac{1}{sJ_{ijkl}(s)} \tag{17}$$

The equation can then be simplified to,

$$E_{ijkl}(s)J_{ijkl}(s) = \frac{1}{s^2} \tag{18}$$

Using the convolution property, $L[t] = 1/s^2$, and taking the inverse transform, the following relationship is obtained,

$$\int_0^t J_{ijkl}(t-\tau)E_{ijkl}(\tau)d\tau = \int_0^t E_{ijkl}(t-\tau)J_{ijkl}(\tau)d\tau = t \tag{19}$$

These are the implicit relationships. If a specific analytical form is known for the relaxation function or creep function, the explicit relationship can be formulated using Laplace transforms as will be developed for the viscoelastic nanoindentation case.

2.1.5. Mechanical Models for Viscoelasticity

Mechanical models composed of springs, assumed to be perfectly elastic, and dashpots, assumed to be perfectly viscous, are generally used to investigate the

viscoelastic behavior of materials. The spring can be described by Hooke's law, equation (1), and the dashpot can be described as a viscous fluid, equation (2). To develop generalized mechanical models and finite networks for representation of viscoelastic behavior in general, a number of basic one-dimensional models are often used. These models will eventually be extended to more general cases to develop terms for creep compliance and relaxation modulus.

2.1.5.1 Maxwell Model

The first is the Maxwell model which is a combination of a linear spring and dashpot connected in series as shown in Figure 4a. Assuming quasistatic deformation, inertia is neglected and the stress is the same in both elements meaning that the total strain and strain rate is the sum of the individual strain and strain rate of each element respectively. Therefore the sum of the strain rates for the Maxwell model will be:

$$\dot{\varepsilon}(t) = \dot{\varepsilon}_s(t) + \dot{\varepsilon}_d(t) = \frac{1}{K}\frac{d\sigma(t)}{dt} + \frac{\sigma(t)}{\eta} \tag{20}$$

where the subscripts s and d denote the spring and dashpot respectively. The ratio of viscosity to stiffness, $t_R = \eta/K$, is called the relaxation time and characterizes one of the viscoelastic properties of the material [22]. Equation (20) can then be used to get the response of any arbitrary loading history for the Maxwell model. If this model is subjected to a step strain ε_0, as shown in Figure 4b, the stress response is obtained as:

$$\sigma(t) = K\varepsilon_0 e^{-t/t_R} \tag{21}$$

which describes the stress relaxation phenomenon for the model under constant strain and the stress relaxation function E(t) can be obtained by dividing the stress as function of time by the initial strain. Also from Equation (21), we can see that when $t = t_R$, only 37%

of the initial stress remains. So the relaxation time can also be defined as the time it takes

for the stress to drop to 37% of its initial value under application of a constant strain. If

the model is subjected to a step stress σ_0, as shown in Figure 4c, the strain response is

obtained as:

$$\varepsilon(t) = \frac{\sigma_0}{K} + \frac{\sigma_0}{\eta} t \qquad (22)$$

which describes the creep phenomenon for the model under constant stress and the creep

compliance J(t) can be obtained by dividing the strain as a function of time by the initial

stress. This model inaccurately describes creep, since the creep compliance has a constant

slope, in contrast to the exponential decay versus time observed experimentally.
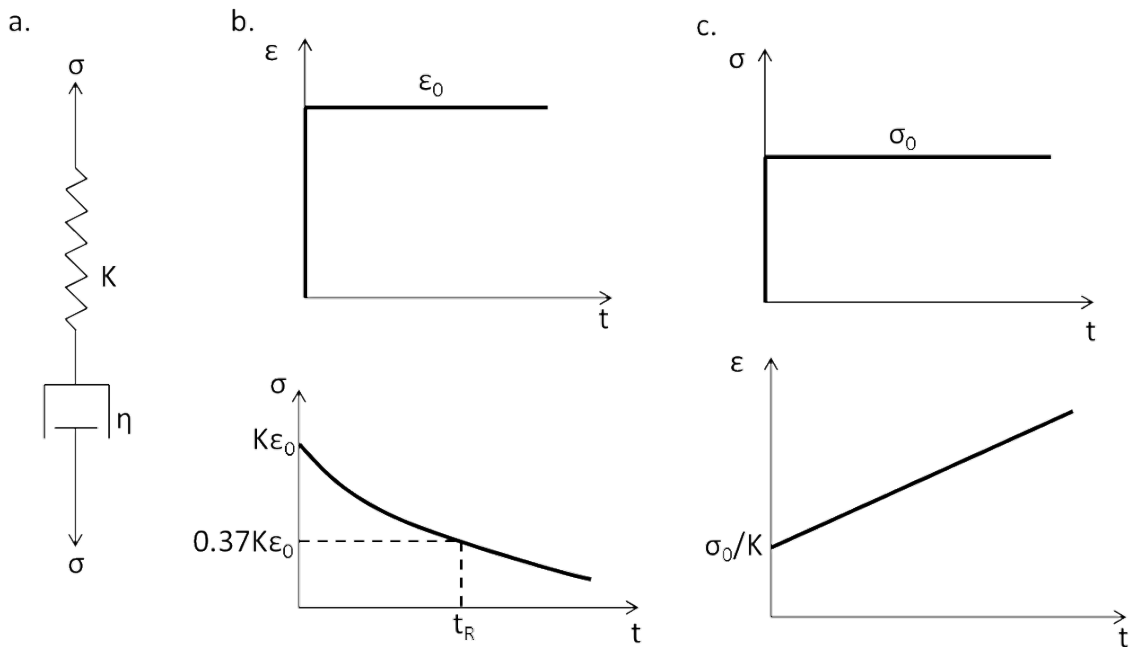
Figure 4 - (a) Maxwell model (b) behavior under applied step strain and (c) behavior
under applied step stress.

<u>2.1.5.2. Kelvin Model</u>

Another commonly used simple is the Kelvin model which is a combination of a linear spring and dashpot connected in parallel as shown in Figure 5a. In this case the strain will be the same in both elements and the total stress will be the sum of the individual stress of each element. Therefore the total stress in the Kelvin model will be:

$$\sigma(t) = \sigma_s(t) + \sigma_d(t) = K\varepsilon(t) + \eta \frac{d\varepsilon(t)}{dt} \tag{23}$$

As with the Maxwell model, the properties can be studied in a similar manner. If the model is subjected to a step strain ε_0, as shown in Figure 5b, the stress response is obtained as:

$$\sigma(t) = K\varepsilon_0 + \eta\varepsilon_0\delta(t) \tag{24}$$

where $\delta(t)$ is the Dirac delta function, which suggests that there will be an infinite stress pulse as soon as the strain is applied and then the response will be a constant thereafter. The relaxation modulus E(t) can be obtained by dividing the stress as a function of time by the initial strain. This case is inaccurate as it does not show the stress relaxation observed experimentally. If the model is subjected to a step stress σ_0, as shown in Figure 5c, the strain response is obtained as:

$$\varepsilon(t) = \frac{\sigma_0}{K}\left(1 - e^{-t/t_c}\right) \tag{25}$$

where $t_C = \eta/K$ is referred to as the retardation time, which is defined as the time it takes the strain to reach 63% of its long term value. The creep compliance J(t) can be obtained by dividing the strain as a function of time by the initial stress.
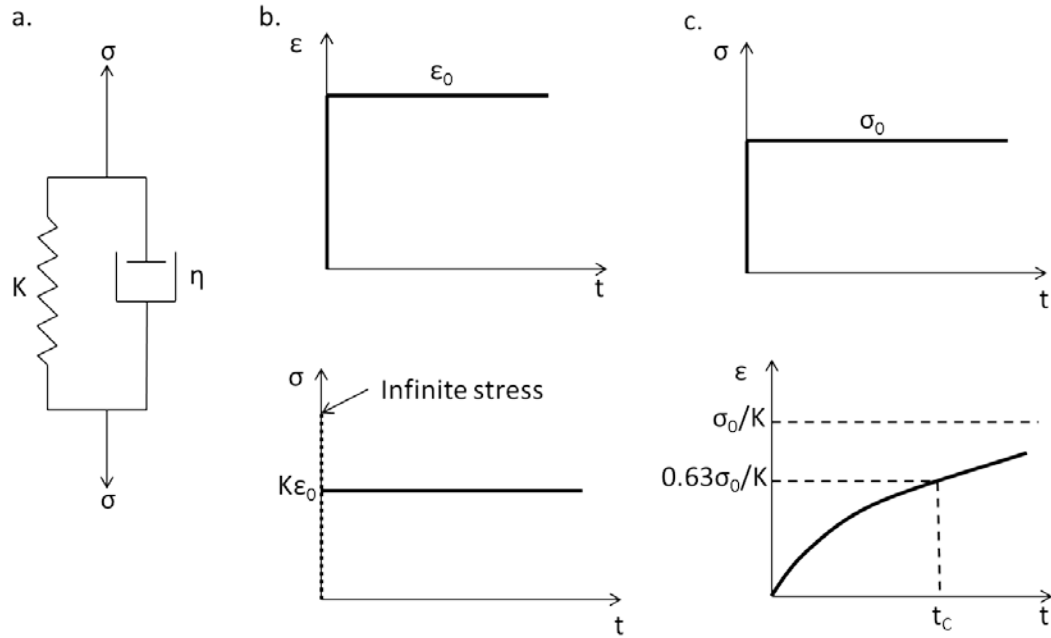
Figure 5 - (a) Kelvin model (b) behavior under applied step strain and (c) behavior under applied step stress.

2.1.5.3. Standard Linear Solid

A more realistic material behavior can be modeled by the standard linear solid, which contains either a Maxwell model in parallel with a spring, as shown in Figure 6a, or a Kelvin model in series with a spring. In this case the model behavior can be described in differential form as:

$$\frac{d\varepsilon(t)}{dt}(K_1 + K_2) + \frac{\varepsilon(t)K_2}{\tau} = \frac{\sigma(t)}{\tau} + \frac{d\sigma(t)}{dt} \tag{26}$$

where τ is either the relaxation time or the retardation time depending on the loading history. To obtain the relaxation response, a step strain can be applied, as shown in Figure 6b, and the equation can be solved using Laplace transforms to get the response and relaxation modulus as [22]:

$$E(t) = K_2 + K_1 e^{-t/t_R} \qquad (27)$$

Using the relationship developed earlier between the relaxation modulus and the creep compliance, we can come up with the creep compliance as:

$$J(t) = \frac{1}{K_2} - \frac{K_1}{K_2(K_1 + K_2)} e^{-t/t_C} \qquad (28)$$
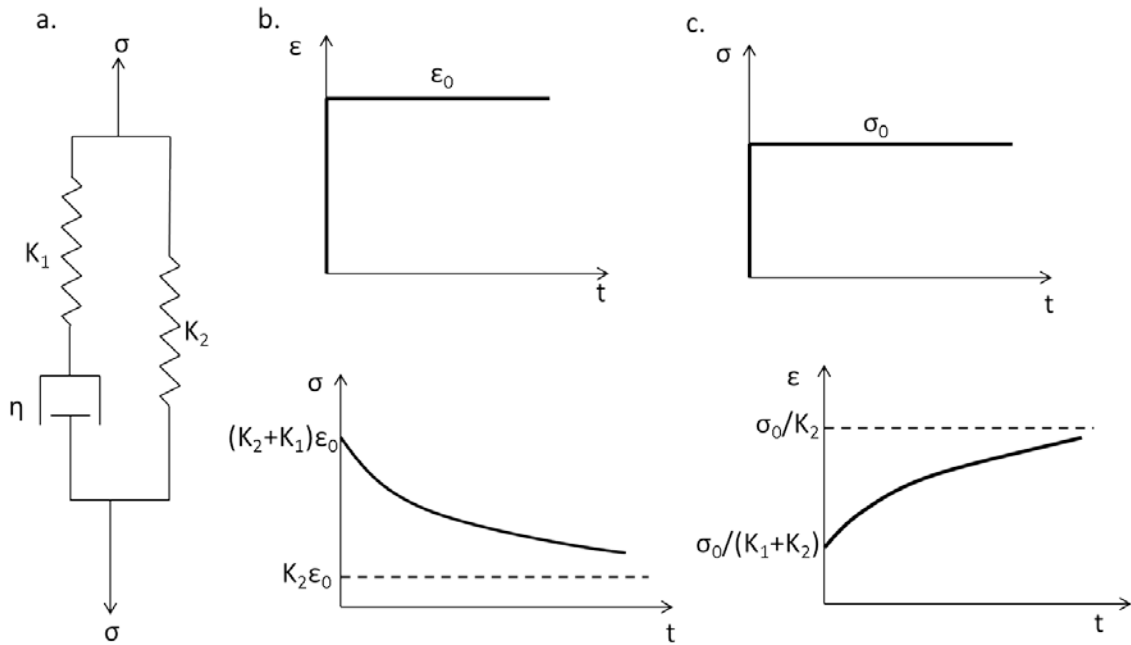
Figure 6 - (a) Standard Linear Solid model (b) behavior under applied step strain and (c) behavior under applied step stress.

These physical models can be extended by adding more springs and dashpots to form more complicated systems, but care has to be taken to relate the models to real material behavior that can be observed by experimentation.

2.1.5.4. Prony Series

    A general representation of the relaxation modulus can be obtained by connecting many Maxwell elements in series, and adding a spring in parallel with the whole array. The relaxation modulus will then have either of the two forms:

$$E(t) = E_\infty + \sum_{i=1}^{N} E_i e^{-t/\tau_i} \tag{29}$$

or

$$E(t) = E_0 - \sum_{i=1}^{N} E_i (1 - e^{-\frac{t}{\tau_i}}) \tag{30}$$

where E_∞ is the steady state stiffness of the system, E_0 is the instantaneous modulus, and E_i and τ_i are the stiffnesses and time constants of the Maxwell elements. The sum of the exponentials is known as the Prony series and is generally used by finite element modeling software to define the properties of time dependent materials. Experimental data from stress relaxation tests can also be fit to equation (29) to determine the Prony series terms. For cases where only creep data is available, a Prony series representation of the creep compliance can be written as:

$$J(t) = J_\infty - \sum_{i=1}^{N} J_i e^{-t/\tau_i} \tag{31}$$

$$J(t) = J_0 + \sum_{i=1}^{N} J_i (1 - e^{-\frac{t}{\tau_i}}) \tag{32}$$

where J_∞ is the steady state stiffness of the system, J_0 is the instantaneous compliance, and J_i and τ_i are the compliances and time constants of the Maxwell elements. If only one function is known, the relationship between the creep function and the relaxation function, described by equation (19), can be used to obtain the other. The shear and bulk relaxation moduli can also be represented in a similar form if either time series is known.

The Prony series is just an example of the most common method of describing viscoelastic behavior and can be used to model a wide range of materials and relaxation times by using the appropriate number of elements.

2.1.6. Viscoelastic Material Property Definition in ABAQUS

The viscoelastic material model used in the FE software ABAQUS defines isotropic rate-dependent behavior assuming the deviatoric and volumetric behaviors are independent in multiaxial stress states. The stress-strain relationship can be described as:

$$\sigma(t) = \int_0^t 2G(\tau - \tau')\dot{e}dt' + I\int_0^t K(\tau - \tau')\dot{\emptyset}dt' \tag{33}$$

where e and $\emptyset$ are the mechanical deviatoric and volumetric strains respectively. τ in this case is the reduced time and is related to the actual time as:

$$\tau = \int_0^t \frac{dt'}{A_\theta(\theta(t'))}, \qquad \frac{d\tau}{dt} = \frac{1}{A_\theta(\theta(t))} \tag{34}$$

where θ is the temperature and A_θ is the shift function. The shift function is used to relate the properties at any temperature to the properties obtained at some reference temperature. So if the relaxation modulus was obtained at one temperature $E(t,\theta_0)$, the relaxation modulus at a different temperature $E(t,\theta)$ can be calculated by using the shift function. Basically $E(t,\theta) = E(A_\theta t,\theta_0)$. If the properties are obtained at the same temperature that the future test will be performed, $A_\theta = 1$ and $\tau = t$. For indentation the properties are collected at approximately the same temperature that the tests are performed.

For a better understanding, the responses can be divided into the shear behavior and the volumetric behavior. If a time varying shear strain, γ, is applied to the material, the shear stress, τ, is defined as:

$$\tau(t) = \int_0^t G(t-s)\dot{\gamma}(s)ds \tag{35}$$

If a time varying volume strain, ε^v, is applied to the material, the hydrostatic pressure, p, is defined as:

$$p(t) = -\int_0^t K(t-s)\,\dot{\varepsilon}^v(s)ds \tag{36}$$

To numerically implement this material behavior, a Prony series of the shear and bulk relaxation moduli in a dimensionless form is used. This is done by dividing the shear relaxation modulus by the instantaneous shear modulus, g(t) = G(t)/G$_0$, and the bulk relaxation modulus by the instantaneous elastic bulk modulus, k(t) = K(t)/K$_0$, which gives:

$$g(t) = 1 - \sum_{i=1}^{n_G} g_i \left(1 - e^{-\frac{t}{\tau_i^G}}\right) \tag{37}$$

$$k(t) = 1 - \sum_{i=1}^{n_K} k_i \left(1 - e^{-\frac{t}{\tau_i^K}}\right) \tag{38}$$

ABAQUS assumes τ^K and τ^G are equal but n_K and n_G need not be equal. In applications where the viscoelastic response is dominated by the deviatoric behavior, it can be assumed $n_K = 0$. Due to the heterogeneous nature of the stress state within the material during nanoindentation and the confined material, both shear and deviatoric behavior will be expected. Therefore it is important to consider both modes of behavior during the simulations.

2.2. Nanoindentation

Indentation tests were originally performed by Brinell, using ball bearings as indenters to measure the plastic properties of materials [16]. In traditional indentation, an indenter of known geometry is driven into a softer sample by applying a set force or displacement. An optical image is then taken of the indent and the dimensions of the resultant imprint are correlated to a hardness index number. With higher resolution equipment, it is now possible to continuously control and monitor the load and displacement of the indenter as it is driven into and withdrawn from the material and produce load-displacement curves as shown in Figure 7a. This is known as instrumented indentation testing or depth sensing indentation and for sub-micron resolutions, nanoindentation. Nanoindentation has significant advantages over the traditional indentation, since the material properties can now be probed from depths as small as a few nanometers, using proper analysis techniques [27]. Nanoindentation has been used to measure the local hardness, elastic modulus [28, 29], evaluate the plastic response of metals [30-33], calculate the fracture toughness of brittle materials [34, 35], and measure the viscoelastic properties of polymers [36-39]. It should be noted that the majority of research is focused on hard materials such as metals and ceramics and the indents are performed with sharp tip indenters rather than spherical indenters.
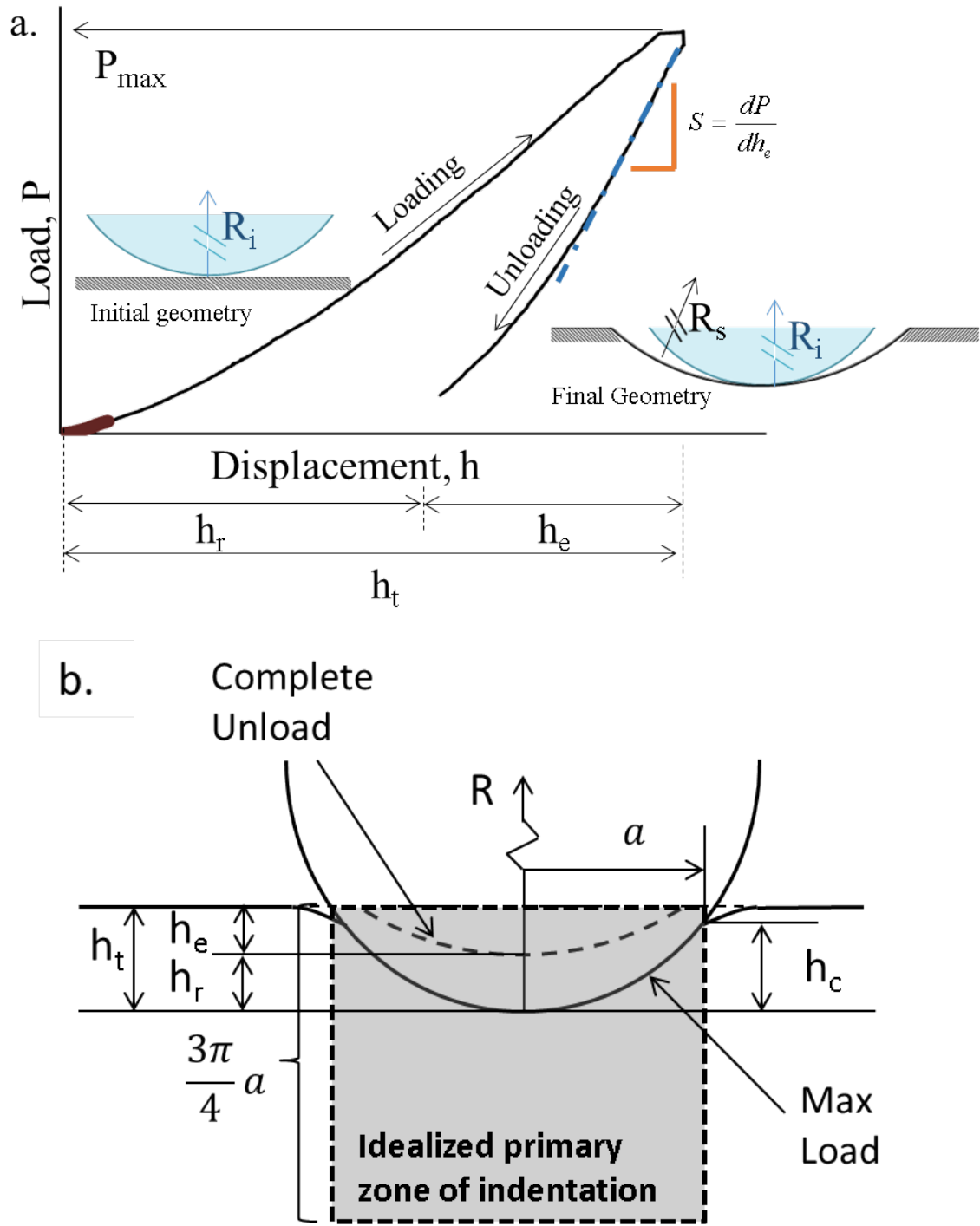
Figure 7 - (a) Typical indentation load-displacement curve with initial and final contact geometry. (b) Schematic of Spherical indentation. [17]

2.2.1. Elastic Nanoindentation

Elastic-plastic nanoindentation on metals and ceramics is primarily performed with sharp indenters, such as Berkovich and Knoop indenters [27], which are useful in calculating the hardness [35] and fracture toughness of a material [34]. Sharp indenters produce high stress concentrations under the indenter tip resulting in a very fast transition from elastic deformation to plastic deformation thus making them non-ideal in studying the elastic behavior of a material. On the other hand, spherical indenters provide a slower and smoother transition from elastic deformation to plastic deformation. This transition can be identified, in some cases, from load displacement curves collected during experiments. With certain assumptions [40], it is possible to generate and follow the stress-strain response in a sample from initial elasticity to initiation of plasticity at yield to large plastic strains [41].

Several of the nanoindentation data analysis procedures used in current literature are based on Hertz's theory [42] for frictionless contact between two linear isotropic elastic solids with spherical surfaces as shown in Figure 8. Since the contact area will be circular with a radius of a, the boundary condition for displacement within this region is given by:

$$u_{z1} + u_{z2} = h - \frac{r^2}{2R_{eff}} \tag{39}$$

where $1/R_{eff} = 1/R_1 + 1/R_2$ is the effective curvature of the two bodies and r is the distance from the center of contact to any point within the contact region. For indentation on a flat surface the effective radius is equal to the indenter radius as the sample radius approaches infinity. Hertz proposed a pressure distribution that satisfies this boundary condition as:

$$p(r) = p_o[1 - (r/a)^2]^{1/2} \tag{40}$$

where p_o is the maximum pressure at the center of contact. This distribution gives normal

displacements of:

$$u_z = \frac{1 - v^2}{E}\frac{\pi p_o}{4a}(2a^2 - r^2), \qquad r \le a \tag{41}$$

where E, in this case, is the Young's modulus and v is the Poisson's ratio. Since the

pressures on both bodies are equal, an effective modulus of the combined system is

described by:

$$\frac{1}{E_{eff}} = \frac{1 - v_1^2}{E_1} + \frac{1 - v_2^2}{E_2} \tag{42}$$

Substituting this and equation (41) into equation (39), we get:

$$\frac{\pi p_o}{4aE_{eff}}(2a^2 - r^2) = h - \frac{r^2}{2R_{eff}} \tag{43}$$

The total load is then related to the pressure as:

$$P = \int_0^a p(r)2\pi r dr = \frac{2}{3}p_o\pi a^2 \tag{44}$$

In experiments, the total load and displacement are the given outputs, so it is convenient

to rearrange equations (43) and (44) to obtain the general form of Hertz theory used in

literature:

$$P = \frac{4}{3}E_{eff}R_{eff}^{1/2}h_e^{3/2} \tag{45}$$

$$a = \sqrt{R_{eff}h_e} \tag{46}$$
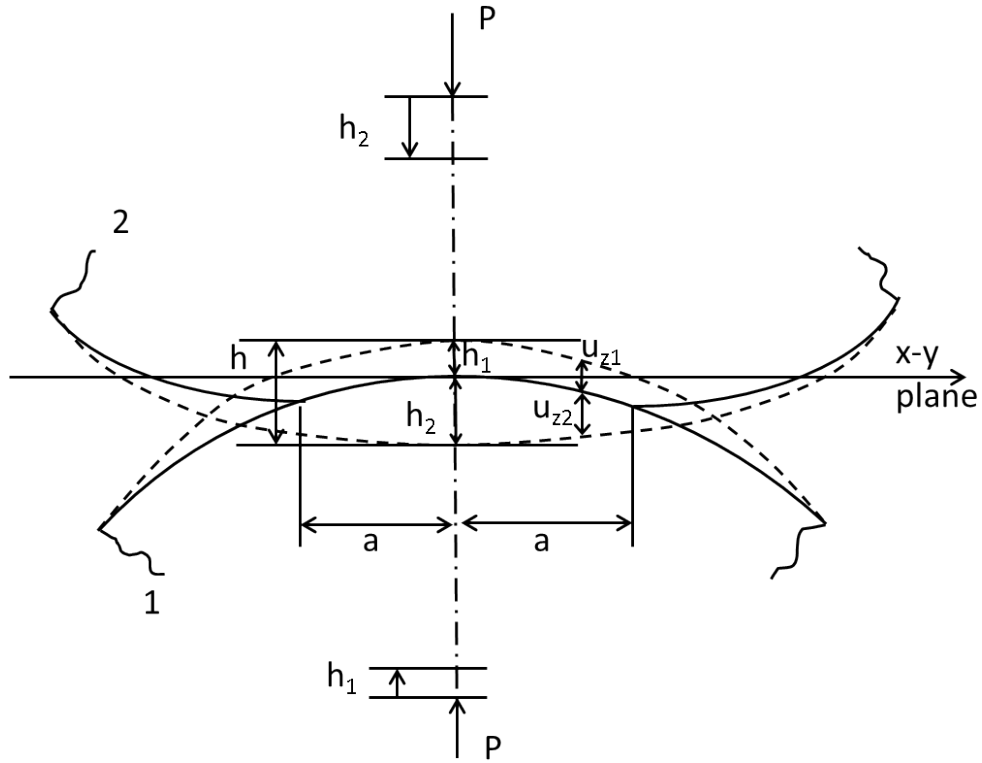
Figure 8 - Contact between two solids of revolution.

On most samples the very small initial elastic loading segment is not clearly identifiable on a measured load-displacement curve, therefore the Hertz model is commonly applied to the unloading segment as it is assumed to be primarily elastic [29, 43, 44]. The sample usually experiences significant inelastic strains before unload, especially with sharp indenters, so the unloading is no longer from a flat undeformed sample surface. A direct measurement of R_s or a is extremely difficult, due to the positioning and scale of the indentation, so most researchers calibrate the projected contact area using measurements on samples with known moduli [45] or from finite element simulations [46]. This approach assumes that the result from the calibration is independent of the material being indented which is unlikely since indentation on different materials would produce different contact geometries.

2.2.1.1. Zero-Point Correction

The first step in the analysis of raw load-displacement data obtained from an indentation test is the accurate estimation of the point corresponding to zero-load and zero-displacement. This will have a major influence on the estimation of the contact radius and values of indentation stress and strain. Our research group finds this point by performing a regression analysis on the initial elastic loading segment of the measured load, displacement, and stiffness signals and fitting it to the expected relationships predicted by Hertz's theory [17]. As a result, an 'effective' point of initial contact is identified which relates to a virtual flat surface free from any sample preparation artifacts, like surface roughness or oxide layers. Another advantage of an effective point of initial contact is that it automatically produces a good looking indentation stress-strain curve for the loading segment compared to the spikes caused by using the zero point from the nanoindenter's default procedures [17].

A very useful signal provided by the Agilent Nanoindenter G200 is the continuous stiffness measurement (CSM) which provides the elastic stiffness (S) as an independent measurement. This is accomplished by imposing a small, sinusoidally varying load on top of the DC signal that drives the motion of the indenter, as shown in Figure 9, which allows for continuous measurement of the resulting amplitude and phase of the displacement oscillation [47]. Agilent have found that an oscillation frequency of 45 Hz works best for the machine dynamics resulting in the best signals. 45 Hz will be used for all indentation tests in this work.

These superimposed oscillations can produce errors in the resulting raw data since the machine records the average values and not the actual load and displacement that the

material experiences. The material actually experiences the load and displacement of the

maxima of the superimposed oscillations and this error can be corrected using the

following equations [48]:

$$P_{act} = P_{app} + \frac{\Delta P}{2} \quad \text{or} \quad P_{act} = P_{app} + \sqrt{2}\Delta P_{rms} \tag{47}$$

$$h_{act} = h_{app} + \frac{\Delta h}{2} \quad \text{or} \quad h_{act} = h_{app} + \sqrt{2}\Delta h_{rms} \tag{48}$$

$$S_{act} = \frac{1}{\sqrt{2\pi}} \frac{P_{max}}{\Delta h_{rms}} \left(\frac{1}{K}\right)^{1/m} \left[1 - \left(1 - \frac{2\sqrt{2}\Delta h_{rms}S_{app}}{P_{max}}\right)\right] \tag{49}$$

where P, h, and S refer to the load, displacement, and stiffness signals, respectively, and

the subscripts act and app refer to the actual value experienced by the material and

apparent value measured by the machine respectively. ΔP and Δh are the peak to peak

load and displacement ranges and the root mean squared (rms) values are provided by the

machine. K and m are constant values which are functions of the indenter geometry (K =

0.6524 and m = 3/2 for spherical indentation) [49]. These corrections are applied to the

load, displacement, and stiffness signals measured by the indenter.
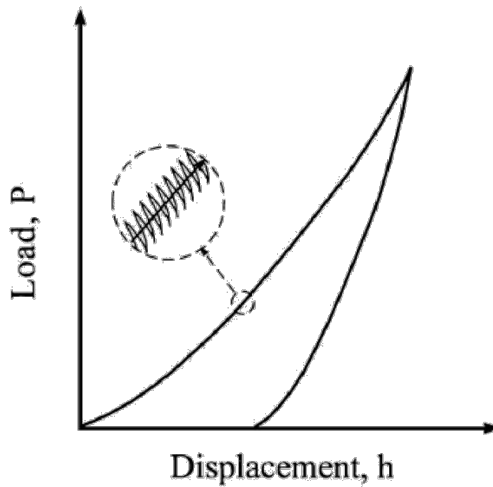
Figure 9 - Sinusoidally varying load applied on top of the DC signal.

To define an effective point of initial contact, start by letting P_1, h_{e1}, and S be the measured load signal, measured displacement signal, and elastic stiffness signal in the initial elastic loading segment from the machine, respectively. Let P^* and h^* denote the values of load and displacement at the effective point of contact. According to Hertz's theory [48], the three signals can be related as:

$$S = \frac{3P}{2h_e} = \frac{3(P_1 - P^*)}{2(h_{e1} - h^*)} \tag{50}$$

Rearranging equation (50) we get:

$$P_1 - \frac{2}{3}Sh_{e1} = P^* - \frac{2}{3}Sh^* \tag{51}$$

Plotting the left hand side of equation (51) against S produces a linear relationship whose slope is equal to $-(2/3)h^*$ and the y-intercept is equal to P^*. This gives us the point of effective initial contact accurately while making sure that the data is consistent with Hertz's theory.

2.2.1.2. Elastic Modulus

There are two ways to determine the elastic modulus of the material. The first, commonly used in literature, is to extract the elastic modulus from the unloading curve. This is done by recasting the Hertz's model (equation (45)) as:

$$E_{eff} = \frac{S}{2a} = \frac{S}{2}\sqrt{\frac{\pi}{A}} \tag{52}$$

where S is the slope of the curve (dP/dh_e) at or close to the peak indentation load and A is the projected contact area defined as:

$$A = \pi a^2 \qquad a = \sqrt{2h_c R_i - h_c^2} \tag{53}$$

In equation (53), h_c is the depth of the indenter that is in contact with the sample as shown in Figure 7b. This definition of contact area uses the actual contact area estimated from simple geometry of a chord length relation as opposed to equation (46) which is the equivalent elastic contact radius consistent with Hertz's theory. Oliver and Pharr [45] proposed the following expression for computation of h_c:

$$h_c = h_t - \frac{1}{2} h_e = h_t - \frac{3}{4} \frac{P}{S} \tag{54}$$

where h_t is the total depth moved by the indenter system and h_e is the elastic depth which as can be seen from Figure 7a is the total depth minus the depth after unloading.

The second method is to determine the elastic modulus from the initial loading curve. This is achieved by rearranging Hertz's theory to the form:

$$P^{2/3} = \left(\frac{4}{3} E_{eff} R_{eff}^{1/2} \right)^{2/3} h \tag{55}$$

So a plot of $P^{2/3}$ vs h of the initial portion of the load-displacement curve should have a section with a constant slope that passes through the origin. Since we are only considering the initial portion starting from a flat surface, $R_i \gg R_s$, we can take $R_{eff} = R_i$. A least squares fit between h and $P^{2/3}$ in the initial segment of the load-displacement data produces the effective modulus. This provides a more accurate description of the elastic modulus as it is extracted from a relatively flat surface and before the material experiences any significant inelastic deformations.

2.2.1.3. Stress-Strain Curves

Common data analysis procedures to define indentation stress and indentation strain transforms equation (45) into a linear relationship as:

$$\sigma_{ind} = \frac{4E_{eff}}{3\pi} \varepsilon_{ind} \qquad \sigma_{ind} = \frac{P}{\pi a^2} \qquad \varepsilon_{ind} = \frac{a}{R_{eff}} \qquad (56)$$

Knowing that $S = dP/dh_e$, equation (45) can be differentiated and the definition of the contact radius in equation (46) can be used to obtain an estimation of the contact radius:

$$a = \frac{S}{2E_{eff}} \qquad (57)$$

In the regime of small indentation depths ($h_c \ll R_{eff}$) equation (56) is the same as the Hertz model. Many researchers have adopted a/R_{eff} [40, 50-52] as the definition of indentation strain due to the expected linear relationship between σ_{ind} and a/R_{eff} in elastic indentation using Hertz's model. Due to difficulty in measuring R_{eff} at each data point, most researchers use a/R_i [40, 50-53] as the definition of indentation strain. This approximation is only valid for the initial elastic loading from a flat sample and breaks down as soon as the material experiences inelastic strain. Also an accurate estimation of the contact tradius needs knowledge of R_{eff} as is seen from equation (45).

Researchers from our group have previously presented and validated new approaches for extracting indentation stress-strain curves for spherical nanoindentation [20, 41, 54, 55]. The first step is providing a more realistic definition of strain to extract the stress-strain curves from the raw load-displacement data. For elastic indentation, the Hertz's model, equation (45), can be recast as:

$$\sigma_{ind} = E^* \varepsilon_{ind} \qquad \sigma_{ind} = \frac{P}{\pi a^2} \qquad \varepsilon_{ind} = \frac{4}{3\pi} \frac{h_t}{a} \approx \frac{h_t}{2.4a} \qquad (58)$$

This new definition of indentation strain uses the total indentation depth instead of the elastic indentation depth which generalizes it for elastic plastic indentations. For elastic indentations, the total depth and the elastic depth are equal and therefore this new definition is consistent with Hertz's theory and is also equivalent to the definition given

by equation (56). The definition idealizes the indentation as being equivalent to compressing a cylindrical region of radius a and height 2.4a by h_t as shown in Figure 7b. This information can now be used with equation (57) to obtain the stress-strain curves for specific material systems. This estimate is only valid for the extraction of stress-strain curves when we assume that E_{eff} remains constant during the inelastic deformation imposed by nanoindentation. This can be applied to most metals as the effective modulus does not change by much throughout the indentation, whereas for viscoelastic materials there is a change even during the elastic portion of the indentation. This novel analysis method has yielded reliable stress-strain curves for aluminum [49], tungsten [17], polycrystalline samples [41], and single crystals [18].

2.2.2. Viscoelastic Nanoindentation

While the previous method has shown highly consistent results with metallic materials, it has yet to be tested on materials that exhibit rate dependent elastic behavior. To be able to apply these new methods to materials that exhibit viscoelasticity, it is important to understand the viscoelastic constitutive relationships for indentation. Theoretical studies on linear viscoelastic indentation started in the mid-1950s with the works of Lee [56], Radok [57], Hunter [58], Graham [59], and Ting [60]. They developed a simple approach to time dependent indentation for finding the viscoelastic solution in cases where the corresponding solution for the purely elastic case is known. This is known as the viscoelastic correspondence principle. This principle for indentation was first derived by Lee and Radok [57] and then later improved for more general cases by Ting [60].

For viscoelastic nanoindentation, an axisymmetric rigid indenter is indenting into a viscoelastic half-space at t = 0. The goal is to find the stresses and displacements in the half-space, which must mathematically satisfy the equation of equilibrium:

$$\frac{\partial \sigma_{ij}}{\partial x_j} = 0 \tag{59}$$

the strain-displacement relationship:

$$\varepsilon_{ij} = \frac{1}{2}\left(\frac{\partial u_i}{\partial x_j} - \frac{\partial u_j}{\partial x_i}\right) \tag{60}$$

and the stress-strain relationships for linear isotropic viscoelasticity:

$$Ms_{ij} = Ne_{ij} \tag{61}$$

$$M'\sigma_{ii} = N'\varepsilon_{ii} \tag{62}$$

where $s_{ij} = \sigma_{ij} - (1/3)\sigma_{kk}\delta_{ij}$ and $e_{ij} = \varepsilon_{ij} - (1/3)\varepsilon_{kk}\delta_{ij}$ are the stress and strain deviators respectively. M, N, M', and N' are linear operators with a time variable and may be differential operators when using mechanical models with springs and dashpots [61] as in section 2.1.5, integral operators for the hereditary-function approach [62] as in section 2.1.3, or other methods of describing viscoelastic behavior.

Consider the case of a smooth rigid sphere indenting into an initially plane surface of a viscoelastic half space at two instants as shown in Figure 10. At any time t that the sphere is in contact with the surface, the contact region will be bounded by a circle of radius a(t). Points that are outside the contact area with a radius r > a(t) will have a boundary condition with zero surface traction. For points inside the contact area, r < a(t), the normal surface displacement is related to contact with the indenter and the tangential component will be zero since the indenter is assumed to be smooth. The surface traction in this region can then be described by:

$$T_i(x_i, t) = \sigma_{ij} n_j \tag{63}$$

where n_j is the unit outward normal vector and x_j are the Cartesian co-ordinates. For the surfaces outside this contact region, only the displacement can be prescribed.
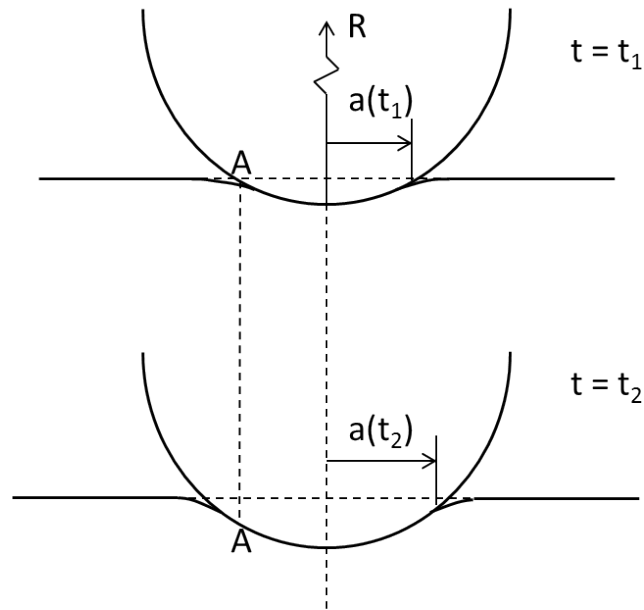
Figure 10 - Indentation of a smooth rigid sphere into a viscoelastic half space at two instants.

In a typical linear viscoelastic model, a solution is available if the regions over which the boundary conditions are defined do not vary during that time. In this case, a Laplace transform is applied to remove the time variable, reducing the problem to an elastic one. Unlike indentation into an elastic half space, the boundary between the two regions shown in Figure 10 has conditions that vary with time. Since for some points on the surface, the traction and displacement are unknown throughout the history of the problem, therefore the transform cannot be obtained. This can be seen in Figure 10, where point A has a boundary condition that changes from time t_1 to time t_2. However,

Radok [63] has suggested that the viscoelastic solution can be obtained by taking the solutions of the elastic problem with the time variable and the same boundary conditions as the viscoelastic problem, and substituting appropriate viscoelastic operators for the elastic constants in the expressions for stress components.

For a contact analysis, the Hertz's solution to the elastic problem (equations (40) and (43)) can be rearranged to give the normal contact pressure as:

$$p(r, t) = \frac{2}{\pi R_{eff}} E_{eff} (a(t)^2 - r^2)^{1/2} \tag{64}$$

This equation appears to be an appropriate form of the elastic spherical nanoindentation solution to substitute viscoelastic operators into, since the surface traction and stress components appear linearly in the basic system of equations. Nonlinearity only appears in the changing geometry of the boundary condition. A relationship for the pressure distribution in an indentation of a viscoelastic half-space by a frictionless sphere can then be formulated as:

$$M[p(r, t)] = \frac{2}{\pi R_{eff}} N[f(r, t)] \tag{65}$$

where,

$$f(r, t) = (a(t)^2 - r^2)^{1/2} \tag{66}$$

Since the indentation progress can be defined by a(t), the surface pressure at each point can be extracted assuming zero initial conditions for the initially undisturbed surface. The problem is now defined by the applied normal surface traction and zero shear traction. Applying the Laplace transform gives an associated elastic problem of $\bar{p}(r, s)$, where the bar indicates the transform and s is the transform parameter. The transform can then be written as:

$$\bar{p}(r,s) = \frac{2}{\pi R_{eff}} \frac{\bar{N}}{\bar{M}} \left[\bar{f}(r,s)\right] \tag{67}$$

where $\bar{M}$ and $\bar{N}$ are the transformed forms of the viscoelastic operators. If the operators used viscoelastic relationships are defined in the integral form, as in section 2.1.3, the transformed form can be formulated as:

$$\bar{\varepsilon}(s) = \bar{J}(s)s\bar{\sigma}(s) \tag{68}$$

so that:

$$\bar{M} = \bar{J}(s)s, \qquad \bar{N} = 1 \tag{69}$$

The corresponding viscoelastic solution can then be obtained by using the transformed viscoelastic operators and performing an inverse Laplace transform.

At any given time during the indentation, to satisfy the Hertz model, the region of contact will be limited to an area A_{max} with a peripheral radius of a_{max}. Looking at Figure 10, a_{max} at time t_2 would $a(t_2)$. Timoshenko and Goodier [64] have shown that for this type of problem the surface displacement can be written as an integral of the surface pressure distribution of the point load elastic solution over the contact area:

$$w(r,t) = \frac{1}{\pi} \iint\limits_{A_{max}} E_{eff} \frac{p(r',t)}{\rho} dA \tag{70}$$

In equation (70) ρ is the distance from the point where the deflection is evaluated to an arbitrary element of area dA and r' is the running radius coordinate over the surface of contact. The elastic constants can then be replaced with the viscoelastic operators and a Laplace transform taken to obtain:

$$\bar{w}(r,s) = \frac{1}{\pi} \iint\limits_{A_{max}} \frac{\bar{M}}{\bar{N}} \frac{\bar{p}(r',s)}{\rho} dA \tag{71}$$

Substituting in the contact pressure from equation (67) then gives:

$$\overline{w}(r,s) = \frac{2}{\pi^2 A_{eff}} \iint\limits_{A_{max}} \frac{\overline{f}(r',s)}{\rho} dA \qquad (72)$$

At any given time, the integral is over a fixed domain A_{max}, therefore the inverse Laplace transform can be performed under the integral sign and the integral only needs to be evaluated within the contact area since it is zero elsewhere. Performing the transform and evaluating the integral gives:

$$w(r,t) = \frac{a(t)^2}{R_{eff}} - \frac{r^2}{2R_{eff}} \qquad (73)$$

which is valid within the contact region, $r < a(t)$, and as long as the surface is in contact with the indenter. This is only valid for nondecreasing contact area since if $a(t)$ reaches a maximum and is then decreased to zero, equation (73) shows that the normal deflection of the surface becomes zero. For viscoelastic materials, a residual impression would be left after the contact has stopped since there are delayed components of elastic and viscous strain. The displacement at the center, $w(0,t)$, also gives the displacement of the indenter:

$$h(t) = \frac{a(t)^2}{R_{eff}} \qquad (74)$$

which gives us the same relationship as the original Hertz model for the elastic case. This means that as long as the contact area is increasing, the displacement for a given contact area during viscoelastic nanoindentation is the same as the elastic nanoindentation case.

The important outputs during indentation are the displacement of the indenter and the total force of penetration. The total force is simply the integral of the pressure distribution over the contact surface:

$$P(t) = \int_0^{a(t)} p(r, t) 2\pi r \, dr \tag{75}$$

For valid elastic solutions, the upper limit can be made constant to get an invariant region of integration since the pressure distribution outside the contact region is zero. Performing the Laplace transform and using the transform from equation (67) gives us:

$$\overline{P}(s) = \frac{2}{\pi R_{eff}} \frac{\overline{N}}{\overline{M}} \int_0^{a_{max}} \overline{f}(r, s) 2\pi r \, dr \tag{76}$$

Taking the inverse transform, the integral reduces to the volume of a hemisphere:

$$P(t) = \frac{4}{3 R_{eff}} \frac{N}{M} a(t)^3 \tag{77}$$

Using the viscoelastic operators from the constitutive relationships for viscoelasticity given by equations (9) and (11) and rearranging everything in terms of load and displacement gives:

$$P(t) = \frac{4\sqrt{R_{eff}}}{3(1 - v^2)} \int_0^t E(t - \tau) \frac{dh^{3/2}(\tau)}{d\tau} d\tau \tag{78}$$

for a prescribed arbitrary displacement history and

$$h^{3/2}(t) = \frac{3(1 - v^2)}{4\sqrt{R_{eff}}} \int_0^t J(t - \tau) \frac{dP(\tau)}{d\tau} d\tau \tag{79}$$

for a prescribed arbitrary loading history. Equations (78) and (79) are commonly used to analyze load-displacement curves obtained from nanoindentation experiments on viscoelastic materials.

2.3. Discrete Deconvolution

The solution to the indentation problem on a linear viscoelastic material is in terms of a convolution integral. Since in a typical indentation test, the load and displacement are measured, the relaxation modulus or creep compliance can ideally be

deconvoluted from the viscoelastic solutions. The data obtained from the indenter is discrete which means the convolution has to be in a discrete form to be deconvoluted. The general form of the convolution integral is:

$$b(t) = \int_0^t A(\tau)x(t-\tau)\,d\tau = \int_0^t A(t-\tau)x(\tau)\,d\tau = A(t) * x(t) \tag{80}$$

where '*' is the convolution operator and $x(t)$ is assumed to be the unknown parameter to be deconvoluted. To approximate the integral by a summation, let ΔT be the sampling interval, and then the discrete form is given by:

$$b(n\Delta T) = \sum_{m=0}^{n\Delta T} A(n\Delta T - m\Delta T)x(m\Delta T)\,\Delta T \tag{81}$$

Each function is now a discrete array and the nth element is the function evaluated at $n\Delta T$. Thus the discrete convolution can be written as:

$$b(n) = \Delta T \sum_{m=0}^{n} a(n-m)x(m) = a(n) * x(n) \tag{82}$$

The summation can be expanded to get:

$$b(n) = \begin{bmatrix} a(0)x(0) \\ a(0)x(1) + a(1)x(0) \\ a(0)x(2) + a(1)x(1) + a(2)x(0) \\ \vdots \\ a(0)x(n) + a(1)x(n-1) + \cdots + a(n)x(0) \end{bmatrix} \Delta T \tag{83}$$

or in matrix form:

$$\begin{bmatrix} a(0) & & & \\ a(1) & a(0) & & \\ \vdots & & \ddots & \\ a(N) & \cdots & \cdots & a(0) \end{bmatrix} \begin{bmatrix} x(0) \\ x(1) \\ \vdots \\ x(N) \end{bmatrix} \Delta T = \begin{bmatrix} b(0) \\ b(1) \\ \vdots \\ b(N) \end{bmatrix} \tag{84}$$

$$AX\Delta T = B$$

where:

$$A_{ij} = \begin{cases} 0 & i < j \\ a(i-j) & \text{otherwise} \end{cases}$$

$$X_i = x(i-1)$$

$$B_i = b(i-1)$$

An estimate $\widehat{X}$ of the unknown parameter can be obtained by using a linear least squares approach to a solution:

$$\widehat{X} = (A^TA)^{-1}A^TB$$

For the viscoelastic nanoindentation solution, once the creep compliance or relaxation modulus is extracted, the estimated solution can be fit to a Prony series to get an idea of the material's instantaneous and long-term moduli or compliance.

2.4. Viscoelastic Nanoindentation in Literature

With advances in technology and the push for advanced engineering materials, there has been considerable interest in the past few years in understanding the micro and sub-micron scale properties of viscoelastic materials. Most studies on nanoindentation focus on extracting the creep compliance or relaxation modulus by fitting the results to a mechanical model or a Prony series representation [36, 37, 65]. Several researchers have used sharp, Berkovich or conical, tips to investigate the viscoelastic behavior of different polymers [66, 67]. It should be noted that in these cases the region deformed under the indenter is plastically deformed, as explained in the previous section, and as such the properties extracted are not representative of the original undeformed viscoelastic material. Some tests extract these properties by fitting the loading portion of the test to the viscoelastic solution whereas others extract them by ramping the load or displacement to a preset number and holding it for some time. The relaxation modulus or creep

compliance can then be extracted from the hold portion. An important study was done by Michelle Oyen [68] to study the assumption of step loading creep conditions. Experimentally, a step loading condition is impossible to implement, therefore it is important to take into account the ramp load before the hold. Oyen has shown the analytical solution for this case and that if a mechanical model is used, a "ramp correction factor" for the exponential decay terms is the only difference between an analytical step loading condition and a ramp loading condition. This is explored in further detail in the next chapter.

Another important property that is commonly studied is a viscoelastic material's response to dynamic (oscillatory) loading at different frequencies [69-71]. This is useful in extracting the storage and loss moduli of the material in the frequency domain for applications where cyclic loading is imposed. The storage and loss moduli are also material properties and combined with tests at different temperatures represent the full spectrum of viscoelastic materials properties before and after its glass transition temperature. While these properties are useful, it is important to develop precise data analysis protocols for nanoindentation of viscoelastic materials at room temperature and for a single loading cycle first. The focus of this dissertation is to develop a concise protocol that provides the mechanical properties of a viscoelastic material at the micron and sub-micron scale accurately. This protocol can be extended, in the future, to different conditions and temperatures to capture the full spectrum of viscoelastic material properties.

CHAPTER 3: NEW VISCOELASTIC NANOINDENTATION PROTOCOLS

The focus of most elastic-plastic nanoindentation tests, in current literature, is to extract the modulus, hardness, or a stress-strain curve, whereas the focus of viscoelastic nanoindentation tests, in current literature, is to extract the creep compliance, relaxation modulus, or storage and loss moduli. The objective of this work is to give any researcher a set of protocols to extract the creep compliance, relaxation modulus, and stress-strain curves from load-displacement curves obtained from nanoindentation experiments on viscoelastic materials. The proposed protocols shall be laid out in steps, starting with an understanding of the material behavior, followed by performing the indentation tests, and finally analyzing the data obtained.

3.1. Step 1: Determine Material Viscoelasticity

The first step is to determine if the material has a big enough viscous component to affect its deformation behavior. This is particularly useful when testing new materials or materials structurally or chemically modified for specific applications. In some cases, the viscous portion is small enough that it is negligible and the material can be treated as an elastic-plastic material. Before any quantitative data can be collected, it is important to make sure that any values being calculated assuming viscoelastic behavior is collected within the viscoelastic region of the load-displacement curve. This can be determined by loading and unloading the material at increasing loads using the same loading rate. At the end of each unload a small load is held on the material and the displacement is allowed to recover. The goal is to observe where the displacement stops decreasing and how this

residual displacement changes at different loads. Ideally if the indentation is still within the viscoelastic regime, the residual displacement will be similar at the different maximum loads. For highly viscoelastic materials, it may take much longer for the material to return to reach a residual value and thus it is hard to quantify the exact position of yield, rather an educated guess is made. Since this is not an exact value, a safe assumption can usually be made on where the elastic behavior of the material ends. To avoid the effect of plasticity, any mechanical properties collected should be within this viscoelastic range.
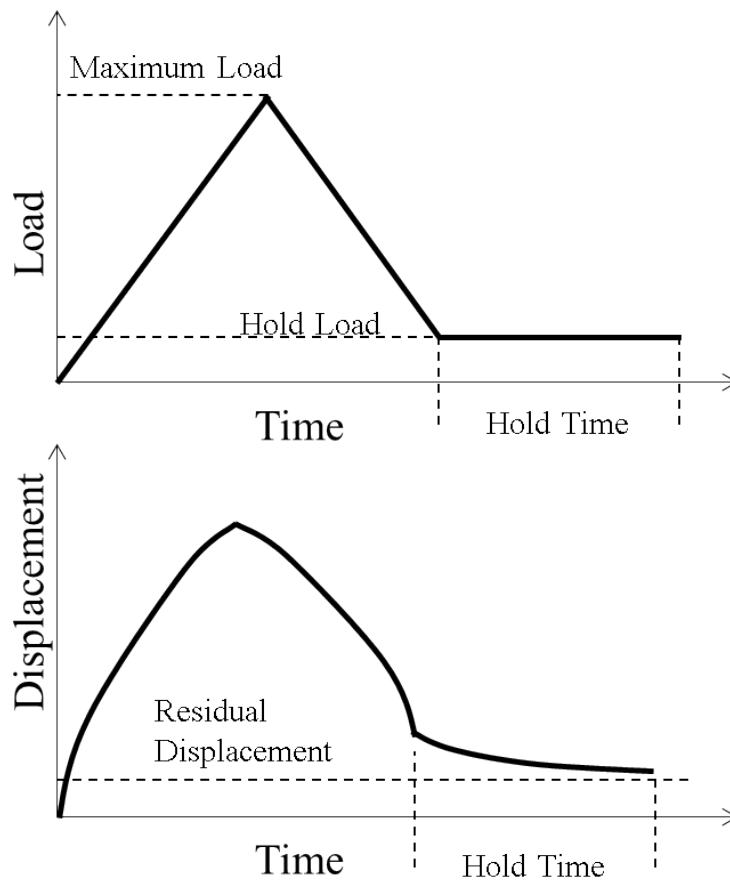
Figure 11 - Schematic of the method used to determining the viscoelastic region.

The best evidence of material viscoelasticity is if the material produces different load-displacement curves in the viscoelastic portion when different deformation rates are applied. Before we test this experimentally in the next chapter, a finite element (FE) study can be performed to formulate the expected behavior for the experiments and confirm some of the analytical solutions for viscoelastic nanoindentation. For all simulations in this thesis, an axisymmetric finite element model was produced using the commercial finite element code ABAQUS. The model consisted of two isotropic bodies, indenter and sample, initially coincident on the axis of symmetry as shown in Figure 12. The sample was a deformable body discretized into four noded axisymmetric (CAX4) elements. The sample is constrained from moving in the 1-direction (x-axis) along the axis of symmetry and in the 2-direction (y-axis) along the bottom surface. The highest mesh density in the region where highest stresses or strains were expected was achieved by discretizing the indentation zone. A mesh density of at least 64 elements/µm, along one direction, is used for all simulations in this zone. The indenter was represented by an axisymmetric rigid indenter of radius 10 µm. In the simulation, a downward vertical displacement condition was imposed on the node at the center of the indenter which is tied to the surface of the indenter. Contact between the sample and indenter was defined as a hard surface-to-surface contact with the indenter as the master surface and the sample as the slave surface. To test our model, we indented isotropic, elastic and viscoelastic materials and compared the FE results with the analytical Hertz and viscoelastic solution respectively. The FE result showed good agreement with the analytical solutions, thereby validating the FE model developed in this study for simulating indentation.
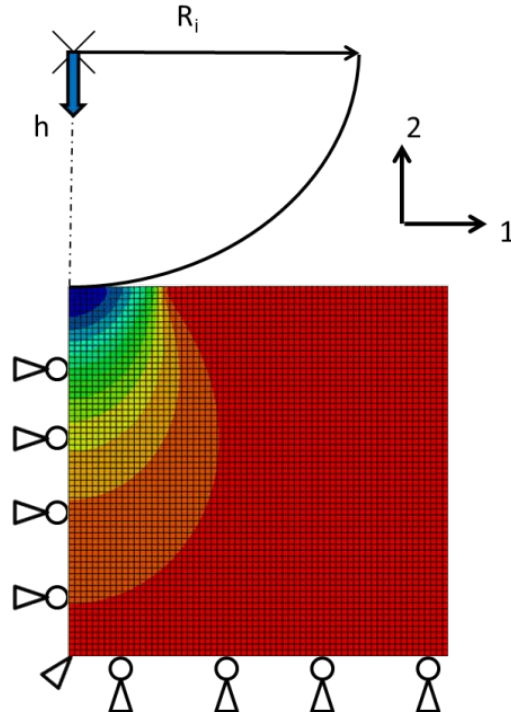
Figure 12 - Schematic of indenter, sample, and boundary conditions used for finite element simulations.

The viscoelastic material properties used for the simulation were obtained from our nanoindentation experiments done on LDPE (presented in the next chapter) in terms of a two term Prony series representation:

$$E(t) = 0.15 + 0.057e^{-0.091t} + 0.043e^{-0.0094t} \quad GPa \tag{85}$$

The elastic material properties used for the simulations were steady state stiffness, 0.2482 GPa, and LDPE's Poisson's ratio, 0.45. The indenter was indented into the material to a depth of 50 nm at 50 nm/s, 5 nm/s, 5×10^{-1} μm/s, and 5×10^{-2} μm/s. As can be seen from Figure 13, the material produces different responses as the displacement rate is reduced. At high displacement rates, the response is almost identical to the elastic case. This is because the time it takes to reach the specified displacement is lower than the material's

time constants thus not giving the material enough time to relax. At a lower displacement rate, the material has enough time to relax thus the response would be lower. The rate dependence will also be shown experimentally in the next chapter by indenting different viscoelastic materials at different rates.
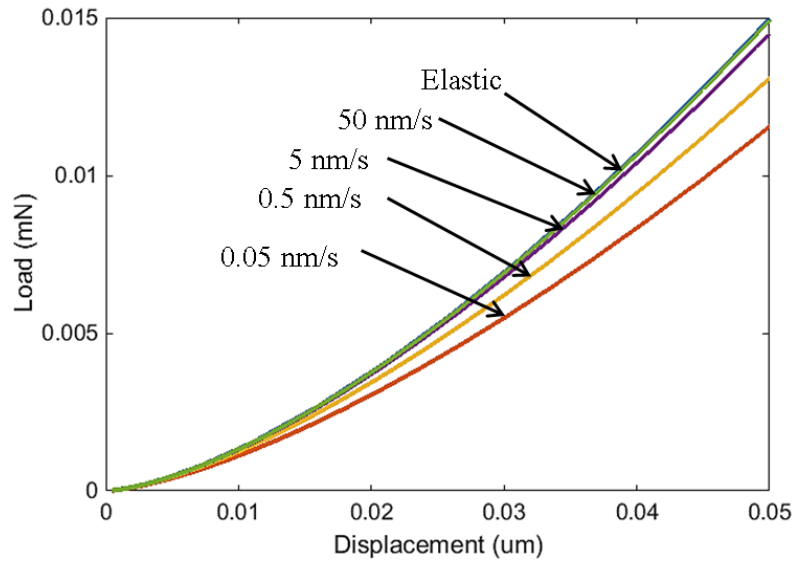
Figure 13 - FE simulation of indentation loading-unloading cycles on LDPE at different displacement rates.

Another method for determining viscoelasticity is to perform a creep or relaxation test. The creep test, in the next chapter, is performed by ramping to a specific load, holding the load for some time, and unloading at the same rate as shown in Figure 14. For a viscoelastic material, displacement will increase as shown in Figure 3. The relaxation test can be performed by ramping to a specific displacement, holding the displacement for some time, and unloading at the same rate as shown in Figure 14. For a viscoelastic material, load will decrease as shown in Figure 2. These tests will give a first glance at how viscoelastic a material is and whether the data collected from nanoindentation should

be treated as viscoelastic. The data from the creep tests will also be used to extract the viscoelastic property of the material as explained in the next section.
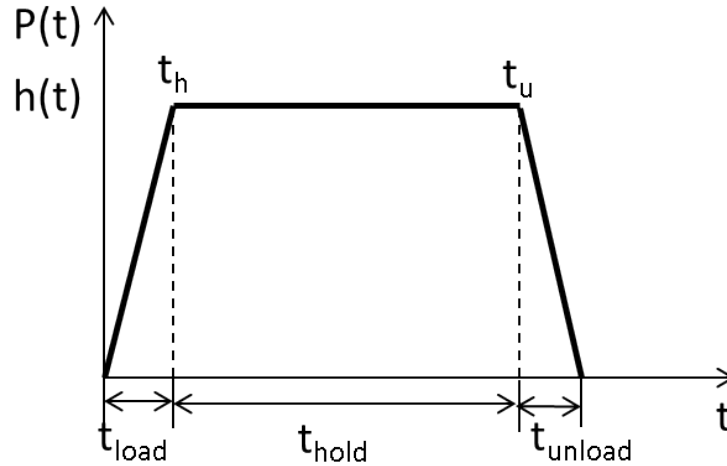
Figure 14 - Schematic for performing a creep or relaxation test.

3.2. Step 2: Extract Viscoelastic Property

This step should be performed before the zero-point correction and the data can be reanalyzed once the correction is performed in the next step. This step is to extract the material's viscoelastic property from the loading portion (in either displacement controlled or load controlled tests) of the curve or from the ramp and hold tests. To extract from the loading portion, the deconvolution procedure described in section 2.3 is used, where the convolution to be solved is given by equation (84) with the terms obtained from equations (78) for a displacement controlled test or (79) for a load controlled test. The unknown in this case is either the relaxation modulus or the creep compliance represented by array X with the terms in matrix A derived from dP/dt or $dh^{3/2}/dt$ for each case respectively. The output in array B is then represented by the load

as P or the displacement as $h^{3/2}$. Since the inputs and outputs are recorded by as discrete signals, noise and other perturbations will affect the solution obtained after approximation. This can be represented by the condition number of matrix A, which measures how much the output will change for a small change in the input. A high condition number means the problem is ill-conditioned and small errors in the output can cause a large error in the solution obtained. Whereas a low condition number means the error in the solution will not be much larger than the errors in output [72]. After numerically testing a few inputs that can be performed experimentally we found that the lowest condition number is obtained when the indentation input is a constant load rate, dP/dt = constant, giving us more consistent solutions for the creep compliance. Using a constant loading rate, a solution for the creep compliance is then obtained. This solution can then be fit to a Prony series to be used to describe the viscoelastic behavior.

If instead a ramp and hold test is performed, the method presented by Oyen [68] is used to analyze the data obtained. The loading conditions can be written as:

$$
\begin{aligned}
P(t) &= kt & 0 \le t \le t_h \\
P_{max} &= kt_h & t_h < t \le t_u
\end{aligned}
\tag{86}
$$

where t_h is the time it takes to reach the maximum load and k is the loading rate. The second term in equation (86) is then a constant. This means that the viscoelastic equation for creep (equation (79)) must be solved twice, once for the ramp and again for the hold:

$$
h^{\frac{3}{2}}(t) = \frac{3(1-\nu)}{8\sqrt{R}} \int_0^t J(t-\tau)\, k d\tau \qquad\qquad 0 \le t \le t_h
$$

$$
h^{\frac{3}{2}}(t) = \frac{3(1-\nu)}{8\sqrt{R}} \left[\int_0^{t_h} J(t-\tau)\, k d\tau + \int_{t_h}^t J(t-\tau)\, 0 d\tau \right]
\tag{87}
$$

$$h^{\frac{3}{2}}(t) = \frac{3(1-v)}{8\sqrt{R}} \int_0^{t_h} J(t-\tau)\,kd\tau \qquad\qquad t_h \le t \le t_u$$

If a Prony series representation of the creep compliance, equation (31), is used and the integrals are solved, we get:

$$h^{3/2}(t) = \frac{3(1-v)k}{8\sqrt{R}} \left[J_\infty t - \sum_{i=1}^N j_i \tau_i \left(1 - e^{-t/\tau_i}\right) \right] \qquad 0 \le t \le t_h$$

$$h^{3/2}(t) = \frac{3(1-v)k}{8\sqrt{R}} \left[J_\infty t_r - \sum_{i=1}^N j_i \tau_i e^{-t/\tau_i} \left(e^{-t_r/\tau_i} - 1\right) \right] \qquad t_h < t \le t_u$$

(88)

The hold portion of the nanoindentation test can then be fit to the second term in equation (88) to extract the constant terms and get the creep compliance function. This method takes into account the ramping it takes to achieve the holding load rather than assuming it is fast enough to be considered a step load. The relaxation modulus can then be extracted by using equation (19) and deconvoluting.

3.3. Step 3: Perform Zero Point Correction

After an indentation has been performed and the data is collected the next step is to make sure that the initial portion of the load-displacement curve is corrected for the CSM oscillations and then the zero-point. The zero-point correction for the elastic nanoindentation case as explained in section 2.2.1 can only be performed because Hertz's model can be arranged in terms of the available signals; load, displacement, and contact stiffness. In the viscoelastic nanoindentation case, due to the convolution integrals in the equations, this cannot be done without extracting the creep compliance or relaxation modulus first, as shown by Cheng and Cheng [73]. Equation (79) can be rearranged to obtain:

$$h(t)\sqrt{R_{eff}h(t)} = \frac{3(1-v)}{8}\int_0^t J(t-\tau)\frac{dP(\tau)}{d\tau}d\tau \tag{89}$$

Equation (74) can then be substituted into (89) and an expression for the displacement correction is obtained:

$$h(t) - h^* = \frac{3(1-v)}{8a(t)}\int_0^t J(t-\tau)\frac{dP(\tau)}{d\tau}d\tau \tag{90}$$

where h^* is the measured displacement at the effective point of contact. The creep compliance can be estimated by performing a creep test and using the method presented in the next section. Once this is obtained, the only unknown is h^* and the contact radius.

In elastic indentation, the contact radius can be obtained by equation (57), a relationship between the contact stiffness, contact radius, and elastic moduli. Since in the experiments the stiffness is obtained from the small unloads performed by the CSM module, the viscoelastic response of these unloads would depend on the frequency applied. These oscillations were simulated using the indentation FE model at different frequencies as shown in Figure 15. The phase angle between the applied displacement oscillations and the resulting load oscillations were measured. At high frequencies the phase angle between the oscillations approaches zero and they can be thought of as being elastic. Therefore the relationship between the elastic modulus, contact area, and stiffness holds at high frequencies, in this case greater than 10 Hz.
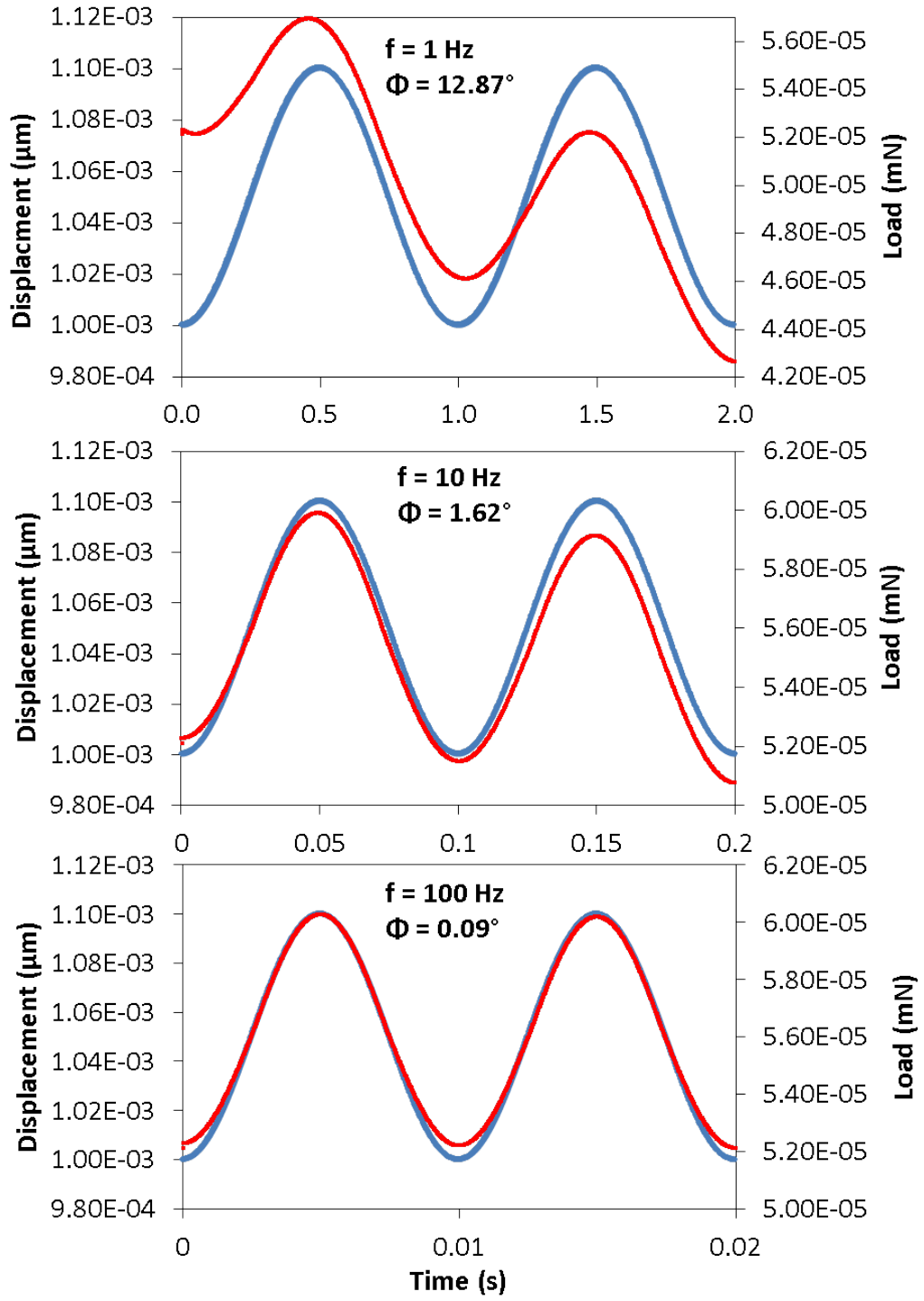
Figure 15 - Finite element simulations of LDPE at different displacement oscillation frequencies.

The CSM oscillations are generally performed at a frequency of 45 Hz and amplitude of 2 nm giving them a loading rate of 0.18 µm/s. This means that the stiffness values from the oscillations can be considered elastic and used to obtain the contact area.

Another question that can be answered using the FE simulations is the relationship between contact radius, displacement, and effective radius given by equation (74). The contact radius of the FE simulations can be measured directly from each simulation by finding out the number of surface elements that are in contact with the indenter at each time step. The results are plotted in Figure 16 for the elastic case and the four viscoelastic displacement rates. For the elastic case and all four displacement rates, the loading curves fall on top of each other. These results show that as the indenter is pushed into the material, the contact radius does not depend on the rate of indentation and is the same as the elastic case. This validates equation (74) for viscoelastic nanoindentation since the contact radius is only dependent on the effective radius and depth of indentation as long as it is increasing.
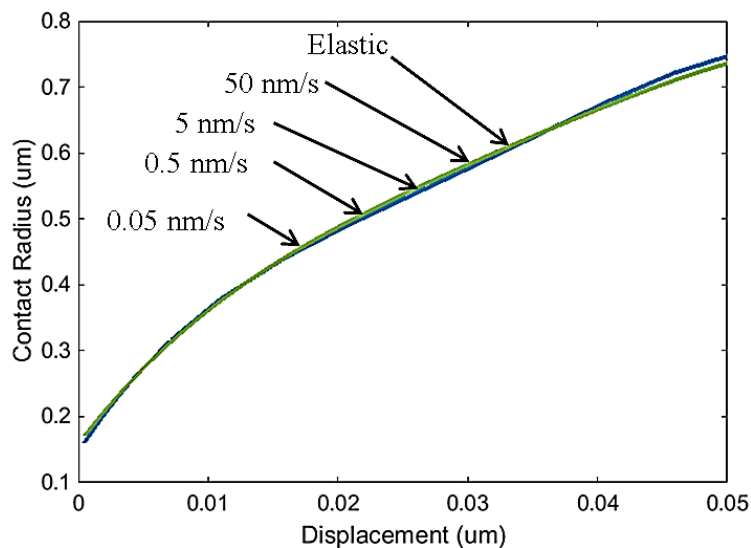
Figure 16 – Contact area vs displacement from FE simulations of LDPE at different displacement rates.

51

3.4. Step 4: Extract Stress-Strain Curves

With the zero-point corrected for and the viscoelastic property extracted, the stress-strain curves can now be recovered from the load-displacement data. The indentation stress can simply be cast as load applied over the indentation contact area:

$$\sigma_{ind}(t) = \frac{P(t)}{\pi a(t)^2} \tag{91}$$

Since strain is merely a function of the geometry of the material being deformed, the indentation strain can be cast as it was in section 2.2.1.3 [17]:

$$\varepsilon_{ind}(t) = \frac{4}{3\pi} \frac{h_t(t)}{a(t)} \approx \frac{h_t(t)}{2.4a(t)} \tag{92}$$

This definition of strain is idealizing the primary zone of indentation as a cylinder of radius a and length 2.4a which is compressed by the total indentation depth h_t. This definition was validated using both numerical simulations and experimental measurements [17, 18, 20, 41]. Since the CSM oscillations are performed at a frequency of 45 Hz and amplitude of 2 nm, they can be considered elastic as explained in section 3.2 and equation (57) can be used to obtain the contact radius a by using the instantaneous modulus as the elastic modulus. With these definitions of stress and strain, the load-displacement curves obtained by nanoindentation can be converted to stress-strain curves.

CHAPTER 4: SPHERICAL NANOINDENTATION ON

COMMODITY POLYMERS

In this chapter we perform uniaxial compression tests and spherical nanoindentation, using the protocol described in the previous chapter, on polymethyl-methacrylate (PMMA), polycarbonate (PC), and low-density polyethylene (LDPE). The goal is to obtain viscoelastic properties and stress-strain curves through nanoindentation that can be compared to the uniaxial compression case.

4.1. Experimental Procedure

4.1.1. Materials

All the polymer specimens used for tests in this chapter were obtained from McMaster-Carr (Elmhurst, IL). For nanoindentation, the specimens were obtained from a 1.25 inch diameter extruded rod for PMMA (density 0.043 lbs/in^3; glass transition temperature 105°C), PC (density 0.045 lbs/in^3; glass transition temperature 145°C), and LDPE (density 0.033 lbs/in^3; glass transition temperature -125°C). For compression tests, the PMMA and PC specimens were extruded rods of approximately 0.625 in diameter and 1.1 in length and the LDPE specimens were extruded rods of approximately 1 in diameter and 2 in length. Each PMMA specimen was annealed at 110°C and each PC specimen was annealed at 150°C. All the specimens were annealed in a Thermo Scientific Lindberg/Blue M^{TM} Moldatherm^{TM} box furnace (Waltham, MA) for two hours and then slowly cooled down to room temperature at a rate of 5°C/hr. The nanoindentation specimens were cut perpendicular to the extruded direction using an

Allied TechCut 5^{TM} (Rancho Dominguez, CA) precision sectioning machine and then polished using silicon carbide paper of decreasing grit size (320, 800, 1200, 2400, and 4000 grit) using a Struers Tegramin-30 (Cleveland, OH). Each polishing step except the 4000 grit was performed for 2 minutes, followed by washing to remove debris. The 4000 grit was performed for 6 minutes. This was followed by polishing with a 1 μm alcohol based diamond suspension (Struers DP-Suspension) for 20 minutes and a 0.05 μm colloidal silica suspension (Buehler MasterMet) for 20 minutes.

4.1.2. Uniaxial Compression Tests

Compression tests were performed on an MTI Phoenix Universal Testing Machine with a 20,000 lb. load cell. Tests were performed according to ASTM standard D695 for testing plastics [74] at a speed of 0.05 in/min. Displacement was measured using a capacitance gage and all load-displacement data was converted to true stress-strain curves. At least five samples were tested for each material with the data reported as mean ± standard error.

4.1.3. Indentation Tests

The indentation tests were performed on an Agilent G200 (Keysight Technologies Inc., Santa Rosa, CA) Nano Indenter with an XP head. The indenter has a maximum load of 500 mN with a high load option of 10 N and a load resolution of 50 nN. The maximum indentation depth achievable is greater than 500 μm with a resolution of less than 0.01 nm. The indents are performed on the polished surfaces of the polymers and the spherical diamond tips used have a radius of 16 μm, 100 μm, and 1500 μm. Since changes in temperature can cause expansion or shrinkage of materials leading to errors in

measurement, the indenter measures a thermal drift before each test by holding the indenter on the surface of the material and measuring any changes in displacement. All tests were performed after the measured indenter drift rate reached and maintained a value of 0.05 nm/s. CSM corrections were applied to the displacement, load, and stiffness of all the tests as explained in section 2.2.1.1.

To find the range where the material is still viscoelastic, each sample was loaded and unloaded at the same rate with three or four different maximum loads. Before completely unloading the material, a pre-set load was left on the material for a period of time. Using the 100 µm radius indenter tip PMMA and PC were loaded at a loading rate of 2.5 mN/s with maximum loads of 40 mN, 80mN, 160 mN, and 320mN for PMMA and 20 mN, 40mN, 80mN, and 160mN for PC. For LDPE a loading rate of 2 mN/s and maximum loads of 8 mN, 16 mN, and 32 mN were used. The loads held at unload were 5 mN for PMMA and PC and 2 mN for LDPE.

To show each material's viscoelasticity and to extract the viscoelastic properties ramp and hold tests were performed using the 100 µm indenter. For each material the load was increased to three different loads at a constant loading rate and that load was held for 300 seconds and then unloaded at a constant unloading rate. For PMMA, the loading rate was 4 mN/s and the holding loads were 20 mN, 40 mN, and 60 mN. For PC, the loading rate was 4 mN/s and the holding loads were 8 mN, 20 mN, and 40 mN. For LDPE, the loading rate was 2 mN/s and the holding loads were 4 mN, 8 mN, and 16 mN. The viscoelastic properties were extracted from the hold portion. The stress-strain curves were extracted from the indentations done at loading rates of 0.05 s^{-1} and 0.5 s^{-1} up to a

specified displacement. The rate in this case is defined by the nanoindenter as the loading rate, dP/dt, divided by the measured load, P.

4.2. Finite Element Study

To better understand the experimental results obtained, uniaxial compression and spherical nanoindentation finite element studies were performed using the viscoelastic material properties obtained by the creep tests. The same model and displacement rates described in section 3.1 were used for the spherical nanoindentation case. Uniaxial compression was performed on a cylinder with a radius of 20 μm and length of 20 μm using the viscoelastic material properties obtained by the creep tests. The viscoelastic nanoindentation load-displacement curves were converted to indentation stress-strain curves using equations (91), (92), and (74). The uniaxial compression load-displacement curves were converted to true stress-strain curves.

4.3. Results and Discussion

4.3.1. Uniaxial Compression Tests

The results from the compression tests are shown in Figure 17. The measured strain rates were 8×10^{-4} s^{-1} for PMMA and PC and 5×10^{-4} s^{-1} for LDPE. It was observed that the PMMA and PC samples failed by shearing with polycarbonate shearing more than PMMA which may have caused some of the drop in stress with increasing strain. This drop in stress has been extensively reported in literature and is usually attributed to a combined effect of strain softening and thermal softening [75]. Care was taken to ensure that the sample geometry was always a right cylinder and the axis of loading was aligned, as any misalignment would increase the shear on the material. The moduli, measured

from the initial linear portion of the true stress-strain curves, were 1.9 ± 0.031 GPa, 1.42 ± 0.031 GPa, and 0.154 ± 0.0014 GPa for PMMA, PC, and LDPE respectively. While the compressive modulus values for PMMA and LDPE are acceptable compared to reported values, the value for PC is at least 0.5 GPa lower than expected. This disparity may primarily be due to the thermo-mechanical history that the material experienced before uniaxial compression testing. These results will be compared to the indentation stress-strain curves collected at similar strains and strain rates.

4.3.2. Finite Element Tests

The results from the viscoelastic uniaxial compression and spherical nanoindentation are shown in Figure 18 for tests done on LDPE. These results show the clear strain rate dependence expected of viscoelastic materials. The indentation stress-strain curves consistently show a higher stress value for similar strains. The average ratios between the indentation stress and compression stress are compared in Table 1. These results show an increasing ratio with slower rates. For PMMA and PC, these ratios are relatively constant and are approximately 1.25 and 2.26 for PMMA and PC respectively. These results will be discussed in more detail when compared against the experimental results in the next section.
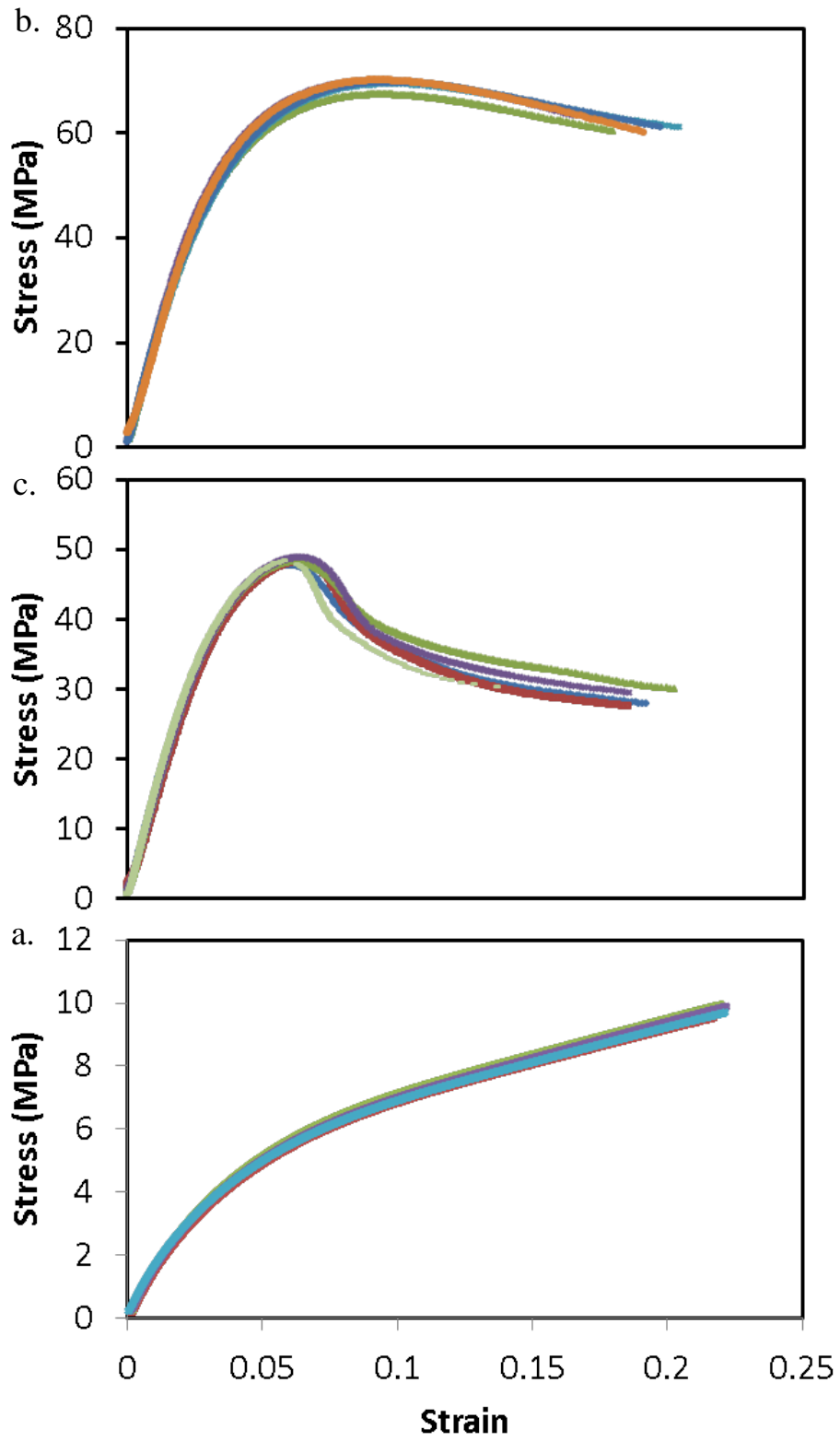
Figure 17 - True stress-strain curves from compression tests on a) PMMA, b) PC, and c) LDPE.
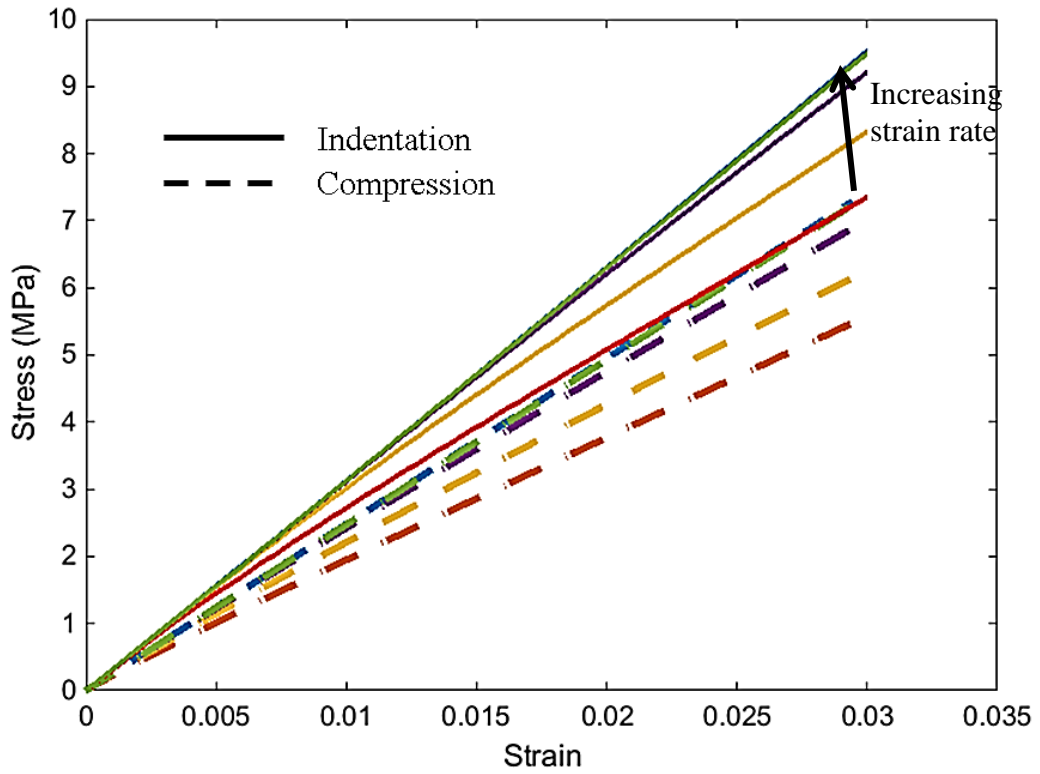
Figure 18 - Finite element stress-strain curves for uniaxial compression and spherical nanoindentation on LDPE.

Table 1 - Average ratio of indentation stress to compression stress for the FE results from LDPE.

LDPE	Strain Rate [/s]	Indentation/ Compression
————	Elastic	1.2689
————	$2x10^{-2}$	1.2716
————	$2x10^{-3}$	1.2938
————	$2x10^{-4}$	1.3452
————	$2x10^{-5}$	1.3715

4.3.3. Spherical Nanoindentation

4.3.3.1. Viscoelastic Region

The results from the tests to find the region of viscoelasticity for PMMA using the 100µm radius indenter tip are shown in Figure 19. Figure 19 shows all curves for the four different maximum loads with at least five tests for each. The results for PC and LDPE are plotted in Figure 20 and Figure 21 respectively. From these results (Table 2) it is seen that above a certain load there is an observable difference in residual displacements and it is assumed that the material may have experienced some plastic deformation above those loads. These results can be used to make a reasonable estimate of the load at which the curves can still be considered viscoelastic. This value is about 160 mN for PMMA, 80 mN for PC, and 16 mN for LDPE. The same tests were performed using the 16 µm and the 1500 µm radius indenter using different loads. For PMMA, this value was 40 mN and 500 mN for the 16 µm and 1500 µm indenter respectively. For PC, this value was 30 mN and 350 mN for the 16 µm and 1500 µm indenter respectively. For LDPE, this value was 3 mN and 50 mN for the 16 µm and 1500 µm indenter respectively.

Table 2 - Residual displacements after holding at 5 mN for PMMA and PC and 2 mN for LDPE.

Material	Maximum Load (mN)	Residual Displacement (nm)
PMMA (5mN)	40	305 ± 3
	80	300 ± 4
	160	322 ± 5
	320	500 ± 2
PC (5mN)	20	307 ± 1
	40	305 ± 1
	80	311 ± 1
	160	334 ± 4
LDPE (2mN)	8	950 ± 2
	16	1033 ± 3
	32	1248 ± 3
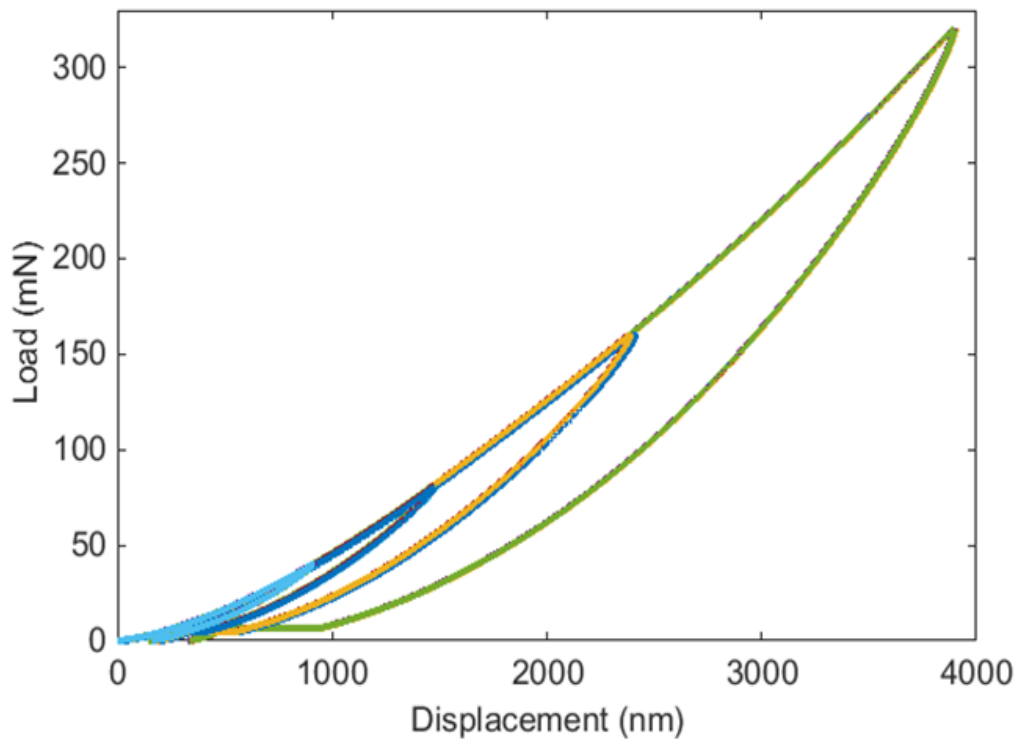
Figure 19 – Indentations to different loads on PMMA.
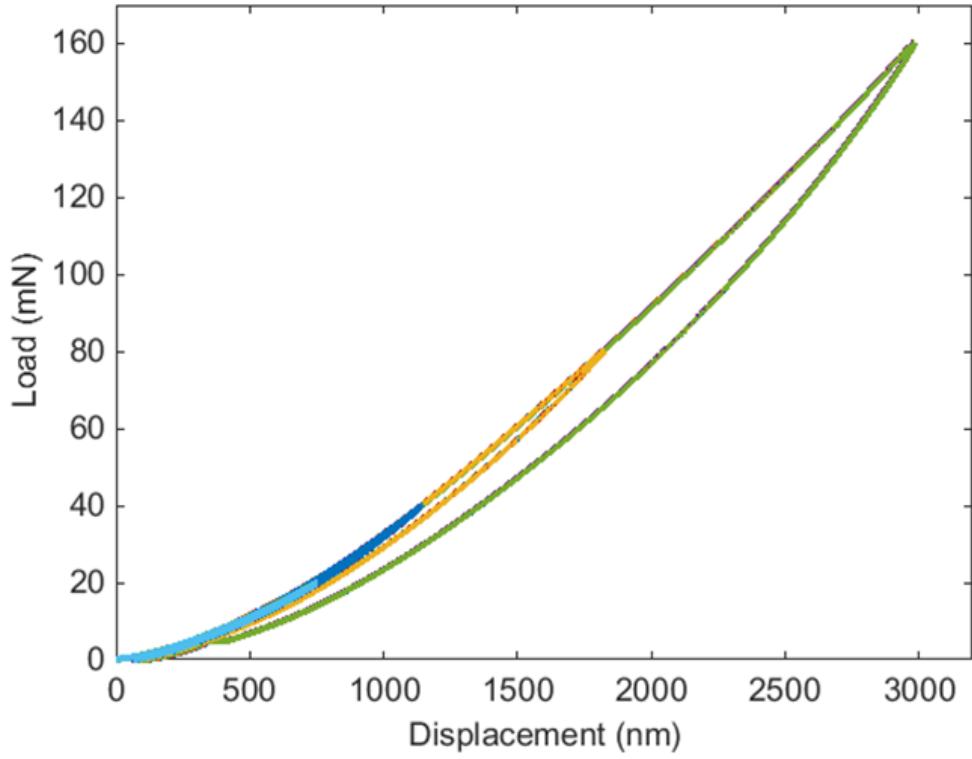
Figure 20 - Indentations to different loads on PC.
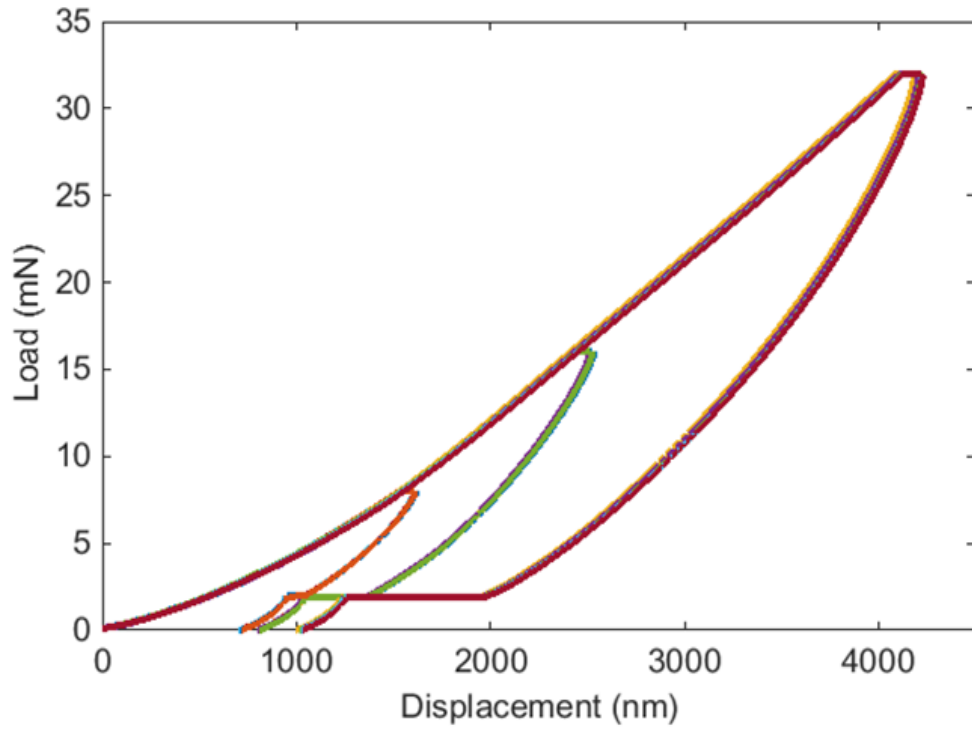
Figure 21 - Indentations to different loads on LDPE.

4.3.3.2. Material Viscoelasticity

     The results from the indentations at two different rates (0.05 s^{-1} and 0.5 s^{-1}) using the 16 µm radius indenter are shown in Figure 22, Figure 23 and Figure 24. These results show a clear difference between the load-displacement curves at the two rates, giving a clear depiction of how viscoelastic each material is. It also clear that LDPE has the largest viscous component and can be considered the most viscoelastic of the three materials while PC is the least viscoelastic. These results show the viscoelastic behavior of the materials and confirm that viscoelasticity should not be ignored when analyzing nanoindentation data on these materials. These results will also be used to extract the indentation stress-strain curves.
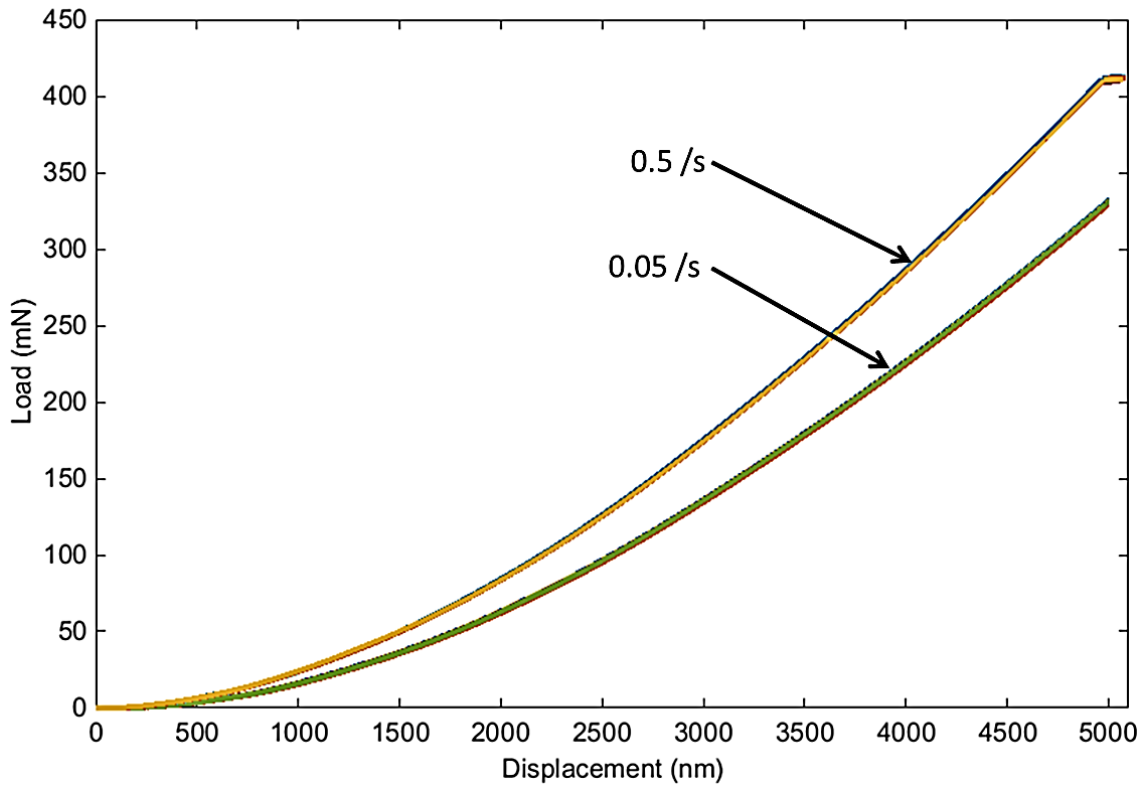
Figure 22 - Load-displacement curves of PMMA at two different loading rates.
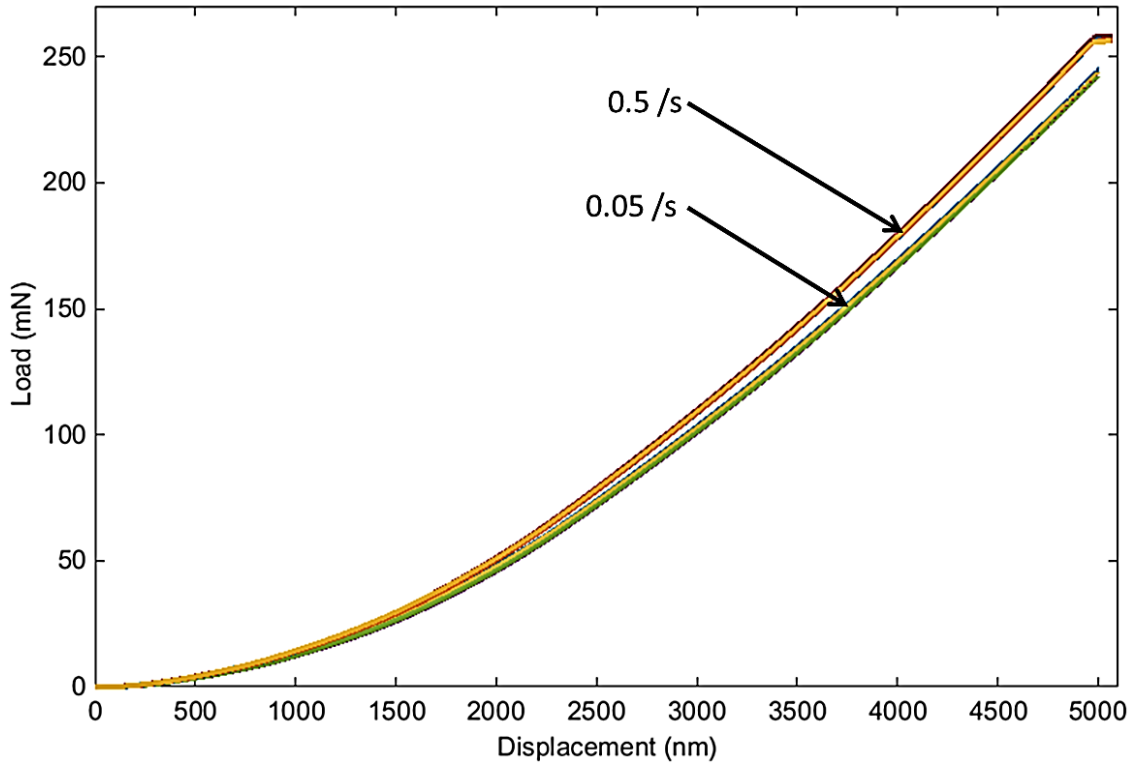
Figure 23 - Load displacement curves of PC at two different loading rates.
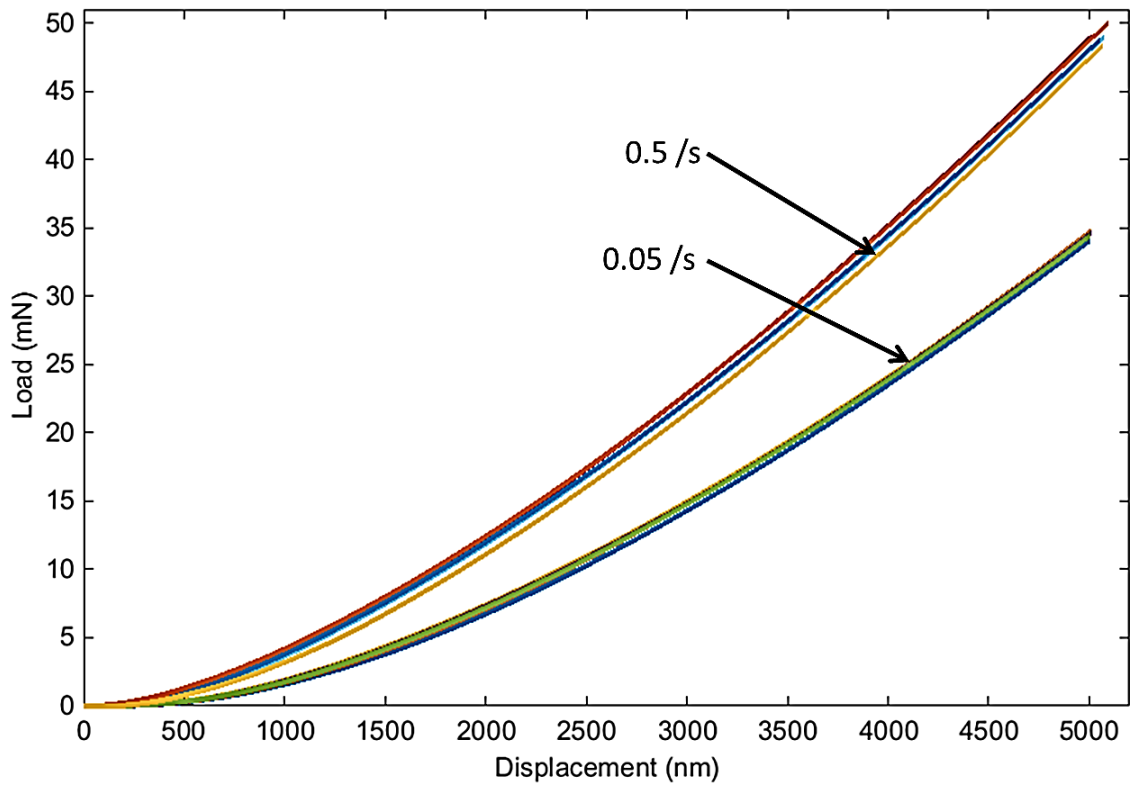
Figure 24 - Load-displacement curves of LDPE at two different loading rates.

The results from the creep tests using the 100 µm radius indenter are plotted in Figure 25, Figure 26, and Figure 27. These results verify how viscoelastic each material is, as was seen in the load-displacement curves at different rates. LDPE is again the most viscoelastic with the largest increase in displacement, while PC has the least, making it close to an elastic material. These results will be used in the next section to extract the viscoelastic properties. From these results it is again clear that viscoelasticity should not be ignored in nanoindentation analysis of PMMA or LDPE. While it may be ignored for polycarbonate, a more accurate quantification of its mechanical properties can only be achieved if viscoelasticity is considered in all nanoindentation analyses. The same tests were also performed using the 16 µm and 1500 µm radius indenter at different loads.
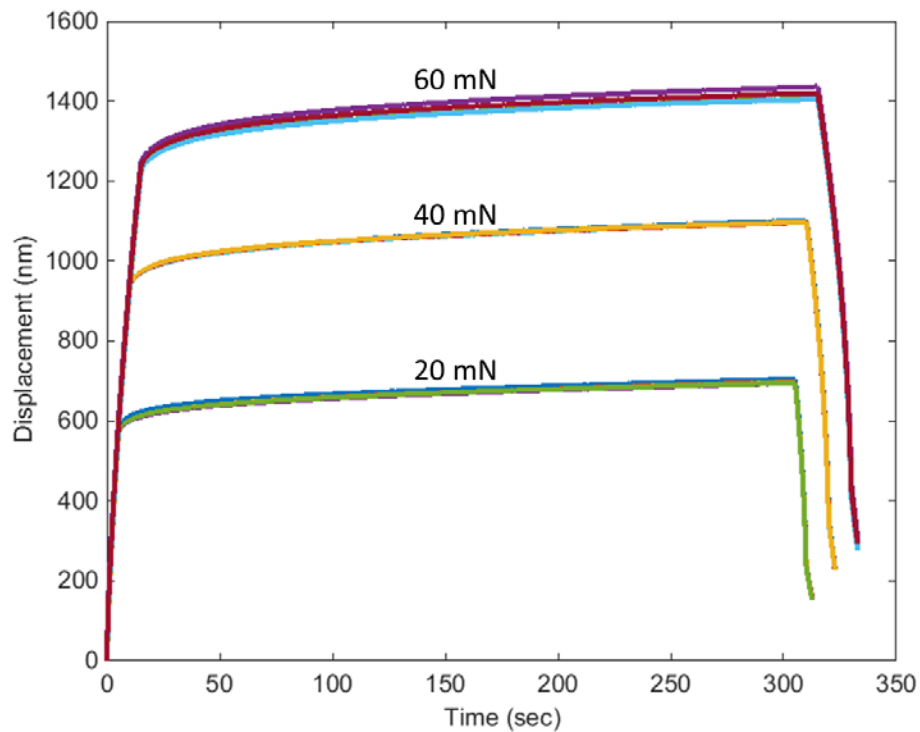
Figure 25 - Displacement vs time for creep tests performed on PMMA at holding loads of 20 mN, 40 mN, and 60 mN.
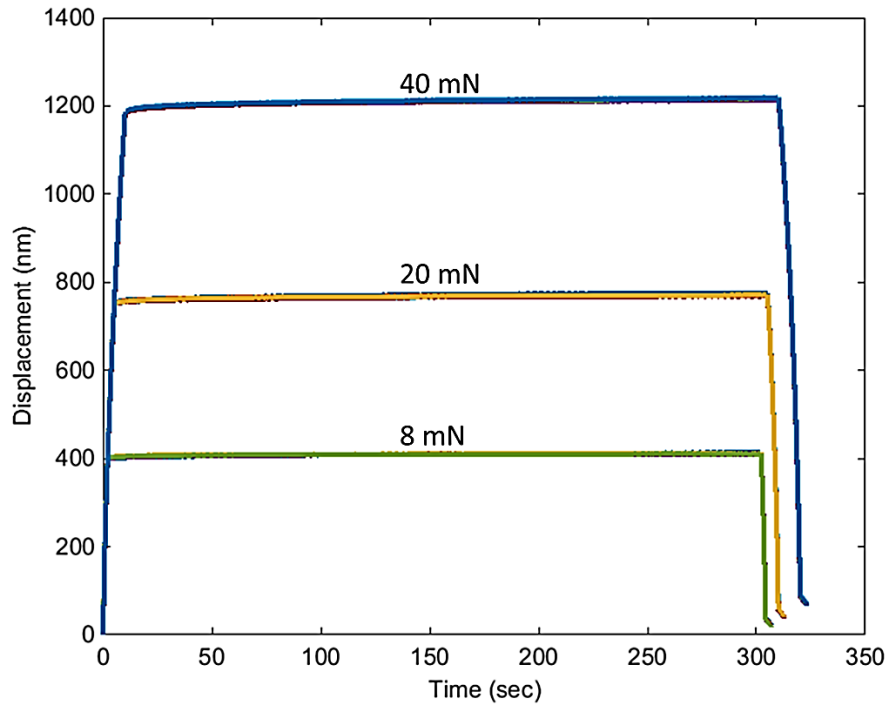
Figure 26 - Displacement vs time for creep tests performed on PC at holding loads of 8 mN, 20 mN, and 40 mN.
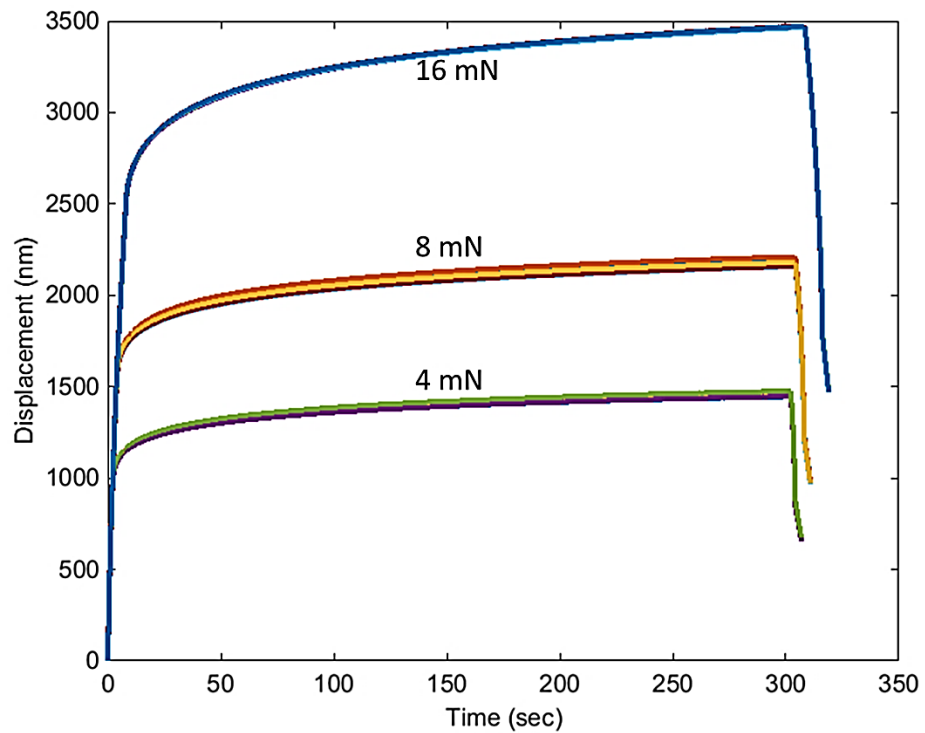
Figure 27 - Displacement vs time for creep tests performed on LDPE at holding loads of 4 mN, 8 mN, and 16 mN.

<u>4.3.3.3. Viscoelastic Properties</u>

The creep compliance and corresponding relaxation modulus were extracted using the methods explained in sections 3.2 and 2.1.4. The viscoelastic properties can be represented in terms of a two-term Prony series such as:

$$J(t) = J_\infty - J_1 e^{-\frac{t}{\tau_{j1}}} - J e^{-\frac{t}{\tau_{j2}}}$$

$$E(t) = E_\infty + E_1 e^{-\frac{t}{\tau_{k1}}} + E_2 e^{-\frac{t}{\tau_{k2}}}$$

(93)

Where the terms in front of the exponentials are the Prony series terms, J_∞ is the long term creep compliance, E_∞ is the long term relaxation modulus, and τ is the time constant. The instantaneous creep compliance, J_0, can be obtained by subtracting the Prony series terms from the long term creep compliance and the instantaneous relaxation modulus, E_0, can be obtained by adding the Prony series terms to the long-term relaxation modulus. These results are tabulated in

Table 3 through Table 5 and the results for the 100 µm radius indenter are plotted in Figure 28 through Figure 32. The compressive moduli obtained by uniaxial compression can be compared to the instantaneous moduli obtained by nanoindentation. These comparisons are plotted in Figure 29 for PMMA and PC and Figure 32 for LDPE. These results show that the compressive moduli are lower than the indentation moduli for all three materials. This is expected as the zone of indentation is constrained by the material surrounding it. This effect usually leads to an increase in modulus and yield strength [76]. Also a much smaller volume of material is being probed leading more local properties compared to the average properties obtained by uniaxial compression. The average ratio between the compressive moduli and indentation instantaneous moduli is 1.6 for PMMA

and LDPE and 1.5 for PC. This ratio can be used to approximate the expected indentation instantaneous modulus for new viscoelastic materials if the compressive modulus is known. The relaxation moduli obtained by Huang and Lu [65] were $E(t) = 2.3343 + 0.1607e^{-0.1t} + 0.2574e^{-0.01t}$ for PMMA and $E(t) = 1.4531 + 0.0681e^{-0.1t} + 0.1359e^{-0.01t}$ for PC. The results for PMMA are comparable to our results with the results for PC being lower than ours.

Table 3 - Viscoelastic Properties for PMMA

Indenter Size	Creep Compliance (1/Gpa)	Relaxation Modulus (GPa)
16 µm	$0.43 - 0.032e^{-t/18} - 0.060e^{-t/216}$	$2.32 + 0.26e^{-t/16} + 0.37e^{-t/186}$
100 µm	$0.45 - 0.044e^{-t/15} - 0.076e^{-t/225}$	$2.23 + 0.37e^{-t/13} + 0.44e^{-t/187}$
1500 µm	$0.41 - 0.025e^{-t/25} - 0.034e^{-t/220}$	$2.46 + 0.20e^{-t/23} + 0.22e^{-t/202}$

Table 4 - Viscoelastic properties for PC

Indenter Size	Creep Compliance (1/Gpa)	Relaxation Modulus (GPa)
16 µm	$0.47 - 0.012e^{-t/15} - 0.010e^{-t/136}$	$2.11 + 0.059e^{-t/15} + 0.047e^{-t/133}$
100 µm	$0.49 - 0.013e^{-t/9} - 0.014e^{-t/151}$	$2.03 + 0.059e^{-t/9} + 0.058e^{-t/146}$
1500 µm	$0.52 - 0.021e^{-t/11} - 0.016e^{-t/162}$	$1.92 + 0.084e^{-t/11} + 0.061e^{-t/157}$

Table 5 - Viscoelastic properties for LDPE

Indenter Size	Creep Compliance (1/Gpa)	Relaxation Modulus (GPa)
16 µm	$6.48-1.22e^{-t/17}-1.58e^{-t/154}$	$0.15+0.072e^{-t/13}+0.046e^{-t/118}$
100 µm	$6.76-1.12e^{-t/14}-1.61e^{-t/138}$	$0.15+0.057e^{-t/11}+0.043e^{-t/106}$
1500 µm	$6.54-1.18e^{-t/15}-1.73e^{-t/146}$	$0.15+0.072e^{-t/11}+0.051e^{-t/108}$
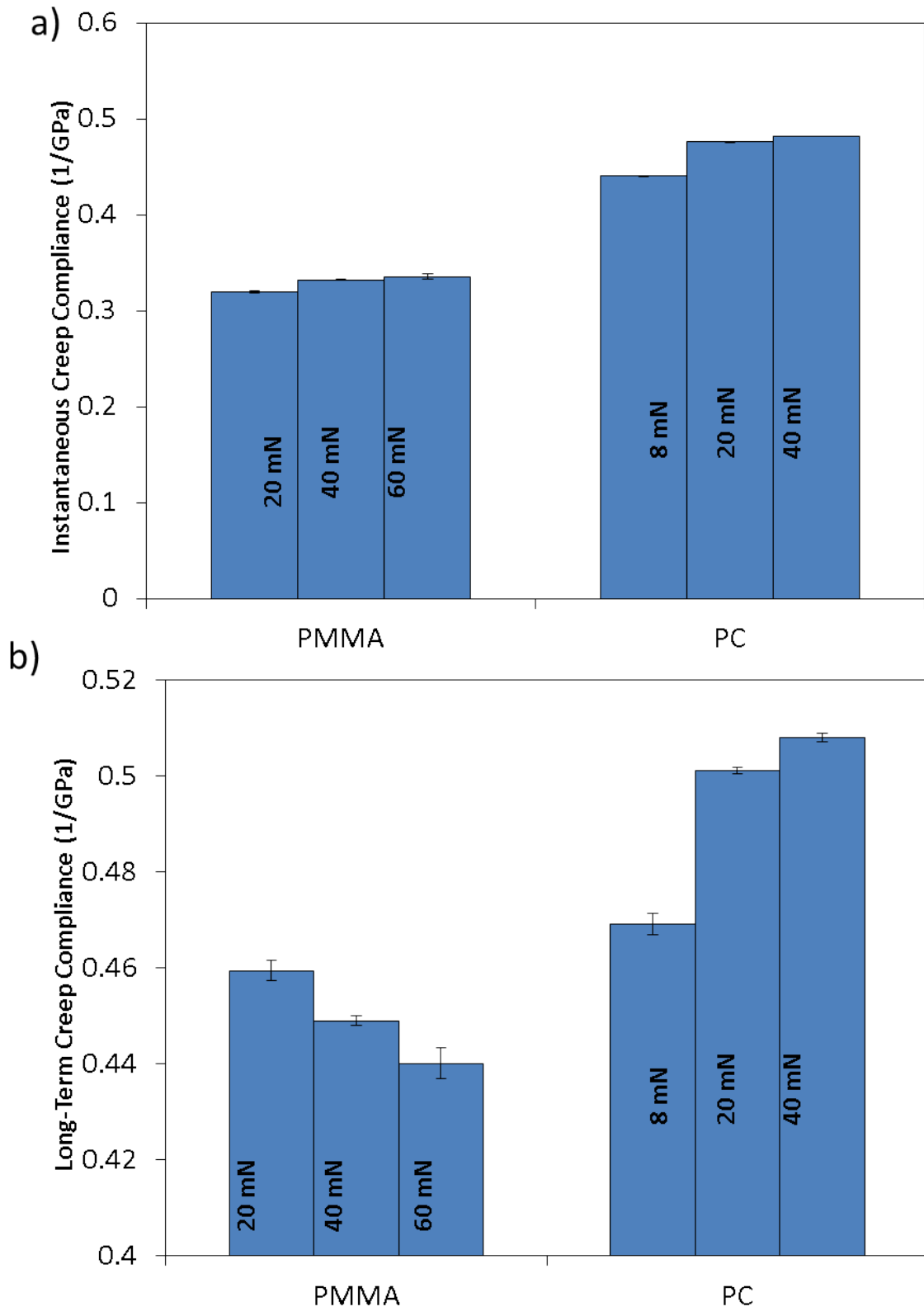
Figure 28 – a) Instantaneous and b) long-term creep compliance for PMMA and PC at the three holding rates.
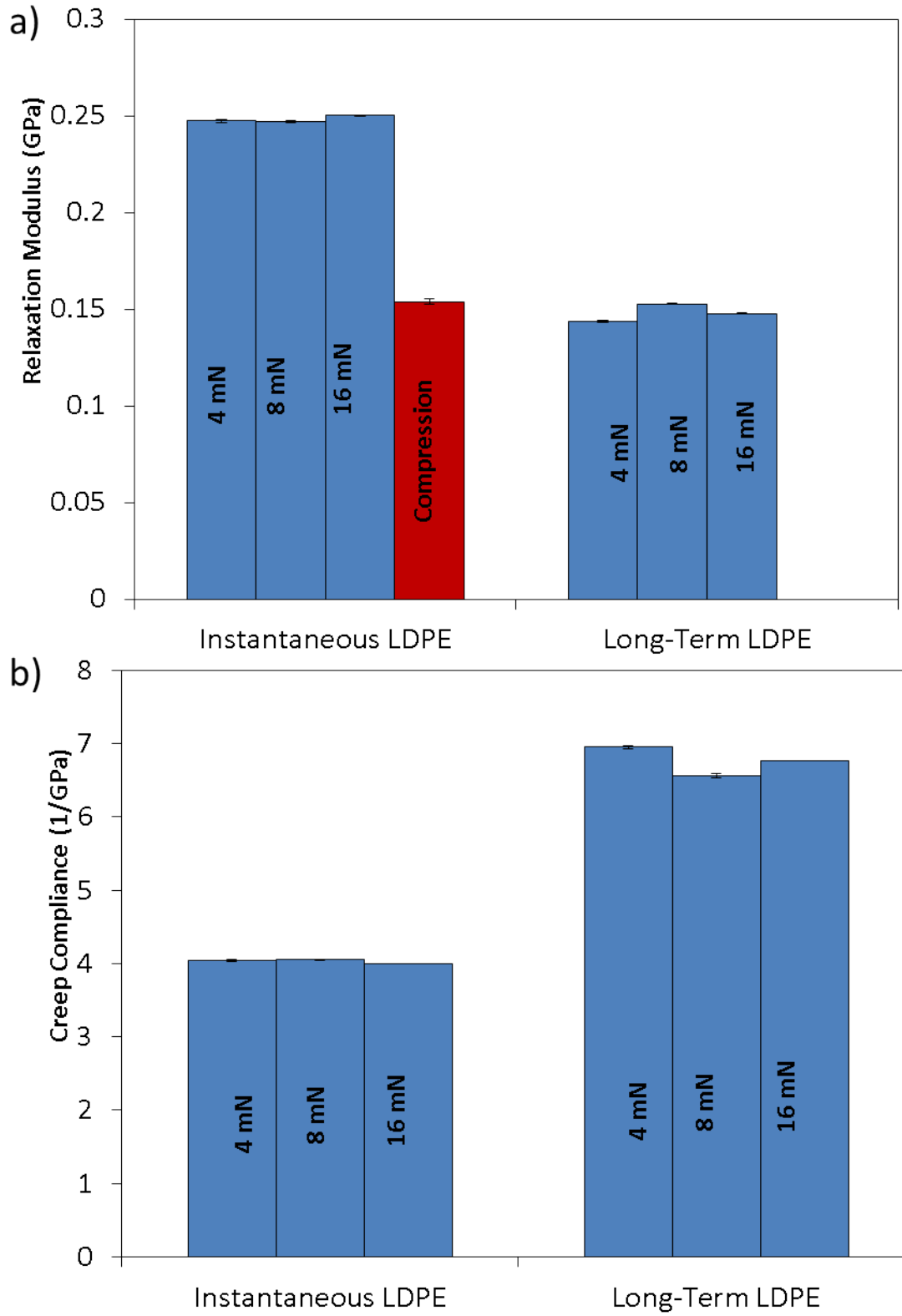
Figure 29 – a) Instantaneous and b) long-term relaxation modulus for PMMA and PC at
the three holding loads. Compression modulus for PMMA and PC is included in a).
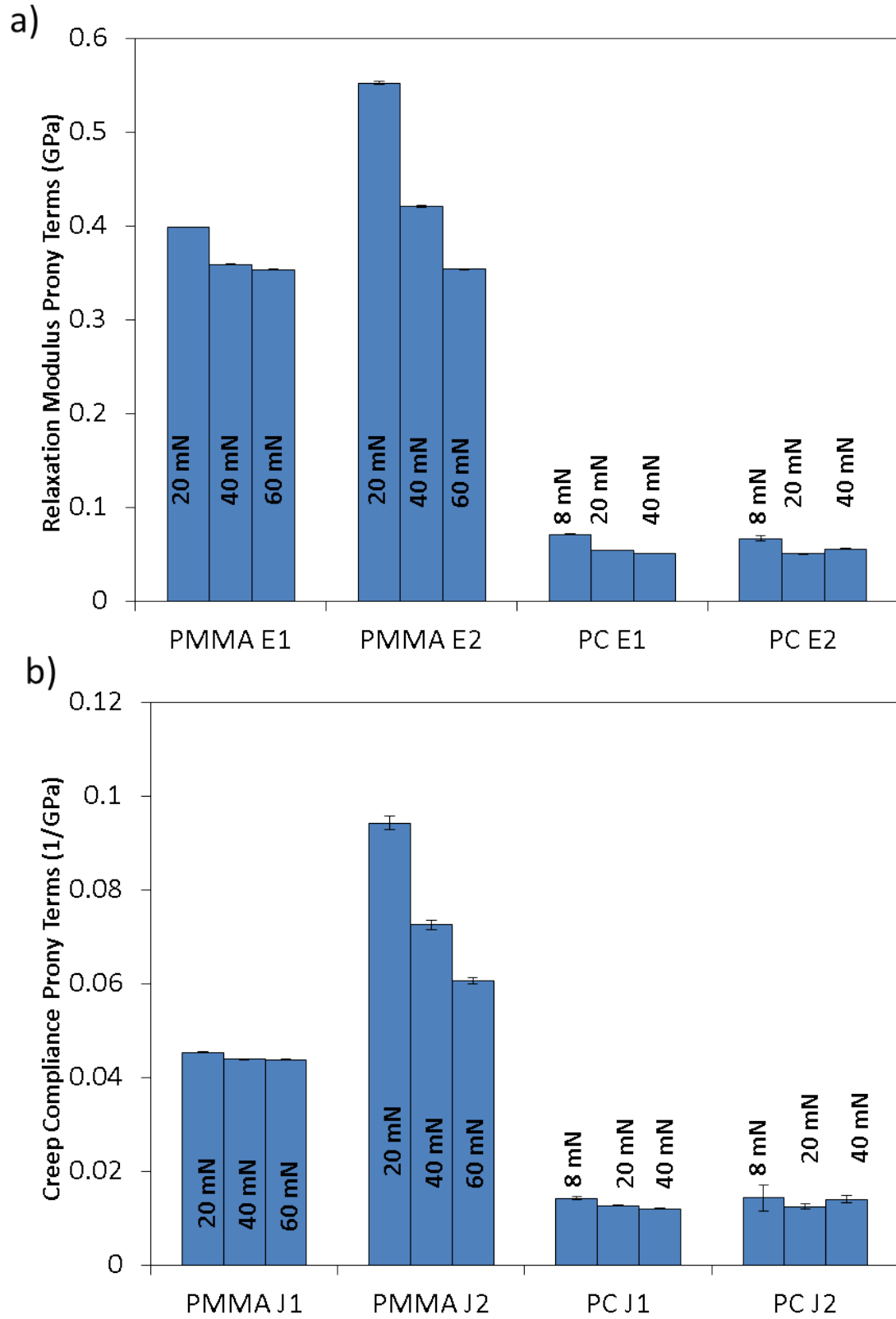
Figure 30 - Prony series terms for a) creep compliance and b) relaxation modulus.
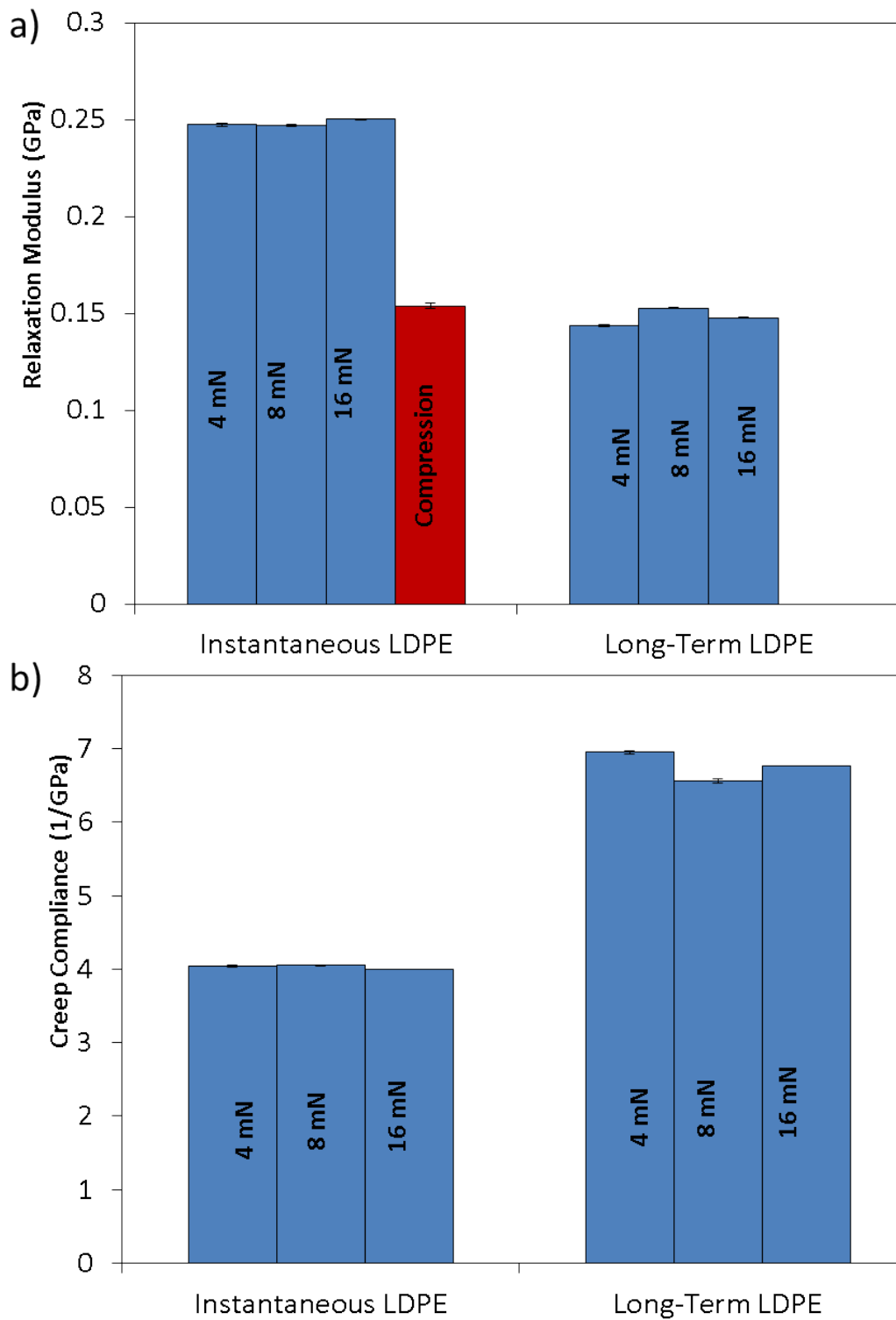
Figure 31 - a) Instantaneous and long-term creep compliance and b) instantaneous and long-term relaxation modulus for LDPE at the three holding loads. Compression modulus for LDPE is included in a).

73
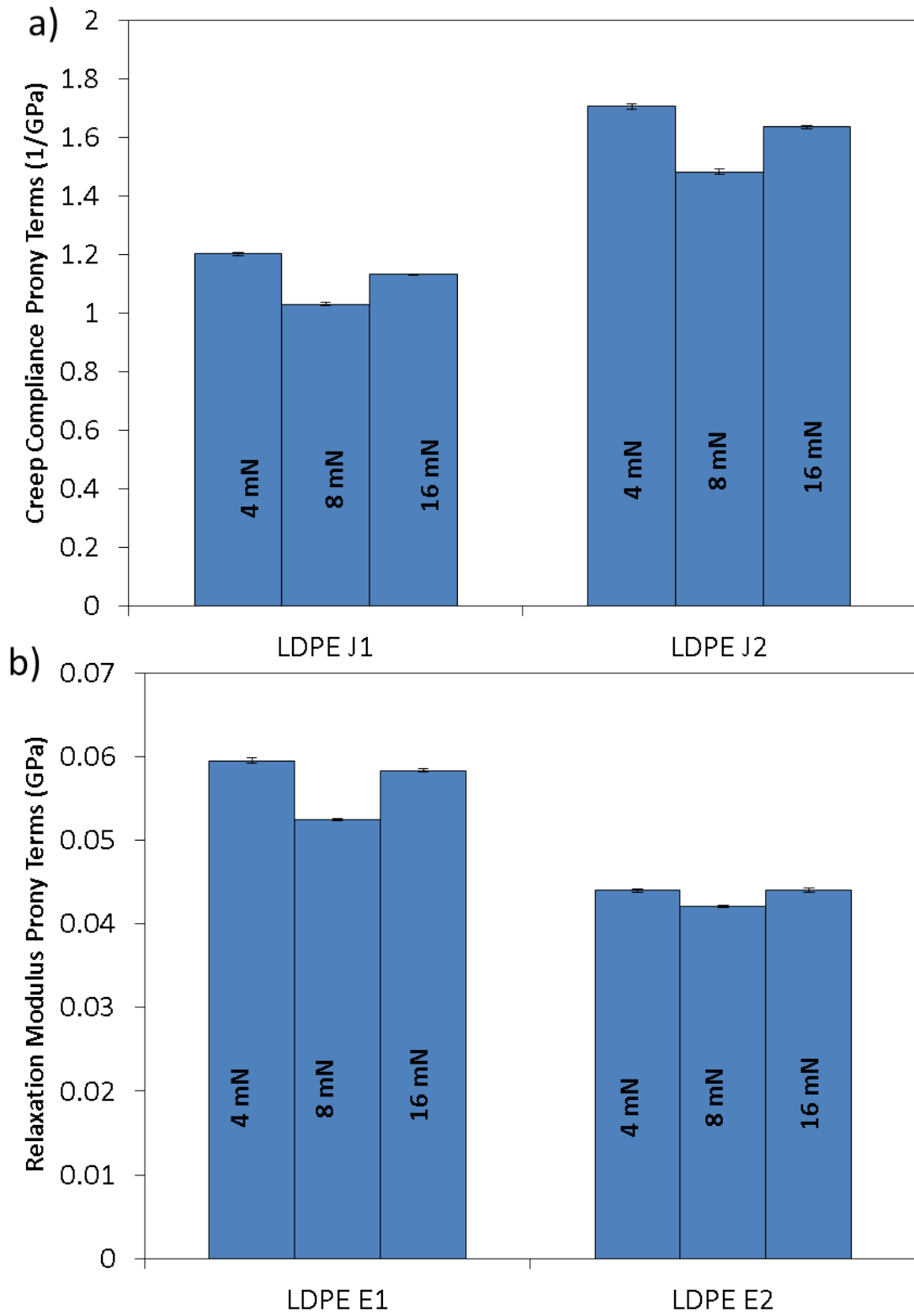
Figure 32 – Prony series terms for a) creep compliance and b) relaxation modulus.

<u>4.3.3.4. Stress-Strain Curves</u>

Once these properties have been extracted, the stress-strain curves can then be produced. First the zero-point is corrected for using the method explained section 3.3. An example of the plot used for the correction on PMMA with a 100 µm radius indenter is shown in Figure 33. The zero-point correction for displacement can then be extracted from the selected portion of the curve using equation (90). The zero-point correction for the load is then simply the load at the corrected displacement. The approximate corrected displacements and loads for the 100 µm radius indenter are 270 nm and 1.4 mN for PMMA, 175 nm and 0.4 mN for PC, and 450 nm and 0.7 mN for LDPE. For the 16 µm indenter they are 50 nm and 0.5 mN for PMMA, 30 nm 0.1 mN for PC, and 150 nm and 0.3 mN for LDPE. For the 1500 µm indenter they are 900 nm and 14 mN for PMMA, 550 nm and 5 mN for PC, and 1300 nm and 8 mN for LDPE. These values depend on the location of the indent, surface roughness, or other surface artifacts that may remain after polishing.
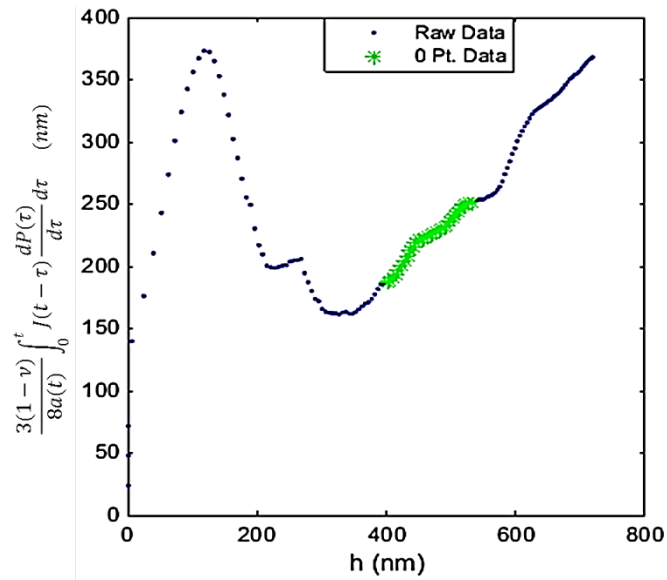
Figure 33 - Example of plot used to perform zero-point correction on PMMA indentation tests.

With the corrections done, the load-displacement curves are converted to stress-strain curves using the method described in section 3.4. The results for PMMA, PC, and LDPE with the 16 µm indenter are plotted in Figure 34, Figure 35, and Figure 36 respectively. They are also compared against results from the compression tests and one set of the indentation stress-strain curves extracted from tests with the 100 µm indenter. For the 1500 µm indenter, due to the load limit on the nanoindenter machine, the achievable strain is very low, less than 0.02, and within the initial viscoelastic portion of the curves. While they confirm that the curves for different indenter tip sizes match at similar strain rates, they do not provide any new information not already shown in the plots. In all three cases, the strain rates for the 100 µm radius, slower 16 µm radius, and compression stress-strain curves are similar and can be compared to each other. It is clear in all cases that the indentation stress-strain curves obtained for different tip sizes are similar, meaning the load-displacement curves are normalized and these protocols can be used for multiple indenter tip sizes.
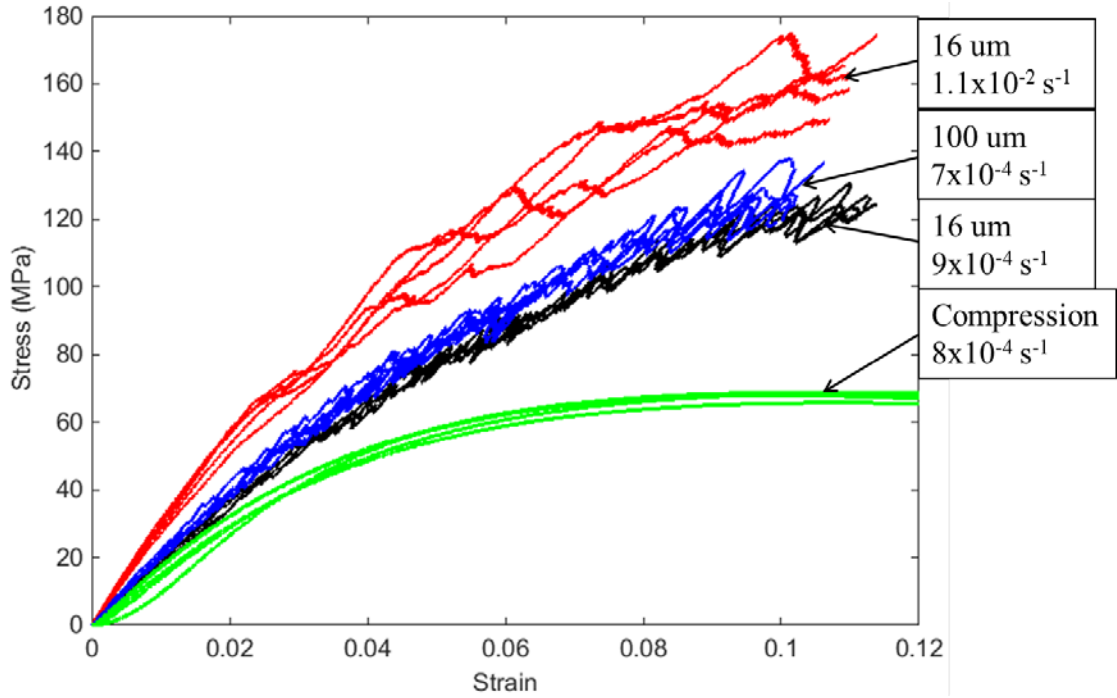
Figure 34 – Stress-strain comparison of nanoindentation tests at two loading rates with uniaxial compression tests done on PMMA.
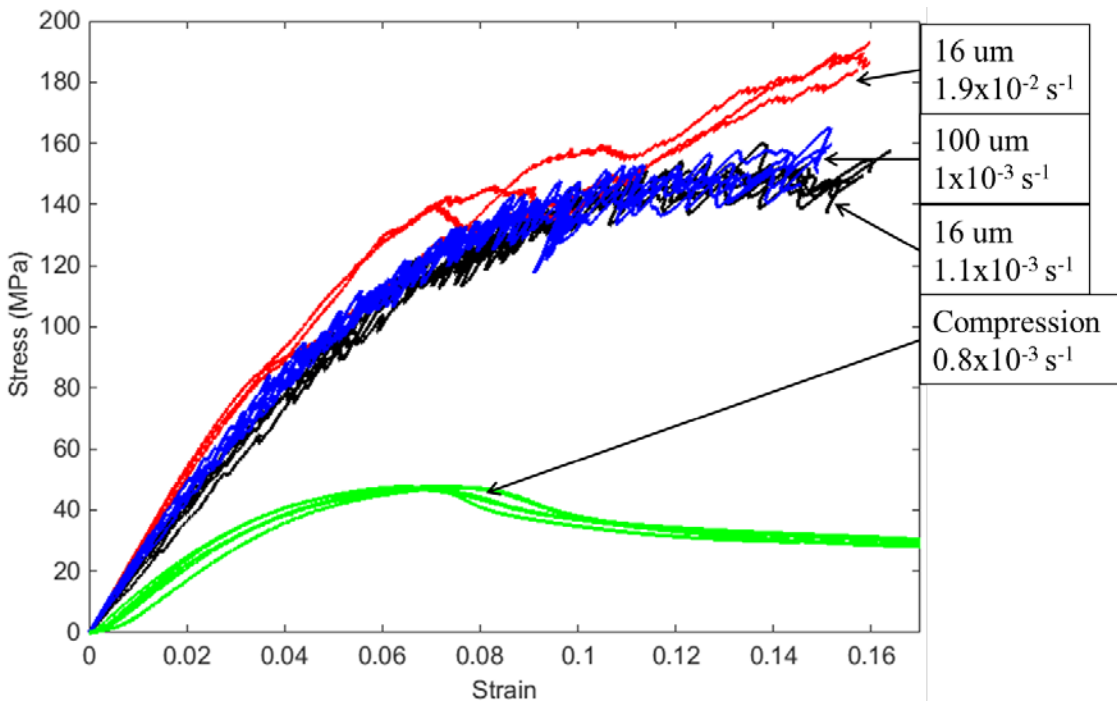
Figure 35 - Stress-strain comparison of nanoindentation tests at two loading rates with uniaxial compression tests done on PC.
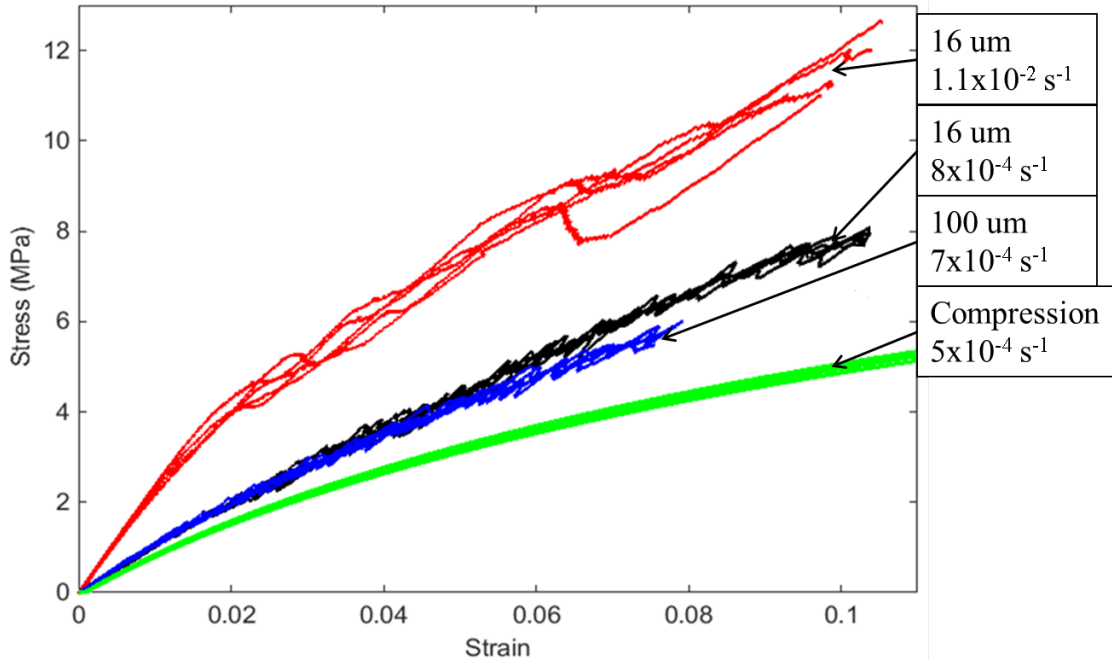
Figure 36 - Stress-strain comparison of nanoindentation tests at two loading rates with uniaxial compression tests done on LDPE.

4.3.3.4.1 Comparison of Indentation Stress-Strain Curves at Different Strain Rates

As the strain increases the indentation stress for the higher strain is greater for all three cases. This difference is clear for PMMA and LDPE with LDPE showing the largest variance between the two. The difference between the two strain rates for PC is not significant. This again confirms the previous tests showing that LDPE is the most viscoelastic, while PC does not show significant viscoelasticity. The average ratio between the higher strain rate and the lower strain rate is 1.57 for PMMA, 1.18 for PC, and 1.77 for LDPE. The ratios obtained by the FE simulations for similar strain rates were 1.23 for PMMA, 1.04 for PC, and 1.23 for LDPE. While there is variance some variance between the idealized FE model and the experimental results, the same trend persists, showing PC as the least viscoelastic of the three materials.

Another measurement that can be obtained from these calculations is the strain rate sensitivity of each material. This is given by:

$$m = \frac{\Delta \ln(\sigma)}{\Delta \ln(\dot{\varepsilon})} \qquad (94)$$

where m is the strain rate sensitivity index, σ is the stress at a specified strain, and $\dot{\varepsilon}$ is the strain rate at the same strain. Since the tests are performed at a relatively constant strain rate, the strain rate sensitivity index can be compared at different strains for each material. These results are shown in **Figure 37** through **Figure 39**. Strain rate sensitivity indexes have been reported ranging from 0.04 [77] to 0.08 [78] for PMMA, from 0.02 [79] to 0.046 [77] for PC, but there are no clear studies for LDPE. The peaks shown for m for PMMA and PC are also approximately where the linear portion of the stress-strain curves and viscoplasticity starts. These results show a clear strain rate sensitivity with LDPE being the most rate sensitive while PC shows the lowest sensitivity. These results again confirm the results presented earlier and show that the strain rate sensitivity of viscoelastic materials can be measured using nanoindentation.
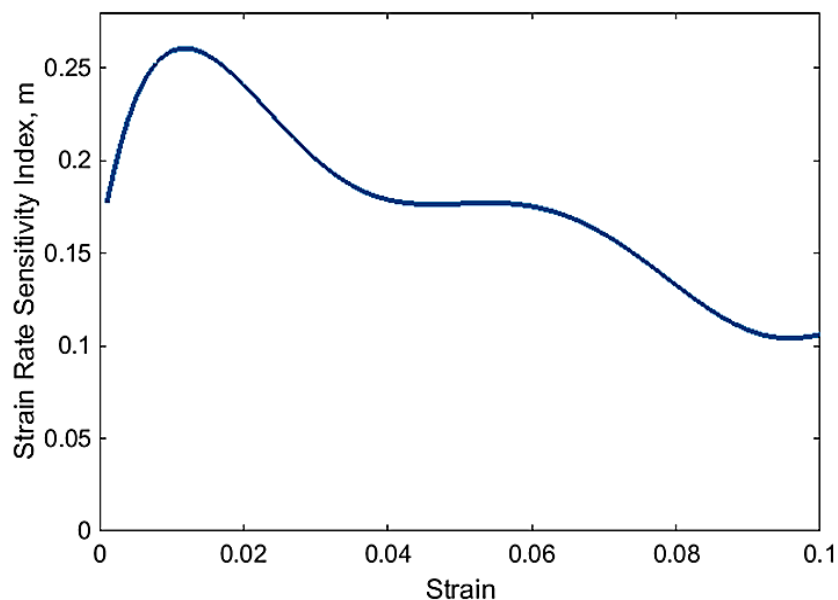
Figure 37 - Strain rate sensitivity index versus strain for PMMA.
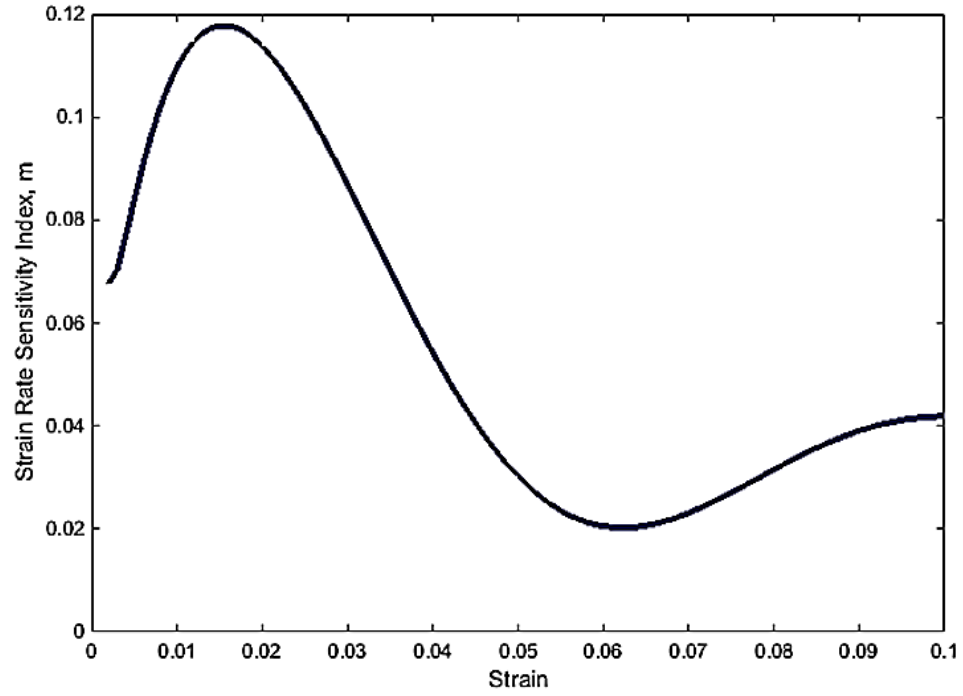
Figure 38 - Strain rate sensitivity index versus strain for PC.
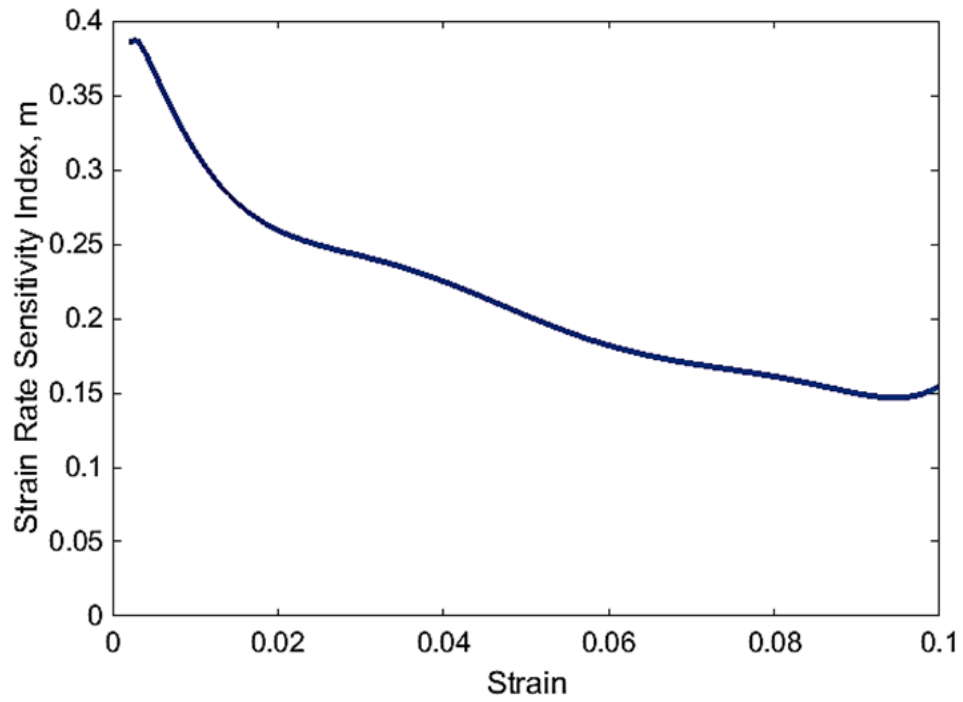
Figure 39 - Strain rate sensitivity index versus strain for LDPE.

4.3.3.4.2 Comparison of Indentation and Compression Stress-Strain Curves

When the results from the indentations are compared to the compression test results, we observe that the stress during indentation is higher than the uniaxial compression case for all three materials for the same amount of strain as was observed in the FE simulations. The ratio between indentation, slower strain rate, and compression can be plotted for all three materials as shown in Figure 40 through Figure 42. Comparing only the ratios of the initial viscoelastic portion, we get an average of 1.14 for PMMA, 2.22 for PC, and 1.31 for LDPE. These values are comparable to what was obtained from the FE simulations, thereby validating the model and showing that the difference in stress-states can be captured by the indentation models. These curves also have a minimum value at approximately where the material seems to yield after which the ratio increases.
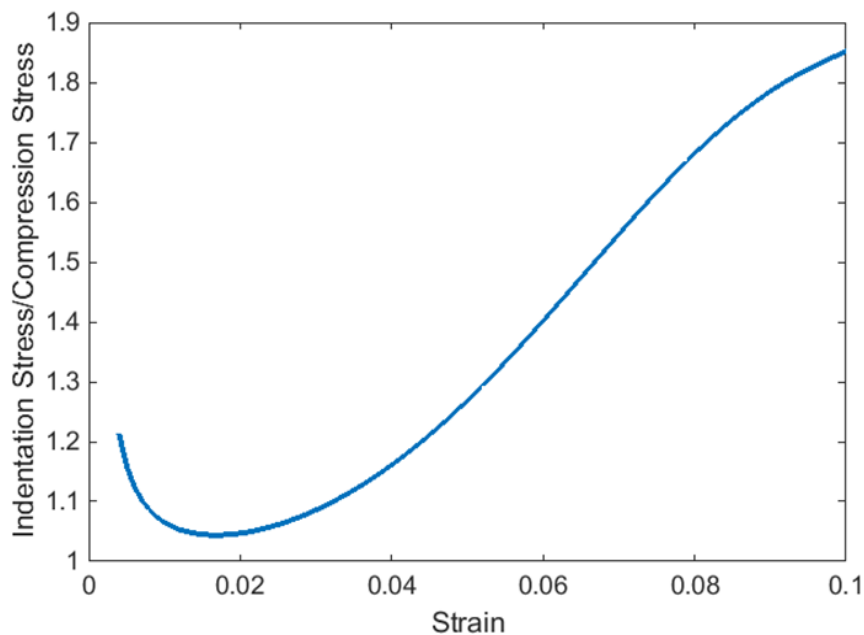
Figure 40 - Ratio between indentation stress and compression stress for PMMA.
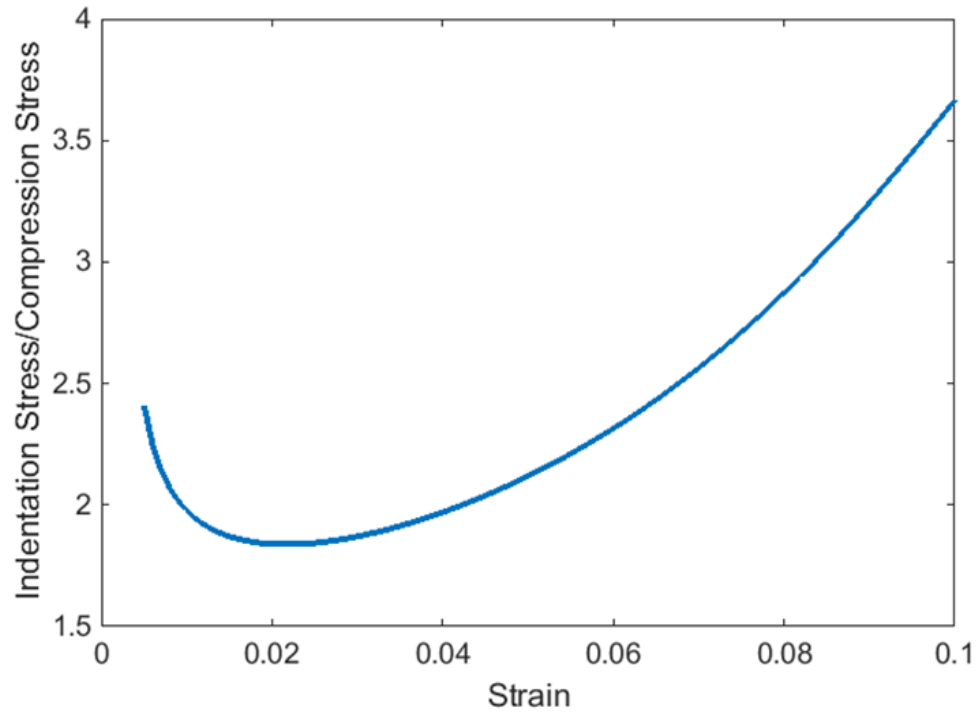
Figure 41 - Ratio between indentation stress and compression stress for PC.
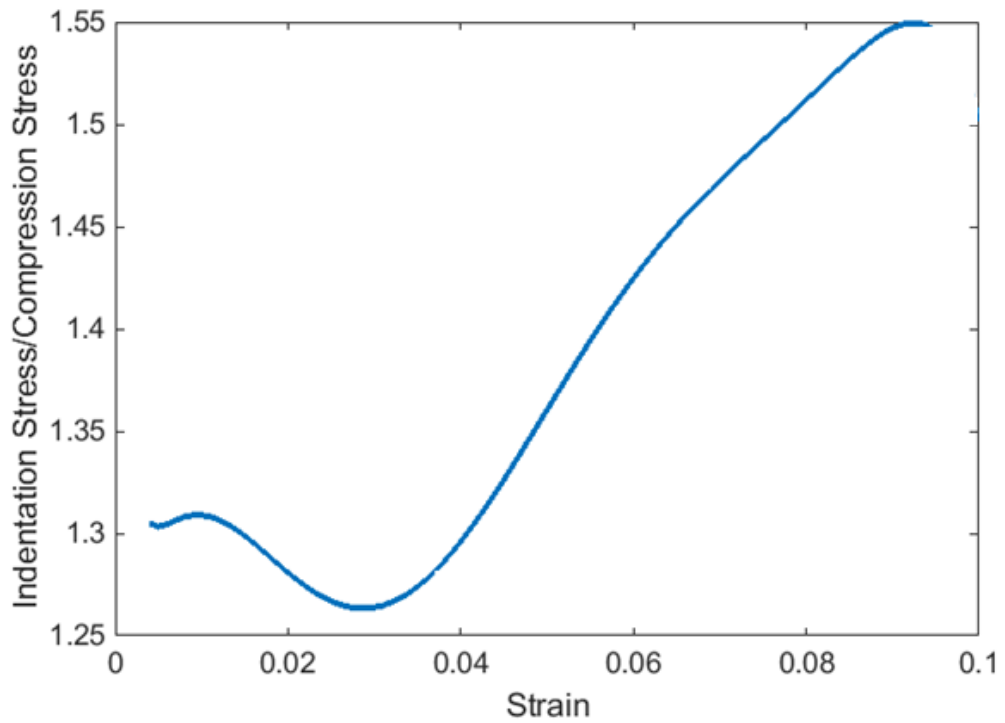
Figure 42 - Ratio between indentation stress and compression stress for LDPE.

4.3.4. Conclusions

A set of protocols to extract viscoelastic properties and indentation stress-strain curves from spherical nanoindentation using three different indenter tip sizes has been tested on commercially available polymers. The properties obtained were compared against all three tips and with results from compression tests on the same materials. While the indentation viscoelastic material properties were consistent across all the indenter sizes, the ratio between the instantaneous indentation modulus and the compressive modulus was about 1.6 for all three materials. The indentation stress-strain curves were also compared at two different strain rates and the effects of viscoelasticity were shown by calculating the strain rate sensitivity index. It was noted that LDPE was the most viscoelastic and PC was the least viscoelastic. The indentation stress-strain curves at the lower strain rate were also compared to the compression stress-strain curves. The ratios of the indentation stress to the compression stress in the initial viscoelastic region were compared to results obtained by FE simulations. They yielded comparable values and validated our model.

These results show that even though the stress state during nanoindentation is heterogeneous, the deformation behavior is comparable to uniaxial compression for different polymers. This new procedure has the advantage that a quantitative value of the material properties can be extracted and stress-strain curves can easily be produced. This new set of protocols provide a high-throughput method of analyzing different viscoelastic materials at different deformation rates without the need to prepare a new test sample for each case.

CHAPTER 5: SPHERICAL NANOINDENTATION ON THE BIO-POLYMER CHITOSAN

In a prior study, included in Appendix A, chitosan-alumina hybrid thin films with nacre-like microstructure were fabricated to mimic and investigate the mechanical function of nacre found in a large number of mollusks. Chitosan is a linear biopolymer derived by N-deacetylation of chitin [80]. In that study viscoelasticity was not considered because the focus was on the effect of relative humidity on the mechanical properties at different volume fractions of alumina. This chapter will focus on obtaining the viscoelastic properties of chitosan and extracting stress-strain curves using spherical nanoindentation at a set relative humidity.

5.1. Experimental Procedure

5.1.1. Materials

Low molecular weight chitosan (75-85% deacetylated) was purchased from Sigma Aldrich, St. Louis, MO, USA. Glacial acetic acid, deionized water, and tissue culture dishes were purchased from VWR International, Radnor, PA, USA. To prepare the chitosan samples for nanoindentation, first 3.6% (w/v) of low molecular weight chitosan was dissolved in 1% (v/v) glacial acetic acid in de-ionized water. The chitosan solution was homogenized on a bottle roller for 48 hours at room temperature (25°C). The solution was cast onto surface-treated tissue culture dishes, placed in a fume hood and allowed to dry at room temperature for at least 24 hours. Once dry, the film was slowly peeled by hand from the dishes. For nanoindentation, only samples with at least a

thickness of 1 mm were used. This was done so that the zone of indentation was within the material and not in the substrate it was glued onto. Since the sample was thin and sensitive to water, it could not be reliably polished without changing the surface chemistry. Therefore, the samples were used without any further modification.

5.1.2. Indentation Tests

The indents are performed on the surface of the chitosan and the spherical diamond tip used had a radius of 100 μm. All tests were performed after the measured indenter thermal drift rate reached and maintained a value of 0.05 nm/s. For all tests, temperature and relative humidity remained at 26.59 ± 0.017 °C and 32.93 ± 0.246 % respectively. CSM corrections were applied to all the tests as explained in section 2.2.1.1.

To find the range where the material is still viscoelastic, the chitosan sample was loaded and unloaded at the same rate with three different maximum loads. Before completely unloading the material, a pre-set load was left on the material for a period of time. A loading rate of 2.5 mN/s was used with maximum loads of 40 mN, 80mN, and 160mN. The load held at unload was 5 mN.

The viscoelastic property of chitosan was extracted using the ramp and hold test. The load was increased to three different loads at a constant loading rate and that load was held for 300 seconds and then unloaded at a constant unloading rate. The loading rate was 4 mN/s and the holding loads were 20 mN, 40 mN, and 60 mN. The viscoelastic properties were extracted from the hold portion of the tests. The stress-strain curves were extracted from the indentations done at rates of 0.05 s^{-1} and 0.5 s^{-1} as defined by the indenter.

5.2. Results and Discussion

5.2.1. Viscoelastic Region

The results from the tests to find the region of viscoelasticity for chitosan are shown in Figure 43. Figure 43 shows all curves for the three different maximum loads with at least five tests for each. For a maximum load of 40 mN the residual displacement was 331 ± 4 nm, for 80 mN it was 332 ± 13 nm, and for 160 mN it was 509 ± 7 nm. From these results it is seen that above a certain load there is an observable difference in residual displacements and it is assumed that the material may have experienced some plastic deformation above those loads. These results can be used to make a reasonable estimate of the load at which the curves can still be considered viscoelastic. This value is 80 mN for chitosan.
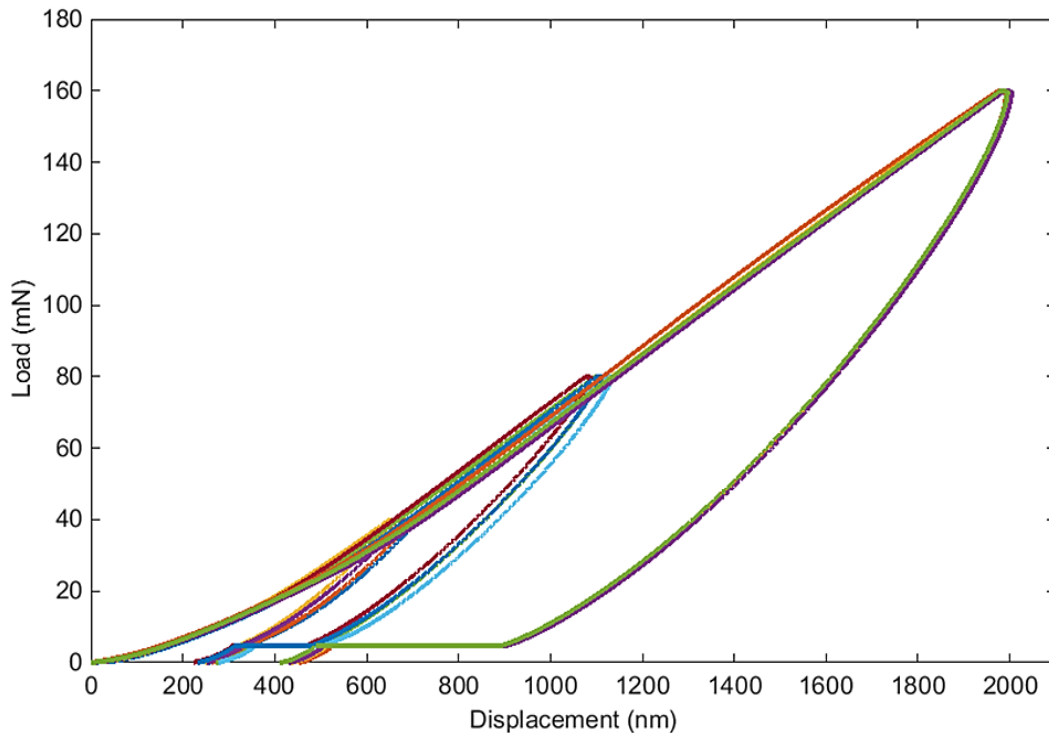
Figure 43 - Indentations to different loads on chitosan.

5.2.2. Material Viscoelasticity

The results from the indentations at two different rates are shown in Figure 44. These results show a clear difference between the load-displacement curves at the two rates. The slower strain rate shows some variability in the data which is most likely due to surface roughness or surface artifacts since the samples could not be polished. These results show that chitosan is clearly viscoelastic even at the low relative humidity that the tests were performed. Therefore time dependence should not be ignored in any mechanical tests that use chitosan as a material.
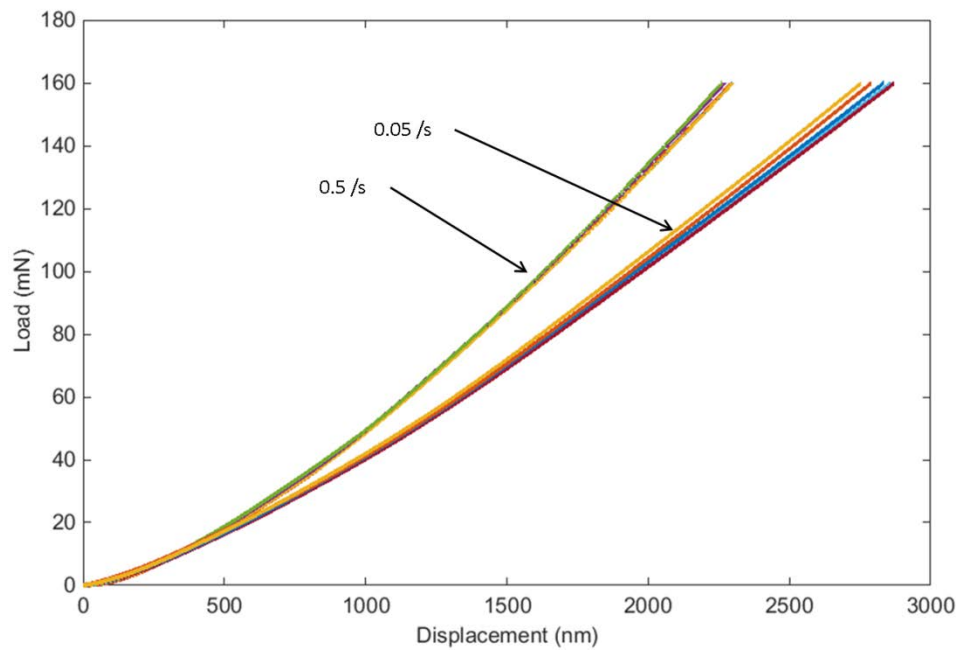
Figure 44 - Load-displacement curves of chitosan at two different loading rates.

The results from the creep tests are plotted in Figure 45. These results verify how viscoelastic chitosan is, as was seen in the load-displacement curves at different rates. These results will be used in the next section to extract the viscoelastic properties.
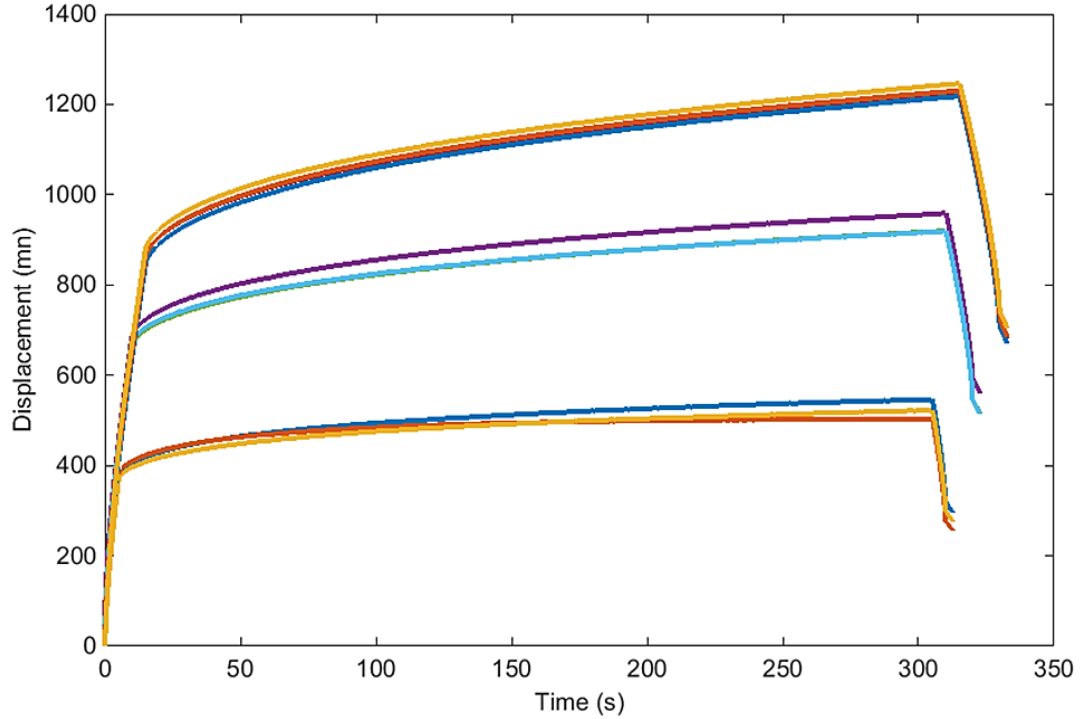
Figure 45 - Displacement vs time for creep tests performed on chitosan.

5.2.3. Viscoelastic Properties

The creep compliance and corresponding relaxation modulus were extracted using the methods explained in sections 3.2 and 2.1.4. The viscoelastic properties can be represented in terms of a two-term Prony series as shown in equation (93):

$$E(t) = 3.036 + 1.07e^{-t/16} + 1.52e^{-t/140} \quad GPa$$

$$J(t) = 0.336 - 0.037e^{-\frac{t}{19}} + 0.119e^{-t/220} \quad GPa$$

These results are plotted in Figure 46 and Figure 47. The tensile moduli obtained by the tests on the thin films can be compared to the instantaneous moduli obtained by nanoindentation. This comparison is plotted in Figure 46. The tensile modulus is higher than the modulus obtained by nanoindentation and the ratio between them is 1.5 comparable to that obtained with the commercial polymers.

88
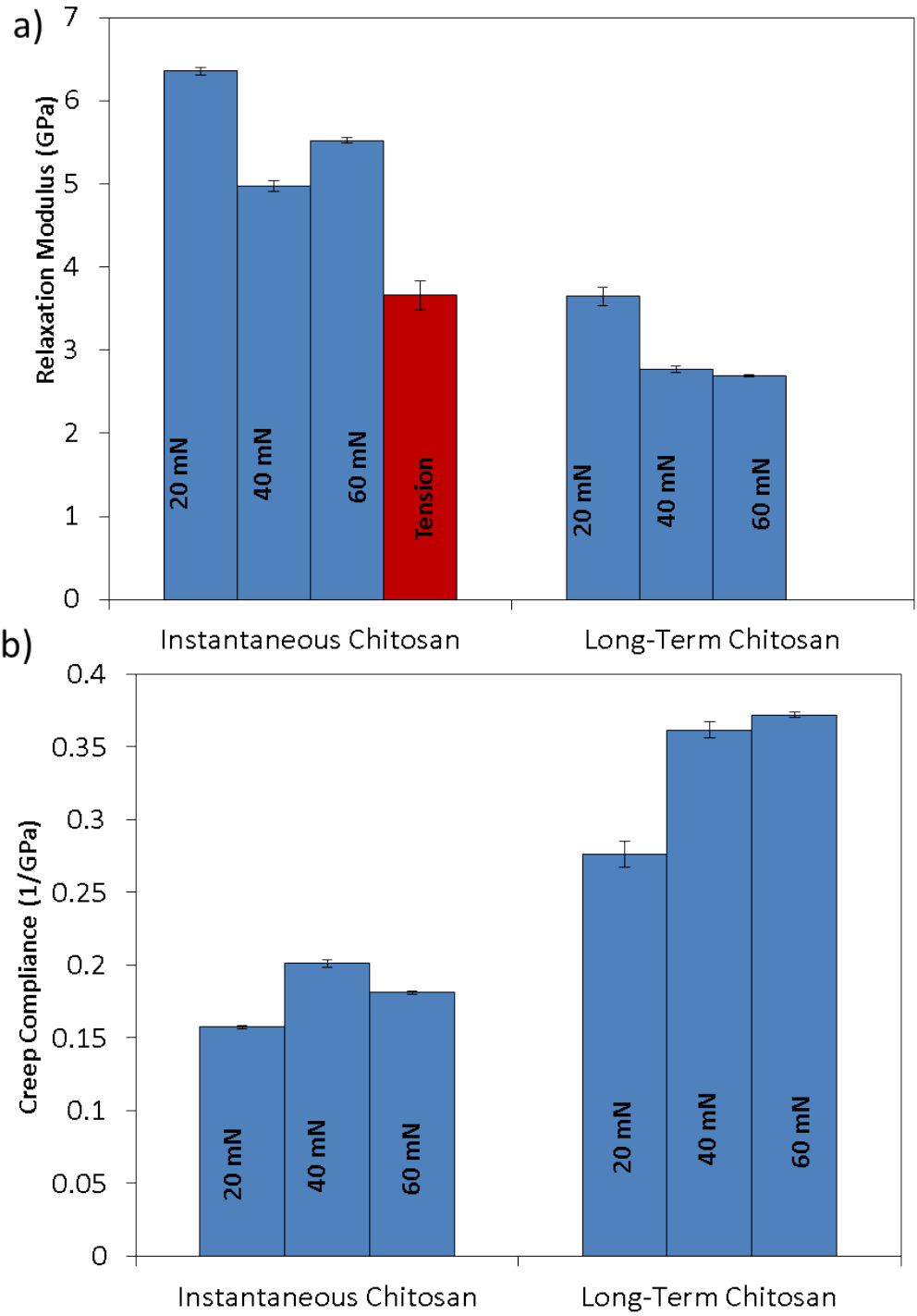
Figure 46 - a) Instantaneous and long-term creep compliance and b) instantaneous and long-term relaxation modulus for chitosan at the three holding loads. Compression modulus for chitosan is included in a).
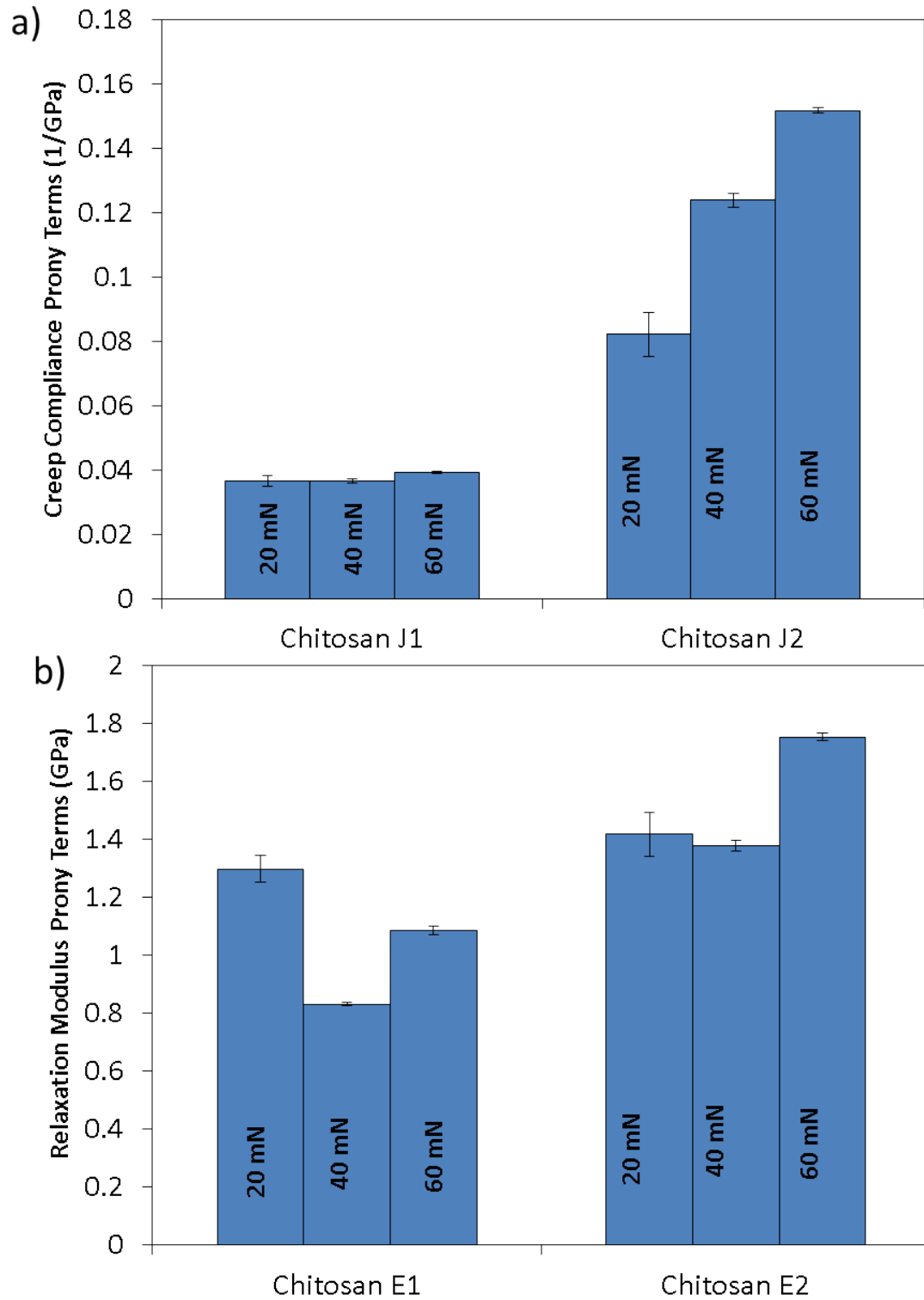
Figure 47 - Prony series terms for a) creep compliance and b) relaxation modulus.

5.2.4. Stress-Strain Curves

Once these properties have been extracted, the stress-strain curves can then be produced. First the zero-point is corrected for using the method explained section 3.3. The same method as in the previous chapter is used and a plot similar to Figure 33 is produced. The approximate corrected displacement and load are 300 nm and 3 mN. These values depend on the location of the indent, surface roughness, or other surface artifacts that may remain after polishing. With the corrections done, the load-displacement curves are converted to stress-strain curves using the method described in section 3.4. These results for the two different rates are plotted in Figure 48. As the strain increases there is also a difference between the indentations at the two loading rates. The faster rate tests show higher stresses at increasing strains as was observed with the commercial polymers.
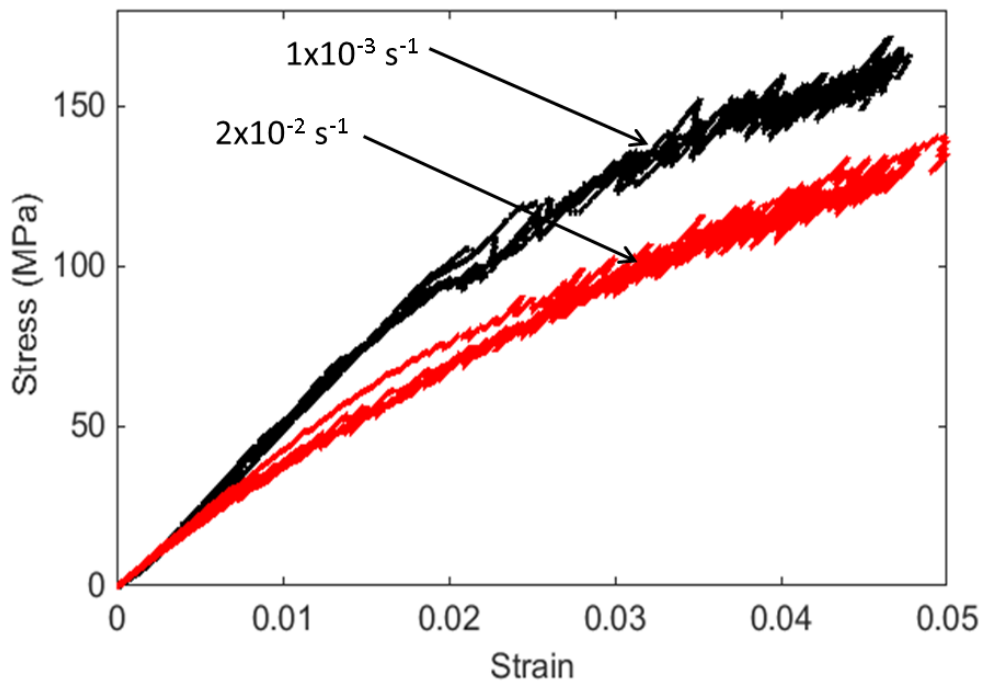
Figure 48 - Stress-strain curves for chitosan indentation at two different loading rates.

5.3. Conclusions

The set of protocols presented in chapter 3 were used to extract viscoelastic properties and stress-strain curves from spherical nanoindentation on the bio-polymer chitosan. Due to the sample being a film and have a relatively rough surface, only the 100 μm radius indenter could be used to extract reliable and consistent data. The properties obtained were compared with results from tensile tests on thin films of the same material. The ratio between the instantaneous modulus obtained from nanoindentation and that of the tensile modulus, at a similar relative humidity, was comparable to those obtained in the previous chapter for commercial polymers. The stresses observed were also higher at increasing strains, consistent with the effect of different stress states. This proves that the protocol presented can be extremely efficient in extracting material properties of viscoelastic biomaterials, especially when only small volumes are available as in this case.

CHAPTER 6: CONCLUSIONS AND FUTURE DIRECTION

The results obtained in these studies allow us to draw several important conclusions for the mechanical characterization of viscoelastic materials using spherical nanoindentation. While some fundamental questions remain, especially on the effect of indentation zone size on different polymer structures, a new set of protocols to extract viscoelastic properties and stress-strain curves have been presented and tested. This chapter summarizes the key findings and presents suggestions for future work to be done.

6.1. Conclusions

This dissertation presented a set of protocols to accurately extract material viscoelastic properties and indentation stress-strain curves from spherical nanoindentation tests performed on polymers. To the best of our knowledge, this the first systematic study of all the steps involved using spherical nanoindentation to extract full stress-strain curves from viscoelastic materials. These protocols were tested on polymethyl methacrylate, polycarbonate, low-density polyethylene, and the bio-polymer chitosan. The goal was to show that spherical nanoindentation can be reliably used to probe time-dependent materials and extract useful information with a simple set of protocols. The steps of the protocols, how they should be used, and the conclusions drawn from this study are summarized below.

1. For any properties extracted to be meaningful, it is important to be sure that the region they are extracted from is representative of the original undeformed sample. This is why it is important to know how much load the material can

handle before it becomes plastically deformed. The method used in this dissertation is to load, to a maximum load, and unload the material at a specific loading and unloading rate. Before fully unloading a small load is held on the material and the displacement is measured. This is done for different maximum loads and once the material has been plastically deformed, the residual displacement will be higher than the other cases. This method has shown consistent results with the tested materials in this study. Since this is a one-time cost and approximation for each material and indenter tip size, care should be taken to get a reliable value that can be used for all further tests on the material. For materials with much higher viscous components, this may pose a problem as it may take a very long time for residual displacement to be reached. This can be inconvenient and time consuming if the goal of the indentation tests is to rapidly test a series of different materials.

2. Once an approximate value of the viscoelastic region is known, the viscoelastic properties can then be extracted. This is done by loading the material at a constant loading rate and then holding a maximum load for a set period of time before unloading. Using a loading ramp that has a constant loading rate is convenient because an analytical form of the viscoelastic equation that does not include an integral can be formed. This was picked over a displacement controlled method since that results in a relationship that cannot be solved analytically. It is important to take into account the dynamics of the machine and make sure the indenter can handle the speed of indentation and produce enough data points for analysis. Different holding loads and indenter tip sizes were used to extract the

properties to show that there is not much variance in the properties within the viscoelastic region and in some cases the regions we assume are no longer viscoelastic. These results show that a zero-point correction is not needed for these tests as they are consistent without a need for correction. Since for some of the materials, LDPE and chitosan, the properties were consistent even in regions that were assumed to no longer be viscoelastic, this step may also be used to determine the viscoelastic region.

3. Once these preliminary steps are performed, indentations can then be performed. The tests are performed at a constant rate defined by the indenter as the loading rate divided by the measured load. This condition is used as it gives a relatively constant strain rate once the load-displacement curves are converted to indentation stress-strain curves. After the data is collected and corrected for the CSM signal, an effective point of initial contact has to be found for each indent. The method used in this dissertation was formulated directly from the viscoelastic solution to the spherical nanoindentation problem and has shown consistent results for all the materials used.

4. After the zero-point correction is performed, the stress-strain curves can then be produced using the definitions of stress and strain provided. Our results show consistent stress-strain curves for all the strain rates and indenter tip sizes used in the experiments. Finite element studies were used to verify some of the trends observed in the initial viscoelastic region. The ratio between indentation stress and compression stress at similar strains and strain rates were compared and

consistent trends were found. For the commercial polymers, LDPE was found to be the most viscoelastic and PC was the least.

With this protocol the properties and stress-strain curves can easily be extracted from nanoindentation on time dependent materials. Once the user is acquainted with the protocols, the whole procedure should take about one week for a series of materials since the data analysis portion can be automated. This new set of protocols is a simple process that has provided insight into stress-strain behavior of viscoelastic materials at the micro-scale. This provides an accurate and fast method of investigating new polymers, bio-polymers, or natural materials containing viscous components.

6.2 Future Direction

The set of protocols presented in this dissertation have only been tested on materials at room temperature without looking into the dynamic properties of the materials. To truly extract the full spectrum of the viscoelastic properties of any time dependent material, it would be useful to perform indentations at a range of temperatures. The dynamic properties can also be extracted by pushing the indenter into the material and oscillating either the displacement or load. With results from these tests, the time-temperature superposition principle can be used to determine frequency dependent properties at various temperatures or a correlation between properties at different frequencies and temperatures.

Another direction is to use a different method to extract the relaxation modulus rather than the creep compliance. This relaxation modulus can then be compared to the one extracted from the ramp and hold load method to get creep compliance. While ideally they should not be different, the type of test performed may cause the material to

experience more force relaxation of displacement creep. It would also be useful to obtain two independent measurements of the mechanical properties to have a more reliable analysis.

While the tests on chitosan were performed at one relative humidity, they can also be performed at different humidities once a reliable setup to control the relative humidity during the tests is fabricated. With results at different humidities, a correlation can be made between the mechanical properties and changes in humidity. This gives a better view of the applications of the thin films in different environments.

APPENDIX A

NACRE-LIKE HYBRID FILMS: STRUCTURE, PROPERTIES, AND THE EFFECT OF RELATIVE HUMIDITY

Mohammed T. Abba, Philipp M. Hunger, Surya R. Kalidindi, Ulrike G.K. Wegst[*]

M. T. Abba, Prof. S. R. Kalidindi
The George W. Woodruff School of Mechanical Engineering
Georgia Institute of Technology, Atlanta, GA 30332-0405, USA
Dr. P. M. Hunger, Prof. U. G. K. Wegst
Thayer School of Engineering, Dartmouth College, Hanover, NH 03755, USA

Functional materials often are hybrids composed of biopolymers and mineral constituents. The arrangement and interactions of the constituents frequently lead to hierarchical structures with exceptional mechanical properties and multifunctionality. In this study, hybrid thin films with a nacre-like microstructure were fabricated in a straightforward and reproducible manner through manual shear casting using the biopolymer chitosan as the matrix material and alumina platelets as the reinforcing particles. The ratio of inorganic to organic content was varied from 0% to 15% and the relative humidities from 36% to 75% to determine their effects on the mechanical properties. It was found that increasing the volume fraction of alumina from 0% to 15% results in a twofold increase in the modulus of the film, but decreases the tensile strength by up to 30%, when the volume fraction of alumina is higher than 5%. Additionally, this study quantifies and illustrates the critical role of the relative humidity on the mechanical properties of the hybrid film. Increasing the relative humidity from 36% to 75% decreases the modulus and strength by about 45% and triples the strain at failure.

1. Introduction

A considerable research effort is currently focused on the synthesis of stronger, tougher, and "greener" materials based on the principles of function and optimization found in natural materials.[2-5] This is because natural materials often exhibit a superior mechanical performance in comparison to their synthetic, monolithic counterparts due to their hierarchical structural arrangements.[11, 81, 82] One example of such a natural material, that has attracted particular interest in recent years, is nacre. Also termed 'mother of pearl', it forms the inner layer of the shells of a large number of mollusks (e.g., abalone), and has demonstrated impressive performance under tensile loading.[83] Nacre is essentially a two-phase composite material with an intricate, interlocked brick-and-mortar structure comprised of about 95 vol.%, of hexagonal aragonite platelets 'glued' together by a thin polymer film (~10–50 nm thick) composed of proteins and polysaccharides.[84-86] The tensile strength of nacre is about 78-130 MPa (wet) and 90-167 MPa (dry), and the Young's modulus is about 58-70 GPa (wet) and 68-90 GPa (dry).[84] With a high volume fraction of ceramic, one would expect the material to be brittle. However, nacre has a work of fracture as high as 1240 J m^{-2}, in a three-point bending test, which is about 3000 times greater than that of monolithic $CaCO_3$.[85, 87] The work of fracture, in this case, is defined as the critical strain energy release rate or the energy necessary to drive a crack through a sample. This intriguing observation and the relative simplicity of the structure of nacre was the motivation for this study of fundamental structure-property relationships, including the often neglected effect of moisture, in a nacre-like model material system .[86]

The bio-inspired research presented here aims to identify the principles of function and optimization in biological materials and to mimic the same in engineered material systems. Numerous studies have described materials that match or even exceed the properties of nacre.[4-7, 9, 10] For example, using a layer-by-layer (LBL) assembly yields nanocomposites that can have tensile strengths up to 400 MPa.[4-6, 9] Freeze casting yields, when infiltrated by a second phase, layered structures that are up to 300 times tougher than its constituents.[2, 7, 10] Toughness, in this case, is defined as the plane-strain fracture toughness, K_{Ic}. Casting methods, such as slip-casting,[3] evaporation,[88] and combined gel-casting and hot-pressing,[89, 90] all yielding a brick and mortar structure, have been reported to produce materials with tensile strengths up to 250 MPa, thus exceeding that of nacre. Samples with a nacre-like structure that can be produced using some of the techniques described in prior literature are usually extremely small in volume and require time-consuming processes and specialized equipment. The scaling-up both of sample volumes and production rates for real-life applications continues to pose considerable difficulties and usually leads to a considerable loss in mechanical properties.

The use of self-assembly mechanisms is increasingly being explored to overcome these problems. Taking advantage of particle self-assembly that occurs during freeze casting, for example, the manufacture of large sample sizes with a nacre-like structure could recently be demonstrated.[91] The resulting cellular materials, composed of alumina platelets in a chitosan-gelatin matrix, had a honeycomb-like structure, whose cell walls exhibited nacre-like structures and resulted in considerably improved mechanical properties both parallel and perpendicular to the long pore axis.[91, 92] In an effort to

better understand the mechanisms that determine the mechanical properties of the wall material of the freeze-cast scaffolds and to mimic the structure of biological materials in a well-controlled model system, we fabricated alumina-platelet reinforced chitosan films. Alumina platelets were chosen as the inorganic ceramic phase because of their close resemblance, in shape and aspect ratio, to the aragonite platelets in nacre.[93] Chitosan, a linear biopolymer derived by N-deacetylation of chitin was chosen for the matrix material, because it is ideally suited for a study of property dependence on relative humidity.[80]

One critical factor that is frequently not addressed and reported is the effect of moisture content on the mechanical properties of the films produced. Since chitosan readily absorbs water, its mechanical properties will greatly vary depending on the relative humidity of the environment at the time of the test.[94] Chitosan films have been reported to have as much as a 99% loss in Young's modulus and 88% loss in stress at break when immersed in deionized water for one night and an 80% loss in tensile strength when the conditioning relative humidity was increased from 15.6% to 93%.[94, 95] To investigate the effect of moisture content, this study focused on controlled relative humidities of 35%, 55%, and 75%.

A relatively simple and reproducible processing method to fabricate thin hybrid films is utilized in this study. The goals are to show that the films produced using this technique result in highly aligned microstructures, to investigate the mechanical properties of these films in tension, and to show that relative humidity of the environment can have a significant effect on the measured mechanical properties.

2. Mechanical Properties

Prompted by investigations into the toughness of nacre (and bone), the mechanics of polymer composites reinforced with anisotropic particles have been pursued in depth in recent years. Models have been developed that describe, how the aspect ratio of the platelets, the properties of the different phases as well as that of the interfaces determine the failure mode of the whole composite.[86, 96, 97] Two simple rule of mixture models are commonly used to describe the mechanical behavior of two-component composites with continuous and aligned phases: the Voigt model and the Reuss model.[98, 99] The Voigt model, mostly applicable in the case of a composite with fibers running parallel to the loading direction, as shown in **Figure 49**a, assumes that the whole composite experiences the same strain. This case is dominated by the stiffer and stronger phase and describes the upper bound of the achievable mechanical properties. The Reuss model, applicable in the case of a composite with fibers running perpendicular to the loading direction, as shown in **Figure 49**b, assumes that the whole composite experiences the same stress. This case is dominated by the softer phase and describes the lower bound of the achievable mechanical properties. Since our composites do not have continuous phases, these models are only used to define the upper and lower bounds of the composite's stiffness.
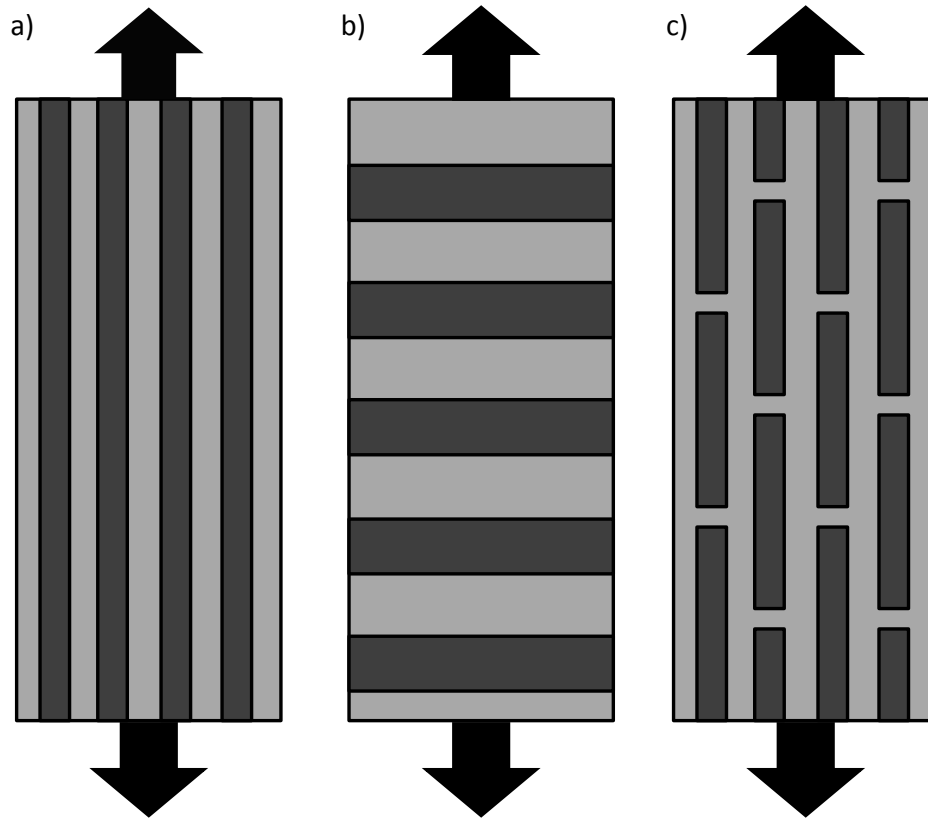
Figure 49 - Models to describe mechanical bahvior of composites: a) Voigt model, b) Ruess model, and c) Jaeger Fratzl model.

Jaeger and Fratzl showed that the microstructure of biocomposites can be described by staggered mineral bricks in a protein matrix as shown in **Figure 49**c.[100] In tension, the mechanical behavior of the Jaeger-Fratzl model can be represented using the shear lag model, in which the mineral platelets are loaded in tension and the protein matrix transfers the load between platelets via shear stresses as shown in **Figure 50**. Models that describe the mechanical behavior of particulate reinforced composites, such as nacre and the alumina-reinforced chitosan films studied here, include the Padawer-Beecher model for composite modulus and the Glavinchevski model for the composite strength.[101, 102] The Padawer-Beecher model is based on a force balance on an

103

individual platelet assuming the composite material follows the shear lag model. The

Padadwer-Beecher model estimates the composite modulus as:

$$E_c = V_f E_f \left[1 - \frac{\tan u}{u} \right] + (1 - V_f) E_m \tag{95}$$

$$u = s \sqrt{\frac{G_m V_f}{E_f(1 - V_f)}} \tag{96}$$

where *s* is the aspect ratio of the platelets, *E* is the elastic modulus, *V* is the volume

fraction, *G* is the shear modulus of the matrix phase, and the subscripts *c*, *m*, and *f* denote

the composite, matrix, and filler phase, respectively.
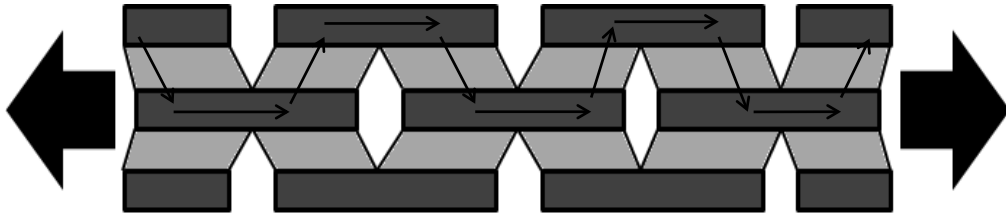
Figure 50 - The shear lag model transfers load between the mineral platelets, where most
of the load is carried, via interfacial shear stresses.

The ultimate tensile strength of the composite can be modeled using the

Glavinchevski model as:

$$\sigma_c = \alpha V_f \sigma_f + (1 - V_f) \sigma_m \tag{97}$$

where σ is the tensile strength. The factor α is a function of the platelet aspect ratio, the

matrix yield shear strength, and the tensile strength of the platelets.[101] The failure

mode of the composite is determined by the aspect ratio of the platelet.[96] The critical

aspect ratio of the platelet can be determined by the length at which the stress build-up in the platelets is equal to its tensile strength as shown in **Figure 51**. The critical aspect ratio can also be estimated by the ratio of the platelet strength to the lower value among the shear strength of the matrix, τ_y, and the shear strength of the polymer-platelet interface, τ_i. For the case where the aspect ratio of the platelet is greater than the critical value, the platelets fracture, leading to a brittle failure of the composite and the factor α can be defined as:

$$\alpha = 1 - \frac{\sigma_f}{2\tau_{min}s} \tag{98}$$

where τ_{min} is either the shear strength of the matrix or the shear strength of the polymer-platelet interface whichever is lower.[4] For the case where the aspect ratio of the platelet is lower than the critical value, the matrix will yield before the platelet, leading to platelet pull-out and plastic yielding of the matrix before the composite completely fails.[82, 103] The factor α is then defined as:

$$\alpha = \frac{\tau_{min}s}{2\sigma_f} \tag{99}$$
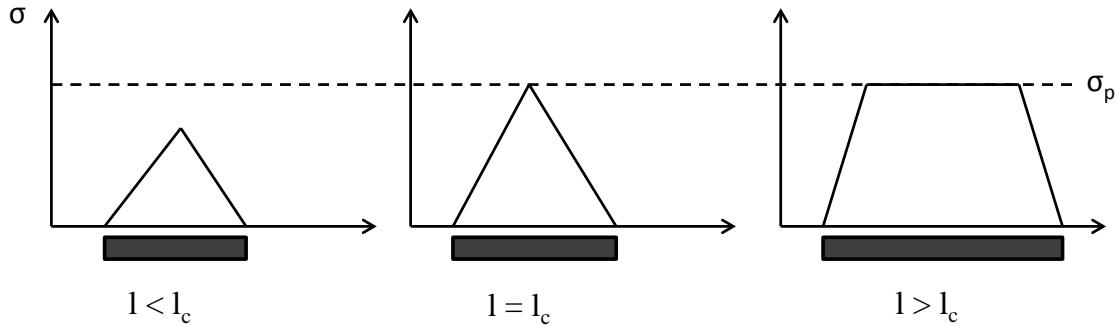
Figure 51 - Variation of tensile stress in the platelet as a function of its length. σp is the platelet fracture strength.

In the models discussed, the following assumptions were made to simplify the calculations: the matrix adheres perfectly to the platelets; the platelets don't interact with each other; all the platelets have the same dimensions; the platelets are arranged parallel to and equidistant from each other; the moduli of all the platelets are the same; and the matrix is linearly elastic. The first assumption is dependent on the surface chemistry between the platelet and the matrix and that there are no pores generated during processing of the matrix. As the volume fraction of the platelets is increased, the likelihood of particle clustering, interactions, and disorder increases, leading to the second and fourth assumptions not being satisfied. For smaller dimensions, manufacturing limitations may cause a larger variation in the dimensions of individual platelets, which may not satisfy the second assumption. If using crystalline platelets, changes in crystal orientation between individual platelets may lead to differences in their modulus; however, they would probably cancel out with a large volume of platelets. The matrix, being a polymer, is most likely viscoelastic. For higher accuracy of the models, it is important to include the time and temperature dependence of the matrix mechanical properties into the models, which in the case of biopolymers are significantly affected by relative humidity.

3. Results and Discussion

3.1. Fabrication of Hybrid Composites

A method to fabricate ceramic-reinforced polymer hybrid films with highly aligned microstructures in larger sample volumes and faster processing times is introduced. The films have been successfully fabricated with volume fractions of ceramic platelets ranging from 5 vol.% to 15 vol.% by first making a slurry of alumina platelets in

a chitosan solution and then using a slip casting method. For best results, it is important to use surface-treated tissue culture dishes, which allow for better wettability between the dish and the chitosan-alumina slurry. The films can be produced with thicknesses ranging from 15 μm to 75 μm and can easily be peeled off, once dry. We found that volume fractions of alumina greater than 15% rendered the dry films too brittle to be removed intact from the petri dish.

3.2. Structural Analysis

Analysis by scanning electron microscopy, shown in **Figure 52**, revealed that the platelets are very uniformly distributed in the matrix and aligned parallel to the film's free surfaces. The cross-sections show that the platelets form a brick and mortar like structure similar to that found in nacre and the freeze-cast scaffolds. **Figure 52** further shows, how the structure changes with an increasing platelet volume fraction and that there appears to be very little increase in misalignment with increasing ceramic volume fraction. The misalignment appears primarily to be due to the freeze-fracturing process before imaging. There also appears to be increased clustering at higher volume fractions, which may result in films with lower composite strengths as discussed in the next section.
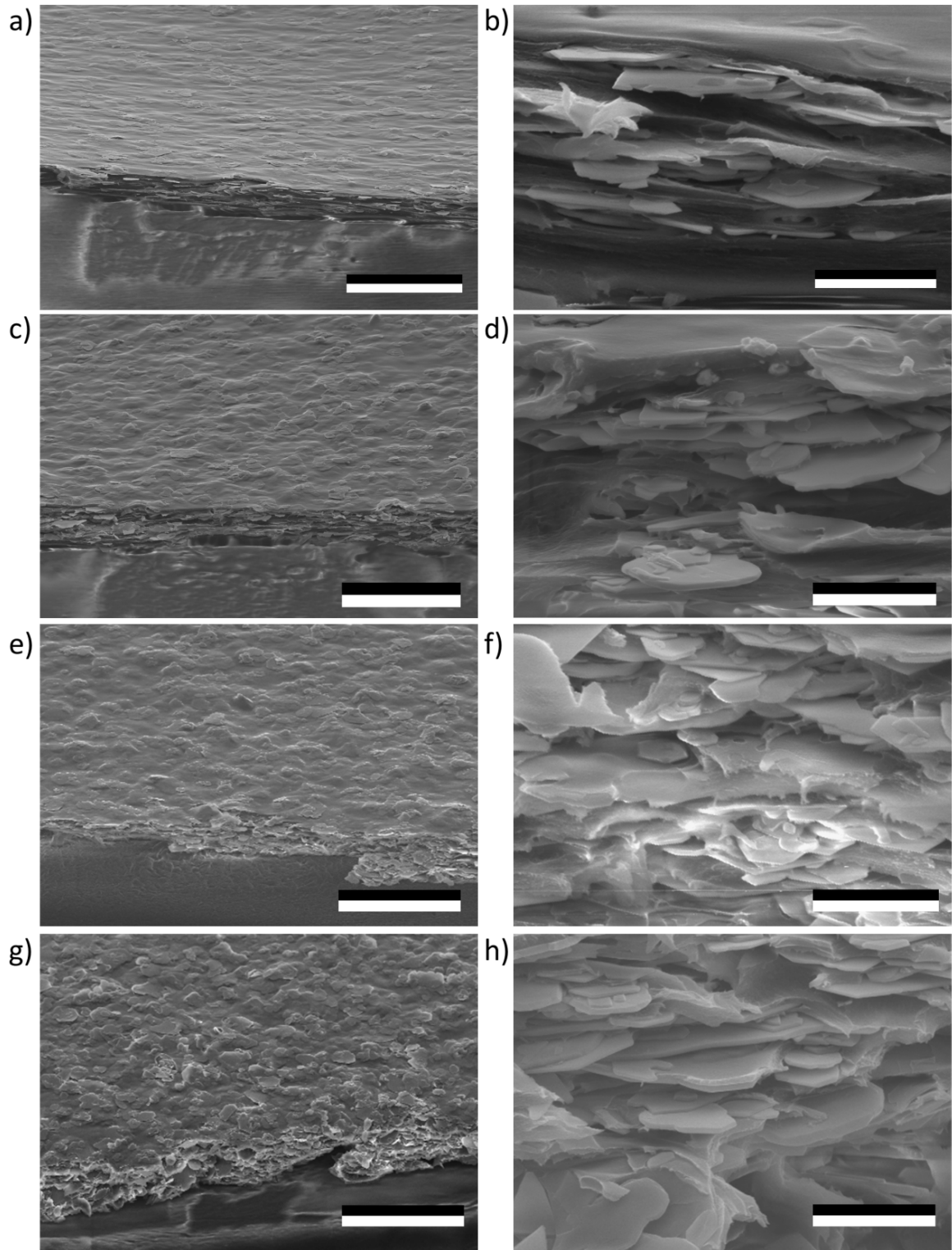
Figure 52 - Films with 5% a,b), 10% c,d), 15% e,f), and 20% g,h) volume fraction of alumina platelets (scale bars are 50μm for a,c,e,g) and 5μm for b,d,f,h)).

3.3. Mechanical Characterization

Alumina reinforced free-standing chitosan films with different volume fractions of alumina were mechanically tested in tension, at three relative humidities of 35%, 55%, and 75%. Typical true stress – true strain plots, shown in Figure 53, illustrate that the Young's modulus increases and the strain at failure decreases with increasing platelet volume fraction.
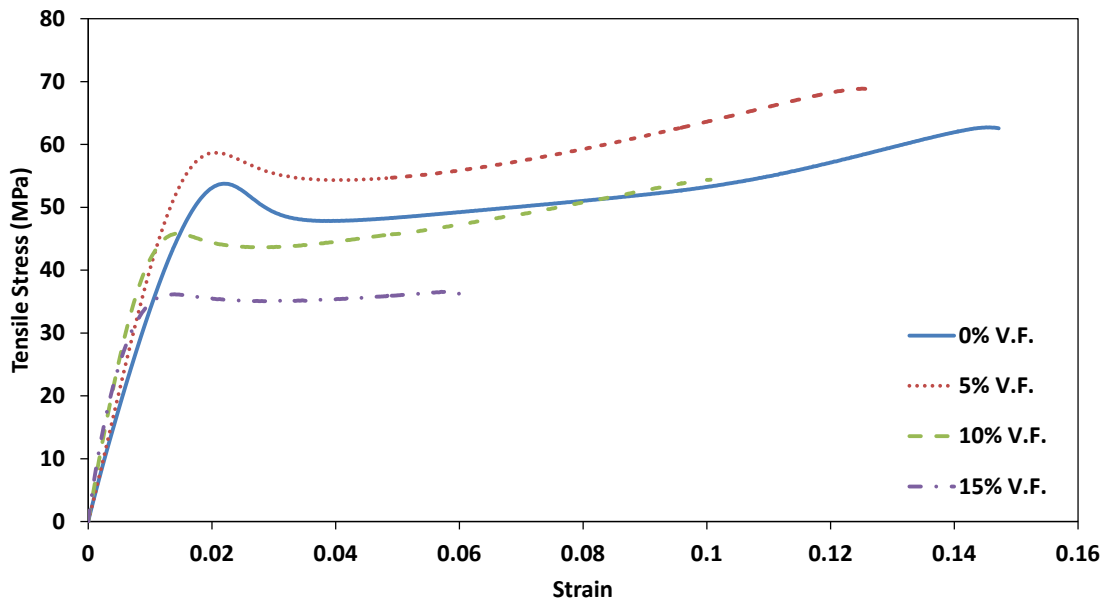
Figure 53 - Typical tensile stress versus strain curves of chitosan-alumina films with increasing volume fractions (V.F.) of alumina platelets (displacement rate is 1 mm s-1, relative humidity is 55%).

3.3.1. Elastic Modulus

The elastic modulus was calculated from the slope of the initial linear region of the stress-strain curves. The Padawer-Beecher model described by Equation (95) was used to estimate the elastic modulus of the chitosan-alumina films. The platelets had an

average thickness and diameter of 400±100 nm and 7.5±2.5 μm respectively, giving them an aspect ratio of about 19.[91] The elastic modulus of the alumina platelets was assumed to be 375 GPa,[104] and the shear modulus of the chitosan film was calculated, using the model assumption of a linear elastic material, by the relationship:

$$G_m = \frac{E_m}{2(1 + \nu)} \qquad (100)$$

where ν is the Poisson ratio of chitosan, $\nu = 0.272$.[105] Since the elastic modulus of chitosan can vary depending on the relative humidity of the environment at the time of testing, the elastic modulus of the pure chitosan films as the matrix in the Padawer-Beecher model was determined experimentally for the three different relative humidities.

We also compared our results with average values found in the literature for materials reinforced with nano-size platelets at volume fractions similar to the ones studied here. Bonderer et al. fabricated freestanding chitosan-alumina hybrid thin films using a layer-by-layer method.[5] The alumina platelets were surface modified with 3-aminopropyltriethoxysilane (APS) to improve the platelets' adhesion to the matrix. Bonderer at al. also fabricated polypropylene-alumina and polyurethane-alumina hybrid thin films using a gel-casting and hot-pressing method.[89, 90] Shukla et al. fabricated epoxy-alumina hybrid thin films using a curing method.[106] The study reported here was performed with uncoated platelets and platelets surface modified with 3-glycidoxypropylmethoxysilane (GPS) to improve platelet adhesion to the matrix.

The elastic modulus results for our study, predictions from the Padawer-Beecher model, and the literature values are plotted in **Figure 54a**. Our results show that increasing the platelet fraction increases the tensile modulus and increasing the relative

humidity decreases the tensile modulus of the composite. Our results also show a good experimental correlation to the model prediction. The same trend is observed in composites characterized by other researchers with property values dependent on the matrix material used. Since no mention is made of the relative humidities at which the literature values were obtained, it is not possible to provide a meaningful direct comparison with these.
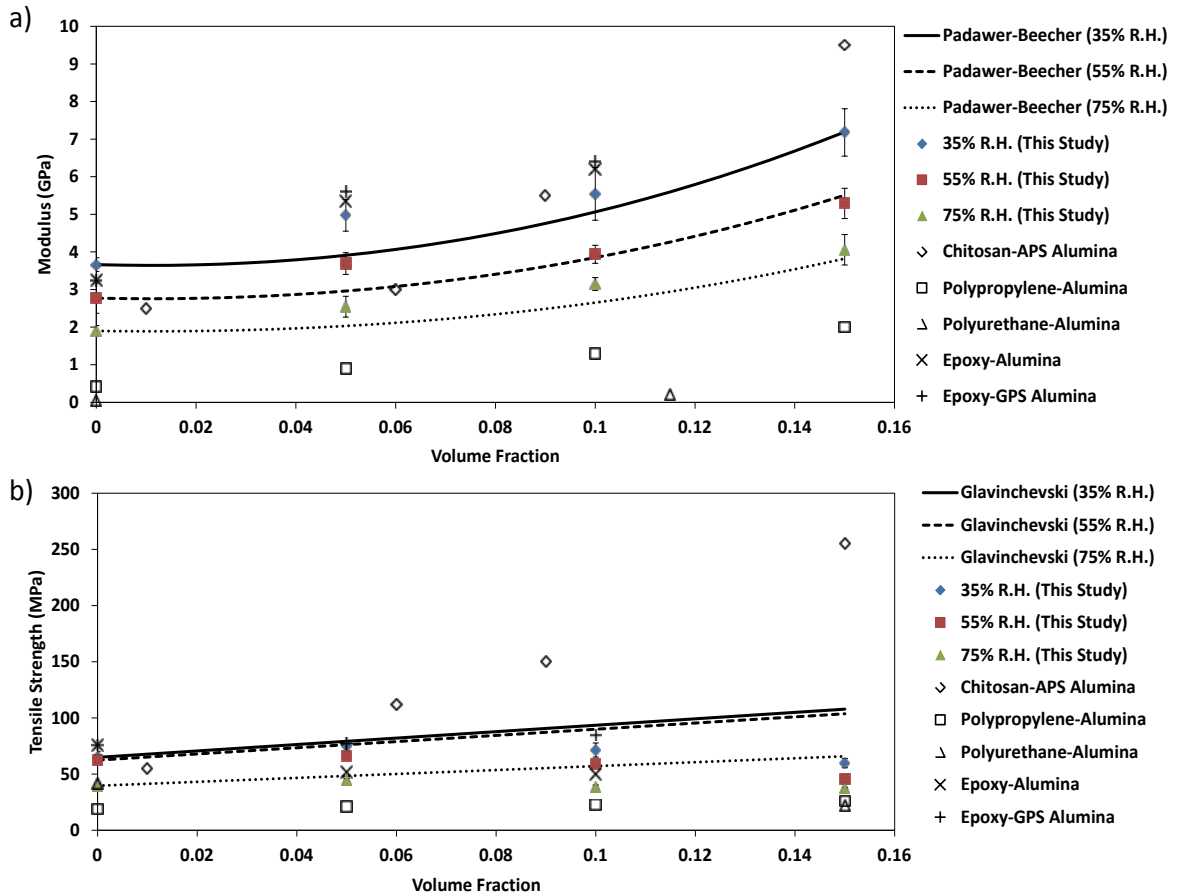
Figure 54 - a) Tensile modulus and b) tensile strength as a function of platelet volume fraction at three different relative humidities. Included are predictions of the composite a) tensile modulus based on the Padawer-Beecher model, b) tensile strength based on the Glavinchevski model, and literature values for chitosan-APS alumina[5], polypropylene-alumina[89], thermoplastic polyurethane[90], epoxy-alumina[106], and epoxy-GPS alumina[106] hybrid composites.

3.3.2 Tensile Strength

Tensile strength was calculated from the maximum stress reached during the tests. The Glavinchevski model described by Equation (97) is used to estimate the tensile strength of the chitosan-alumina composite. Since we are assuming that the matrix adheres perfectly to the platelets, the matrix will yield before the polymer-platelet interface, and the shear strength of the polymer will be used to estimate the critical aspect ratio and the mode of failure of the composite. The tensile strength of the alumina platelets is taken to be $\sigma_p = 2$ GPa and the shear strength of the polymer is estimated, using the von Mises criterion, to be $\tau_y = 0.577\sigma_m$ at the three different relative humidities.[4, 107] The critical aspect ratio is then 53.4, 55.5, and 87.4 for the 35%, 55%, and 75% relative humidities, respectively. The platelet aspect ratio is 19, which is lower than the critical aspect ratios, so Equation (99) is used to estimate the α factor meaning that the matrix should ideally yield before the platelet. In this case α is 0.18, 0.17, and 0.11 for the 35%, 55%, and 75% relative humidities, respectively.

The tensile strength results of our study, predictions from the Glavinchevski model, and the literature values are plotted in **Figure 54**b. We notice an initial increase in tensile strength but the strength decreases as the volume fraction of the platelets is increased beyond 5%. The reduction in strength, we suggest, is due to the introduction of flaws, such as porosity formed when the particles are added to the matrix, or insufficient bonding of the platelets to the chitosan matrix, so that full debonding is initiated early and occurs well before the matrix fails. Porosities are further increased in the material once debonding has occurred and the strain increases. Additionally, we also notice increased clustering of the platelets with increasing volume fraction (**Figure 52**), which causes an

increase in the stress concentrations around those areas leading to cracks being formed. Composites in the literature, in which the surfaces of the alumina platelets were not modified to enhance adhesion, show a decrease in strength with increasing platelet volume fraction. For the composites whose particles surfaces were modified, the strength increases with increasing platelet volume fraction especially in the case of Bonderer et al.,[5] with a 500% increase in tensile strength at a 15% volume fraction of platelets. This suggests that enhancing the bond between the matrix and platelets can significantly improve the tensile strength of the composite.

3.3.3 Effect of Relative Humidity

Table 6 shows that a decrease in relative humidity results in an increase in elastic modulus and tensile strength and a decrease in the strain at failure. The three stress–strain curves shown in **Figure 55** for a film with 10 % volume fraction alumina show this even more clearly. The tensile modulus and strength decrease by about 45% with an increase of relative humidity of 20%, whereas the strain at failure is almost tripled; as the humidity increases, the films absorb more of the plasticizer water, rendering the polymer phase more ductile. This dramatic effect of the moisture content on the mechanical properties shows that it is very important to take into account the environmental conditions, when mechanical tests are performed on samples containing significant amounts of biopolymers such as chitosan. Humidity can further play a crucial role in determining the material's performance and effectiveness for a given application.
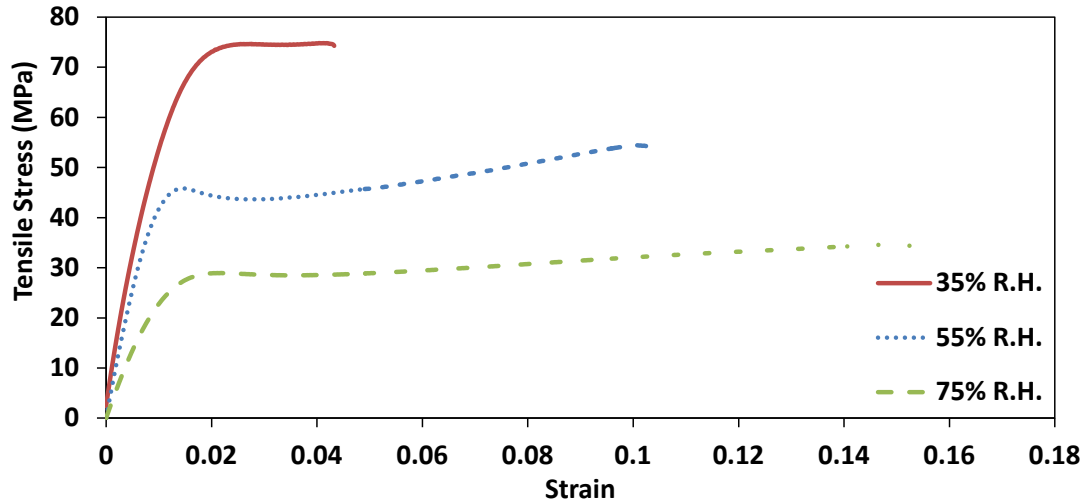
Figure 55 - Tensile stress versus strain of 10% V.F. alumina-chitosan films conditioned and tested at three different relative humidities.

Table 6 - Mechanical properties of chitosan-alumina films at different relative humidities and platelet volume fractions.

Volume Fraction [%]	Relative Humidity [%]	Elastic Modulus [GPa]	Tensile Strength [MPa]	Strain at Failure [%]
	35	3.66 ± 0.18	64.9 ± 5.04	4.6 ± 1.03
0	55	2.77 ± 0.4	62.43 ± 3.03	12.3 ± 1.13
	75	1.9 ± 0.14	39.64 ± 1.62	19.85 ± 0.92
	35	4.97 ± 0.42	74.42 ± 4.78	6.72 ± 0.79
0.05	55	3.69 ± 0.29	65.64 ± 1.74	12.89 ± 0.51
	75	2.54 ± 0.28	44.55 ± 1.45	16.65 ± 1.48
	35	5.54 ± 0.7	71.37 ± 6.27	4.98 ± 0.32
0.1	55	3.94 ± 0.24	58.86 ± 2.05	10.12 ± 1.29
	75	3.15 ± 0.17	38.54 ± 1.76	13.86 ± 0.96

Table 1 (continued)

	35	7.18 ± 0.63	59.71 ± 4.03	2.66 ± 0.22
0.15	55	5.29 ± 0.4	45.83 ± 3.2	6.92 ± 0.5
	75	4.06 ± 0.4	37.32 ± 0.93	10.95 ± 0.66

4. Conclusion

Nacre-inspired composite films were successfully prepared with alumina-platelets in a chitosan solution. They emulate the brick-and-mortar structure of the natural material and could be made with film thicknesses and volumes significantly higher than those of similar composition reported in the literature.[4, 5] While the modulus increased and the strain decreased with an increase in particle content, the strength did not increase with volume fractions greater than 5%. Voids, insufficient particle-matrix bonding, and platelet clustering are thought to introduce flaws, which result in decreased tensile strength. This can be investigated in the future by functionalizing the alumina surface to facilitate a chemical bond between the alumina and chitosan, thus increasing the interfacial strength of the composite. Also at higher volume fractions, processing methods would have to be improved to reduce the clustering that occurs. We have shown that an organized structure can be maintained at higher volume fractions and the fabrication method has a potential to be used for larger scale applications. Particularly noteworthy is the effect of relative humidity, a frequently neglected factor, on the mechanical performance. An increase in the relative humidity from 35% to 75% results in a 48.1% decrease in modulus and up to fourfold increase in strain at failure for the chitosan-alumina films. These results are steps towards a better understanding of the

mechanisms that drive biological systems as well as towards improved processes to emulate them in the laboratory. With improvements in the materials and processing techniques, it will become possible to manufacture complex hybrid materials whose mechanical properties can be custom-designed for specific applications and environmental conditions.

5. Experimental Section

Materials: Low molecular weight chitosan (75-85% deacetylated) was purchased from Sigma Aldrich, St. Louis, MO, USA. Glacial acetic acid, deionized water, and tissue culture dishes were purchased from VWR International, Radnor, PA, USA. Alumina platelets with a diameter and a thickness of 5-10 µm and 300-500 nm, respectively, were obtained from Alusion^{TM}, Antaria Limited, Bentley, Western Australia. Deionized water was used for all experiments and all chemicals were used without further modifications.

Film Preparation: To prepare the nacre-inspired alumina-chitosan hybrid films, first 3.6% (w/v) of low molecular weight chitosan was dissolved in 1% (v/v) glacial acetic acid in de-ionized water. The chitosan solution was homogenized on a bottle roller for 48 hours at room temperature (25°C). To prepare the ceramic slurry, alumina platelets were added to the chitosan solution to achieve the required volume fraction of alumina in the dry film once the solution was cast. For example, to prepare a 5% volume fraction thin film, we took 10 mL of the chitosan solution, which contains 0.36 g or 0.295 cm^3 of chitosan (density of chitosan is 1.22 g/cm^3), and added 0.0155 cm^3 or 0.0621 g of alumina (density of alumina is 4 g/cm^3). Similarly, for 10% and 15% volume fraction, 0.1312 g and 0.2082 g of alumina is added. The ceramic slurry was then shear-mixed (SpeedMixer DAC 150 FVZ-K, FlackTek Inc., Landrum, SC, USA) at 2700 rpm for two

minutes before film preparation. The hybrid films were slip cast in a 150mm diameter petri dish using the method depicted in **Figure 56**. Electrical tape was placed at the edges as shown in **Figure 56** such that the final width of the film was 90 mm and final thickness was 10–40 μm. The petri dish was then placed in a fume hood and allowed to dry at room temperature for at least 24 hours. Once dry, the films were then slowly peeled from the petri dishes by hand. The thickness of the dry film can be controlled by increasing the thickness of the electrical tape.

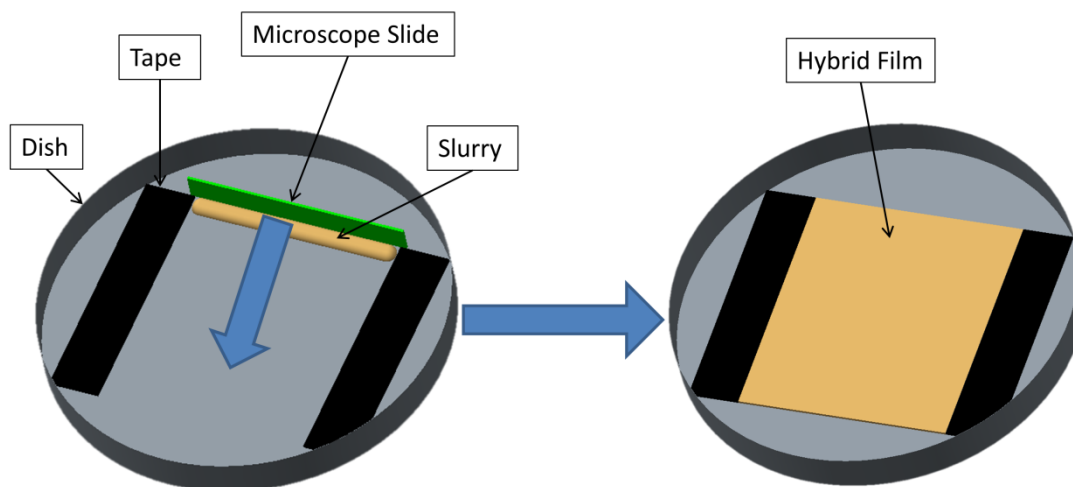Figure 56 - Preparation of hybrid thin films using a slip casting method.

Scanning Electron Microscopy: For observation by scanning electron microscopy (SEM), the films were first freeze-fractured in liquid nitrogen, to reduce disturbance to the cross-section, and then sputter-coated (Cressington 108 Auto Sputter Coater, Cressington Scientific Instruments Inc., Watford, England, UK) with a 2–5 nm thick

platinum-paladium layer. Cross-sections of the films were observed in a scanning electron microscope (Zeiss Supra 50VP, Carl Zeiss SMT Inc., Peabody, MA, USA).

Mechanical Testing: For mechanical testing in tension, the films were cut into a dumbbell shape (ASTM D1708-06), with a narrow section 17 mm long and 5 mm wide, with a microtensile die (Pioneer-Dietecs, Weymouth, MA, USA).[108] The strips were taped with double-sided tape into custom made paper-frames to stabilize them before the test and gripping in the vices with a gauge length of 22 mm for testing (**Figure 57**). To condition the films at $36\pm0.1\%$, $56\pm0.1\%$ and $75+0.1\%$ relative humidity, saturated solutions of Sodium Chloride (ACS grade, EMD Chemicals, Gibbstown, NJ, USA), Magnesium Nitrate (ACS grade, Alfa Aesar, Ward Hill, MA, USA), and Magnesium Chloride (ACS grade, Alfa Aesar) were prepared. The solutions were then poured into the bottom of a desiccator with the framed films placed on a ceramic plate and allowed to condition for at least 48 hours as specified by ASTM D618-13.[109, 110] At least 5 strips were tested for all four compositions at three different relative humidities. Mechanical testing was carried out in tension on an Instron 5948 (Instron, Norwood, MA, USA) with a 50 N load cell and a crosshead speed of 1 mm/min, corresponding to a strain rate of 0.045/s. For testing, a climate chamber was built around the Instron, which ensured that the samples could be tested at a well-defined humidity identical to that, at which the films had been conditioned prior to testing. The climate chamber consisted of a BioPuls (Instron, Norwood, MA, USA) bath chamber around the testing system sealed by elastic bellows (TheRubberStore.com, Dayton, Ohio, USA) as shown in **Figure 58**. Tests were performed after the relative humidity in the chamber had reached and stabilized at each respective relative humidity. The true stress–true strain curves were plotted using the

measured force and displacement and the dimensions of the film. Young's modulus was calculated from the slope of the initial linear region, the tensile strength was taken to be the highest stress of the true stress-strain curve, and the strain at failure was taken when the stress started decreasing before it fully failed.
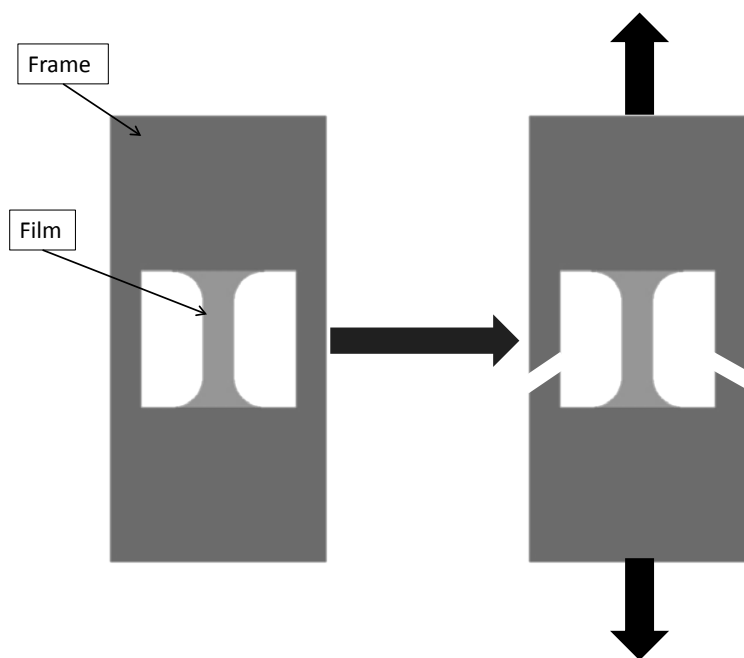
Figure 57 - Frame for tensile testing

Humidity control: The saturated salt solutions mentioned above were prepared by adding the salts in boiling deionized water until no more salt could be dissolved. Magnesium Chloride was used to achieve an average relative humidity of 35.7±0.1%, Magnesium Nitrate was used to achieve an average relative humidity of 56±0.1%, and Sodium Chloride was used to achieve an average relative humidity of 75.4±0.1%. Before the start of each tensile test, salt solutions were placed in separate containers at the

bottom of the biobath and a small fan was used to circulate the air over salt solutions and to ensure a uniform relative humidity in the climate chamber. The required humidity was usually reached within a few minutes and stayed within 0.1% relative humidity for the duration of the test. The fan was turned off for the duration of each test directly before each test was performed.
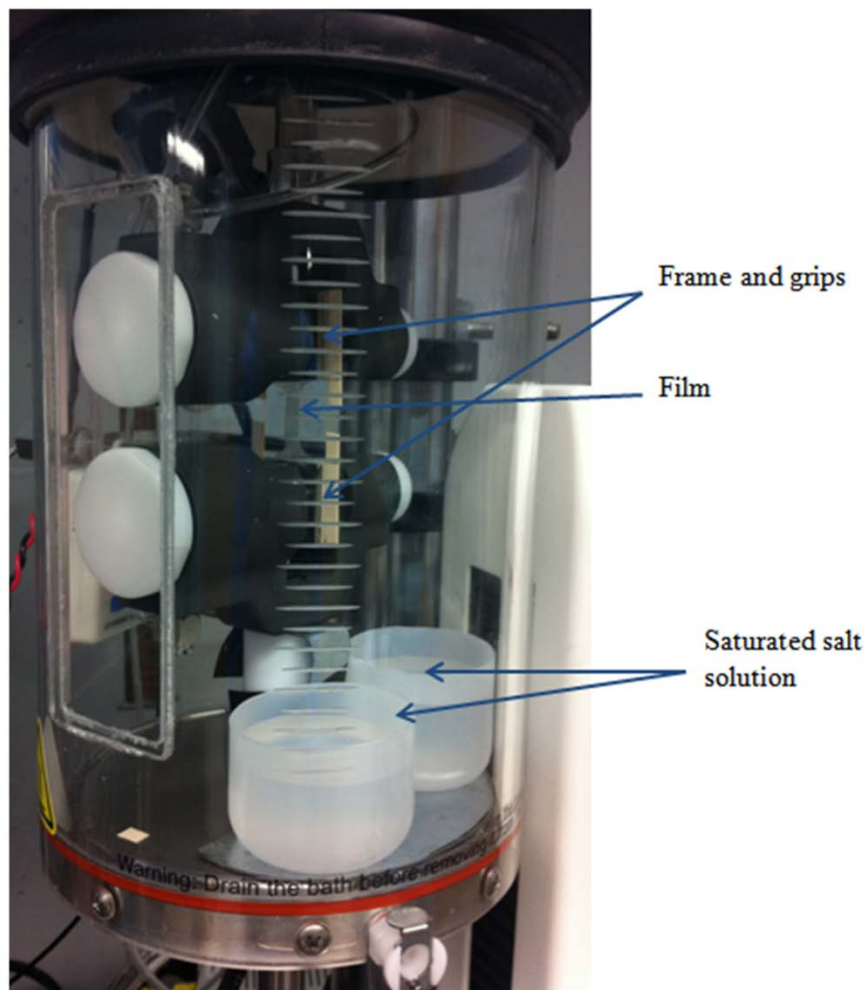
Figure 58 - Setup for tensile testing of chitosan films.

REFERENCES

[1]   Ramakrishna, S., et al., *Biomedical applications of polymer-composite materials: a review.* Composites Science and Technology, 2001. **61**(9): p. 1189-1224.

[2]   Munch, E., et al., *Tough, Bio-Inspired Hybrid Materials.* Science, 2008. **322**(5907): p. 1516-1520.

[3]   Walther, A., et al., *Large-area, lightweight and thick biomimetic composites with superior material properties via fast, economic, and green pathways.* Nano Lett, 2010. **10**(8): p. 2742-8.

[4]   Bonderer, L.J., A.R. Studart, and L.J. Gauckler, *Bioinspired design and assembly of platelet reinforced polymer films.* Science, 2008. **319**(5866): p. 1069-1073.

[5]   Bonderer, L.J., et al., *Strong and ductile platelet-reinforced polymer films inspired by nature: Microstructure and mechanical properties.* Journal of Materials Research, 2009. **24**(9): p. 2741-2754.

[6]   Podsiadlo, P., et al., *Ultrastrong and Stiff Layered Polymer Nanocomposites.* Science, 2007. **318**(5847): p. 80-83.

[7]   Wegst, U.G.K., et al., *Biomaterials by freeze casting.* Philosophical Transactions of the Royal Society a-Mathematical Physical and Engineering Sciences, 2010. **368**(1917): p. 2099-2121.

[8]   Ebina, T. and F. Mizukami, *Flexible transparent clay films with heat-resistant and high gas-barrier properties.* Advanced Materials, 2007. **19**(18): p. 2450-+.

[9]   Malwitz, M.M., et al., *Layered structures of shear-oriented and multilayered PEO/silicate nanocomposite films.* Physical Chemistry Chemical Physics, 2004. **6**(11): p. 2977-2982.

[10]   Deville, S., et al., *Freezing as a path to build complex composites.* Science, 2006. **311**(5760): p. 515-518.

[11]   Dunlop, J.W.C. and P. Fratzl, *Biological Composites*, in *Annual Review of Materials Research, Vol 40*, D.R. Clarke, M. Ruhle, and F. Zok, Editors. 2010, Annual Reviews: Palo Alto. p. 1-24.

[12]   Haque, M.A. and M.T.A. Saif, *A review of MEMS-based microscale and nanoscale tensile and bending testing.* Experimental Mechanics, 2003. **43**(3): p. 248-255.

[13]   Bhushan, B., *Nano- to microscale wear and mechanical characterization using scanning probe microscopy.* Wear, 2001. **251**(1–12): p. 1105-1123.

[14]   Hemker, K.J. and W.N. Sharpe, *Microscale characterization of mechanical properties*, in *Annual Review of Materials Research*. 2007, Annual Reviews: Palo Alto. p. 93-126.

[15]   Fischer-Cripps, A.C., *Nanoindentation*. Mechanical Engineering Series, ed. F.F. Ling. 2002, New York: Springer.

[16]   Bhushan, B., *Handbook of Micro/Nano Tribology, Second Edition*. 1998: Taylor & Francis.

[17]   Kalidindi, S.R. and S. Pathak, *Determination of the effective zero-point and the extraction of spherical nanoindentation stress–strain curves.* Acta Materialia, 2008. **56**(14): p. 3523-3532.

[18]   Pathak, S., et al., *Analyzing indentation stress–strain response of LaGaO3 single crystals using spherical indenters.* Journal of the European Ceramic Society, 2008. **28**(11): p. 2213-2220.

[19]   Pathak, S., D. Stojakovic, and S.R. Kalidindi, *Measurement of the local mechanical properties in polycrystalline samples using spherical nanoindentation and orientation imaging microscopy.* Acta Materialia, 2009. **57**(Copyright 2009, The Institution of Engineering and Technology): p. 3020-8.

[20]   Donohue, B.R., A. Ambrus, and S.R. Kalidindi, *Critical evaluation of the indentation data analyses methods for the extraction of isotropic uniaxial mechanical properties using finite element models.* Acta Materialia, 2012. **60**(9): p. 3943-3952.

[21]   Mase, G., *Schaum's Outline of Continuum Mechanics*. 1970: McGraw-Hill Education.

[22]   Lakes, R., *Viscoelastic Materials*. 2009: Cambridge University Press.

[23]   Eringen, A.C., *Continuum mechanics of single-substance bodies*. 2013: Academic Press.

[24]   Brinson, H. and C. Brinson, *Polymer engineering science and viscoelasticity: an introduction.* 2008, New York: Springer.

[25]   Gauthier, M.M., *Engineered materials handbook*. 1995: ASM International.

[26]   Lakes, R.S. and A. Wineman, *On Poisson's ratio in linearly viscoelastic solids.* Journal of Elasticity, 2006. **85**(1): p. 45-63.

[27]   Fischer-Cripps, A.C., *Nanoindentation*. Vol. 1. 2011: Springer.

[28]   Schuh, C.A., *Nanoindentation studies of materials.* Materials Today, 2006. **9**(5): p. 32-40.

[29]   Oliver, W.C. and G.M. Pharr, *Measurement of hardness and elastic modulus by instrumented indentation: Advances in understanding and refinements to methodology.* Journal of Materials Research, 2004. **19**(Compendex): p. 3-20.

[30]   Bucaille, J.L., et al., *Determination of plastic properties of metals by instrumented indentation using different sharp indenters.* Acta Materialia, 2003. **51**(6): p. 1663-1678.

[31]   Herrmann, M., et al., *Determination of Young's modulus and yield stress of porous low-k materials by nanoindentation.* Surface and Coatings Technology, 2006. **201**(7): p. 4305-4310.

[32]   Yang, B., L. Riester, and T.G. Nieh, *Strain hardening and recovery in a bulk metallic glass under nanoindentation.* Scripta Materialia, 2006. **54**(7): p. 1277-1280.

[33]   Ashby, M., *Indentation creep.* Materials science and technology, 1992. **8**(7): p. 594-601.

[34]   Pharr, G.M., D.S. Harding, and W.C. Oliver, *Measurement of Fracture Toughness in Thin Films and Small Volumes Using Nanoindentation Methods*, in *Mechanical Properties and Deformation Behavior of Materials Having Ultra-Fine Microstructures*, M. Nastasi, D. Parkin, and H. Gleiter, Editors. 1993, Springer Netherlands. p. 449-461.

[35]   Pathak, S., et al., *Analyzing indentation behavior of LaGaO3 single crystals using sharp indenters.* Journal of the European Ceramic Society, 2008. **28**(10): p. 2039-2047.

[36]   Huang, G. and H. Lu, *Measurements of two independent viscoelastic functions by nanoindentation.* Experimental Mechanics, 2007. **47**(1): p. 87-98.

[37]   Cheng, L., et al., *Spherical-tip indentation of viscoelastic material.* Mechanics of Materials, 2005. **37**(1): p. 213-226.

[38]   VanLandingham, M.R., et al., *Viscoelastic characterization of polymers using instrumented indentation. I. Quasi-static testing*.* Journal of Polymer Science Part B: Polymer Physics, 2005. **43**(14): p. 1794-1811.

[39]   Oyen, M.L., *Handbook of nanoindentation with biological applications.* 2011: Pan Stanford Singapore.

[40]   Field, J.S. and M.V. Swain, *A simple predictive model for spherical indentation.* Journal of Materials Research, 1993. **8**(02): p. 297-306.

[41]   Pathak, S., D. Stojakovic, and S.R. Kalidindi, *Measurement of the local mechanical properties in polycrystalline samples using spherical nanoindentation and orientation imaging microscopy.* Acta Materialia, 2009. **57**(10): p. 3020-3028.

[42]   Hertz, H., *Uber die Beruhrung fester Elastischer Korper.* Journal fer die Reine und Angewandte Mathematik, 1881. **92**: p. 156-171.

[43]   Pharr, G.M. and A. Bolshakov, *Understanding nanoindentation unloading curves.* Journal of Materials Research, 2002. **17**(10): p. 2660-2671.

[44]   Hainsworth, S.V., H.W. Chandler, and T.F. Page, *Analysis of nanoindentation load-displacement loading curves.* Journal of Materials Research, 1996. **11**(8): p. 1987-1995.

[45]   Oliver, W.C. and G.M. Pharr, *An improved technique for determining hardness and elastic modulus using load and displacement sensing indentation experiments.* Journal of Materials Research, 1992. **7**(06): p. 1564-1583.

[46]   Park, Y.J. and G.M. Pharr, *Nanoindentation with spherical indenters: finite element studies of deformation in the elastic–plastic transition regime.* Thin Solid Films, 2004. **447–448**(0): p. 246-250.

[47]   Li, X. and B. Bhushan, *A review of nanoindentation continuous stiffness measurement technique and its applications.* Materials Characterization, 2002. **48**(Compendex): p. 11-36.

[48]   Pharr, G.M., J.H. Strader, and W.C. Oliver. *Critical issues in making small-depth mechanical property measurements by nanoindentation with continuous stiffness measurement.* 2009. 506 Keystone Drive, Warrendale, PA 15086, United States: Materials Research Society.

[49]   Vachhani, S.J., R.D. Doherty, and S.R. Kalidindi, *Effect of the continuous stiffness measurement on the mechanical properties extracted using spherical nanoindentation.* Acta Materialia, 2013. **61**(10): p. 3744-3751.

[50]   Basu, S., A. Moseson, and M.W. Barsoum, *On the determination of spherical nanoindentation stress-strain curves.* Journal of Materials Research, 2006. **21**(Copyright 2007, The Institution of Engineering and Technology): p. 2628-37.

[51]   Murugaiah, A., et al., *Spherical Nanoindentations and Kink Bands in Ti3SiC2.* Journal of Materials Research, 2004. **19**(04): p. 1139-1148.

[52]   Field, J.S. and M.V. Swain, *Determining the mechanical properties of small volumes of material from submicrometer spherical indentations.* Journal of Materials Research, 1995. **10**(01): p. 101-112.

[53]   Fischer-Cripps, A.C. and B.R. Lawn, *Indentation stress-strain curves for "quasi-ductile" ceramics.* Acta Materialia, 1996. **44**(2): p. 519-527.

[54]   Kalidindi, S.R. and S. Pathak, *Determination of the effective zero-point and the extraction of spherical nanoindentation stress-strain curves.* Acta Materialia, 2008. **56**(Copyright 2008, The Institution of Engineering and Technology): p. 3523-32.

[55]   Pathak, S., et al., *Importance of surface preparation on the nano-indentation stress-strain curves measured in metals.* Journal of Materials Research, 2009. **24**(Copyright 2009, The Institution of Engineering and Technology): p. 1142-55.

[56]   Lee, E.H., *Stress Analysis in Viscoelastic Materials.* Journal of Applied Physics, 1956. **27**(7): p. 665-672.

[57]   Lee, E.H. and J.R.M. Radok, *The Contact Problem for Viscoelastic Bodies.* Journal of Applied Mechanics, 1960. **27**(3): p. 438-444.

[58]   Hunter, S.C., *The Hertz problem for a rigid spherical indenter and a viscoelastic half-space.* Journal of the Mechanics and Physics of Solids, 1960. **8**(4): p. 219-234.

[59]   Graham, G.A.C., *The contact problem in the linear theory of viscoelasticity.* International Journal of Engineering Science, 1965. **3**(1): p. 27-46.

[60]   Ting, T.C.T., *The Contact Stresses Between a Rigid Indenter and a Viscoelastic Half-Space.* Journal of Applied Mechanics, 1966. **33**(4): p. 845-854.

[61]   Casula, G. and J. Carcione, *Generalized mechanical model analogies of linear viscoelastic behaviour.* Bollettino di geofisica teorica ed applicata, 1992.

[62]   Gutierrez-Lemini, D., *Engineering Viscoelasticity*. 2014: Springer.

[63]   Radok, J.R.M., *Visco-elastic stress analysis*. 1956, DTIC Document.

[64]   Timoshenko, S. and J. Goodier, *Theory of elasticity*. 2nd Edition ed. 1953, New York, N.Y.: McGraw-Hill Book Company Inc.

[65]   Huang, G. and H. Lu, *Measurement of Young's relaxation modulus using nanoindentation.* Mechanics of Time-Dependent Materials, 2006. **10**(3): p. 229-243.

[66]   Briscoe, B.J., L. Fiori, and E. Pelillo, *Nano-indentation of polymeric surfaces.* Journal of Physics D: Applied Physics, 1998. **31**(19): p. 2395.

[67]   Jakes, J.E., R.S. Lakes, and D.S. Stone, *Broadband nanoindentation of glassy polymers: Part I. Viscoelasticity.* Journal of Materials Research, 2012. **27**(02): p. 463-474.

[68]   Oyen, M.L., *Spherical indentation creep following ramp loading.* Journal of Materials Research, 2005. **20**(08): p. 2094-2100.

[69]   Huang, G., B. Wang, and H. Lu, *Measurements of viscoelastic functions of polymers in the frequency-domain using nanoindentation.* Mechanics of Time-Dependent Materials, 2004. **8**(4): p. 345-364.

[70]   Odegard, G., T. Gates, and H. Herring, *Characterization of viscoelastic properties of polymeric materials through nanoindentation.* Experimental Mechanics, 2005. **45**(2): p. 130-136.

[71]   Jäger, A. and R. Lackner, *Identification of viscoelastic model parameters by means of cyclic nanoindentation testing.* International Journal of Materials Research, 2008. **99**(8): p. 829-835.

[72]   Kreyszig, E., *Advanced Engineering Mathematics.* 2010: John Wiley & Sons.

[73]   Cheng, Y.-T. and C.-M. Cheng, *Relationships between initial unloading slope, contact depth, and mechanical properties for spherical indentation in linear viscoelastic solids.* Materials Science and Engineering: A, 2005. **409**(1–2): p. 93-99.

[74]   D695-10, A., *Standard Test Method for Compressive Properties of Rigid Plastics.* ASTM International, 2010.

[75]   Arruda, E.M., M.C. Boyce, and R. Jayachandran, *Effects of strain rate, temperature and thermomechanical coupling on the finite strain deformation of glassy polymers.* Mechanics of Materials, 1995. **19**(2): p. 193-212.

[76]   Spitzig, W. and O. Richmond, *Effect of hydrostatic pressure on the deformation behavior of polyethylene and polycarbonate in tension and in compression.* Polymer Engineering & Science, 1979. **19**(16): p. 1129-1139.

[77]   Goble, D. and E. Wolff, *Strain-rate sensitivity index of thermoplastics.* Journal of materials science, 1993. **28**(22): p. 5986-5994.

[78]   Berthoud, P., et al., *Physical analysis of the state-and rate-dependent friction law: Static friction.* Physical review B, 1999. **59**(22): p. 14313.

[79]   Fujisawa, N. and M. Swain, *Nanoindentation-derived elastic modulus of an amorphous polymer and its sensitivity to load-hold period and unloading strain rate.* Journal of Materials Research, 2008. **23**(03): p. 637-641.

[80]   Dutta, P.K., J. Dutta, and V. Tripathi, *Chitin and chitosan: Chemistry, properties and applications.* Journal of Scientific and industrial research, 2004. **63**(1): p. 20-31.

[81]   Zhang, Z., Y.W. Zhang, and H. Gao, *On optimal hierarchy of load-bearing biological materials.* Proc Biol Sci, 2011. **278**(1705): p. 519-25.

[82]   Launey, M.E. and R.O. Ritchie, *On the Fracture Toughness of Advanced Materials.* Advanced Materials, 2009. **21**(20): p. 2103-2110.

[83]   Studart, A.R., *Towards High-Performance Bioinspired Composites.* Advanced Materials, 2012. **24**(37): p. 5024-5044.

[84]   Kakisawa, H. and T. Sumitomo, *The toughening mechanism of nacre and structural materials inspired by nacre.* Science and Technology of Advanced Materials, 2011. **12**(6): p. 064710.

[85]   Jackson, A.P., J.F.V. Vincent, and R.M. Turner, *The Mechanical Design of Nacre.* Proceedings of the Royal Society of London. Series B. Biological Sciences, 1988. **234**(1277): p. 415-440.

[86]   Barthelat, F., *Nacre from mollusk shells: a model for high-performance structural materials.* Bioinspiration & Biomimetics, 2010. **5**(3).

[87]   Meyers, M.A., et al., *Biological materials: structure and mechanical properties.* Progress in Materials Science, 2008. **53**(1): p. 1-206.

[88]   Yao, H.B., et al., *Artificial Nacre-like Bionanocomposite Films from the Self-Assembly of Chitosan–Montmorillonite Hybrid Building Blocks.* Angewandte Chemie International Edition, 2010. **49**(52): p. 10127-10131.

[89]   Bonderer, L.J., K. Feldman, and L.J. Gauckler, *Platelet-reinforced polymer matrix composites by combined gel-casting and hot-pressing. Part I: Polypropylene matrix composites.* Composites Science and Technology, 2010. **70**(13): p. 1958-1965.

[90]   Bonderer, L.J., K. Feldman, and L.J. Gauckler, *Platelet-reinforced polymer matrix composites by combined gel-casting and hot-pressing. Part II: Thermoplastic polyurethane matrix composites.* Composites Science and Technology, 2010. **70**(13): p. 1966-1972.

[91]   Hunger, P.M., A.E. Donius, and U.G.K. Wegst, *Platelets self-assemble into porous nacre during freeze casting.* Journal of the Mechanical Behavior of Biomedical Materials, 2013. **19**(0): p. 87-93.

[92]   Hunger, P.M., A.E. Donius, and U.G.K. Wegst, *Structure–property-processing correlations in freeze-cast composite scaffolds.* Acta Biomaterialia, 2013. **9**(5): p. 6338-6348.

[93]   Gao, H.J., et al., *Materials become insensitive to flaws at nanoscale: Lessons from nature.* Proceedings of the National Academy of Sciences of the United States of America, 2003. **100**(10): p. 5597-5600.

[94]   Domard, A. and M. Domard, *Chitosan : Structure – Properties Relationship and Biomedical Applications*, in *Polymeric Biomaterials*, S. Dumitriu, Editor. 2002, Marcel Dekker: New York. p. 187 - 212.

[95]   Rachtanapun, P. and P. Wongchaiya, *Effect of Relative Humidity on Mechanical Properties of Blended Chitosan-Methylcellulose Film.* Chiang Mai Journal of Science, 2012. **39**(1): p. 133-137.

[96]   Richardson, M., *Polymer engineering composites*. 1977: Elsevier Science & Technology.

[97]   Barthelat, F. and M. Mirkhalaf, *The quest for stiff, strong and tough hybrid materials: an exhaustive exploration.* Journal of The Royal Society Interface, 2013. **10**(89).

[98]   Chawla, K.K., *Composite materials: science and engineering*. 2012: Springer.

[99]   Meyers, M.A. and K.K. Chawla, *Mechanical Behavior of Materials*. 2009: Cambridge University Press.

[100]   Jäger, I. and P. Fratzl, *Mineralized collagen fibrils: a mechanical model with a staggered arrangement of mineral particles.* Biophysical Journal, 2000. **79**(4): p. 1737-1746.

[101]   Glavinchevski, B. and M. Piggott, *Steel disc reinforced polycarbonate.* Journal of Materials Science, 1973. **8**(10): p. 1373-1382.

[102]   Padawer, G.E. and N. Beecher, *On the strength and stiffness of planar reinforced plastic resins.* Polymer Engineering & Science, 1970. **10**(3): p. 185-192.

[103]   Ji, B. and H. Gao, *Mechanical principles of biological nanocomposites.* Annual Review of Materials Research, 2010. **40**: p. 77-100.

[104]   Shukla, D. and V. Parameswaran, *Epoxy composites with 200 nm thick alumina platelets as reinforcements.* Journal of Materials Science, 2007. **42**(15): p. 5964-5972.

[105]   Nurul Hazwani, M., et al., *EFFECT OF PRESSURE ON ELASTIC PROPERTIES OF CHITOSAN.* Journal of Solid State Science and Technology, 2011. **19**(2): p. 120 - 127.

[106]   Shukla, D.K., S.V. Kasisomayajula, and V. Parameswaran, *Epoxy composites using functionalized alumina platelets as reinforcements.* Composites Science and Technology, 2008. **68**(14): p. 3055-3063.

[107]   Liu, K. and M.R. Piggott, *Shear strength of polymers and fibre composites: 1. thermoplastic and thermoset polymers.* Composites, 1995. **26**(12): p. 829-840.

[108]   D1608, *Test Method for Tensile Properties of Plastics by Use of Microtensile Specimens.* ASTM International, 2006.

[109]   D618-13, A., *Practice for Conditioning Plastics for Testing.* ASTM International, 2013.

[110] E104-02(2012), A., *Standard Practice for Maintaining Constant Relative Humidity by Means of Aqueous Solutions.* ASTM International, 2002.

VITA

MOHAMMED T. ABBA

ABBA was born in Cardiff, Wales, UK but spent his first few years in Nigeria. He completed his primary and secondary schooling in Riyadh, Saudi Arabia and enjoyed studying physics and mathematics. He started his Mechanical Engineering degree at the International Centre for Applied Sciences, Manipal University, Manipal, India. After two years he transferred to Drexel University, Philadelphia, PA where he completed his BS and MS in Mechanical Engineering in 2009 and started the PhD program. After three years he transferred to Georgia Institute of Technology with his advisor to complete his PhD. When he is not working on his research, Mr. Abba enjoys running, staying fit, and spending time with friends.